TIP CASING HEAT TRANSFER MEASUREMENTS OF A FILM-COOLED TURBINE STAGE IN A SHORT DURATION FACILITY

by

BRET P. VAN POPPEL

Bachelor of Science in Mechanical Engineering
United States Military Academy, 1992

Submitted to the Department of Aeronautics and Astronautics in partial fulfillment of the requirements for the degree of

MASTER OF SCIENCE

in

AERONAUTICS AND ASTRONAUTICS

at the

MASSACHUSETTS INSTITUTE OF TECHNOLOGY

June 2001

Author:_____
Department of Aeronautics and Astronautics
May 25, 2001

Certified by:_____
Dr. Gerald R. Guenette
Principal Research Engineer
Thesis Supervisor

Accepted by:_____
Wallace E. Vander Velde
Professor Aeronautics and Astronautics
Chair, Committee on Graduate Students

TIP CASING HEAT TRANSFER MEASUREMENTS OF A FILM-COOLED TURBINE STAGE IN A SHORT DURATION FACILITY

by

Bret P. Van Poppel

Submitted to the Department of Aeronautics and Astronautics on May 25, 2001, in partial fulfillment of the requirements for the degree of Master of Science

Abstract

An experimental study of the heat transfer to the tip casing of a fully scaled turbine stage was conducted. Pressure and surface temperature measurements were taken on the tip casing. Time-averaged heat flux data was computed and used to assess the influence of stage total pressure ratio, corrected speed and tip gap on casing heat flux.

The experimental work was conducted in the MIT Blowdown Turbine Facility using a highly loaded, film-cooled turbine stage. The facility is a short duration experimental structure capable of testing turbine stages under fully scaled conditions to produce useful test durations of 0.5 seconds. The turbine stage tested consisted of film-cooled turbine blades and nozzle guide vanes. During the course of this research, semi-infinite heat flux gauges were designed and fabricated by painting and baking thin platinum films onto machineable ceramic substrates. These gauges were used to experimentally measure surface temperatures on the tip casing with an estimated frequency response of 60 kilohertz. A tip casing insert was designed as an instrument holder to orient the heat flux gauges and highly sensitive pressure transducers on the tip casing surface to spatially resolve heat flux and static pressure.

A matrix of test conditions was devised to investigate the effects of various run conditions and tip gaps on tip casing flow. Both a 3.0% and a 1.5% tip-gap-to-span ratio were tested. Run conditions were established by varying the stage pressure ratio and the corrected speed. Results were compared within each test, between tests at the same tip gap, and between tests at different tip gaps. Time averaged data revealed the influence of rotor enthalpy extraction on casing heat flux. Pressure and corrected speed tests showed similar trends at both tip gaps. At design conditions, average endwall heat transfer was approximately 4% greater for the 1.5% tip gap.

Thesis Supervisor: Dr. Gerald R. Guenette
Title: Principal Research Engineer
Department of Aeronautics and Astronautics
Gas Turbine Laboratory

ACKNOWLEDGEMENTS

I must express my deepest gratitude to Dr. Gerald R. Guenette, *"the Colonel."* His wisdom is remarkable, and second only to his breadth of understanding of the physical sciences. His influence, though, was not limited to merely the role of advisor. In a day when leadership seems to be a lost art, Jerry stands as a true leader of character. Thank you, sir.

There are many in this laboratory who have contributed to the project, this document, and my edification. I especially appreciate the work of Jack Costa, Viktor Dubrowski, Jimmy Letendre, Bill Ames, and Holly Anderson; without their help, this project would not have been feasible. On behalf of all graduate students in the lab, I must extend my sincere appreciation to the devotion and efforts of Lori Martinez—where would we be without her?

Fellow students, past and present, made life and learning more entertaining. Up front, I must thank Jameel and Will, fellow BDT pit crew members; best of luck to both of you. Additionally, Dan, Chris, Rory, Zolti, Amit, Luc, Steve, Carol, and many others deserve hearty thanks.

To my wife, Chrisanne, and son, Henry William, I cannot find words appropriate to express my appreciation for the happiness and joy you bring me everyday. Thank you for your patience, understanding, assistance, and support.

I extend my grateful appreciation to the Engineers at Alstom Power for sponsoring this program, and to the United States Army for sponsoring me.

My efforts over the past two years are dedicated to the cherished memory of:

Joseph J. Suminski, 1930-2001

Corporal, U.S. Army, Korean Conflict (1950-52)

Loving Husband, Mentor, Coach, and Friend.

CONTENTS

LIST OF FIGURES

LIST OF TABLES

NOMENCLATURE

Roman

a	speed of sound
A	area
c	specific heat capacity
h	enthalpy
I	moment of inertia
k	thermal conductivity
l	length
L_{ref}	reference length
$\dot{m}$	mass flow rate
N_c	corrected speed
N_h	non-dimensionalized heat transfer coefficient
N_q	non-dimensionalized heat flux
P	pressure
P	power
q	heat flux
Q_0	resistive heat
R	gas constant
R	resistance
t	time
t	thickness
T	temperature
V	voltage
w	width

Greek

α	temperature coefficient of resistivity
δ	thermal penetration depth
γ	ratio of specific heat
κ	thermal diffusivity
ρ	density
Ω	angular velocity
ω	frequency

Subscripts

0	inlet conditions
s	surface conditions
t	stagnation quantity

Acronyms

ASME	American Society of Mechanical Engineers
ANSI	American National Standards Institute
DAQ	Data Acquisition System
FSTI	Flow Similarity Test Interval
NIST	National Institute of Standards in Technology
PR	Pressure Ratio
RTD	Resistance Temperature Detector
RTV	Room Temperature Vulcanization
TCI	Tip Casing Insert

Chapter 1

Introduction

1.1 Background

Dramatic advances in gas turbine technology over the past 50 years have resulted in much higher efficiencies and performance. In large electrical power applications, gas turbine engine temperatures have exceeded 1700 K. Indeed, turbine inlet temperature is the defining temperature for many engines. Polytropic efficiencies of axial flow turbines now exceeds 90%. Higher heat loads within the turbine are by-products of these advances. As such, an engine's ability to handle high heat loads has become a paramount concern and sparked extensive research in the past decade, especially in high-pressure turbines. Conventional turbine cooling schemes—including film-cooling, internal convective cooling, and internal impingement cooling—have been designed and developed to mitigate the effects of extreme heat loads on blades, shrouds, and tip casings.

Experimental testing has been used to study the magnitude and characteristics of heat transfer within the turbine. Currently, steady state turbine testing has become expensive and impractical. Costs can easily exceed $5 million even for relatively benign test conditions (inlet temperatures approximately 450K). Thus, steady state testing is not a viable option at many academic institutions. In the power generation industry, full-scale steady state test facilities are typically not employed due to their immense size and power consumption. In most cases, engine components are tested in service and result in minimal improvements in efficiency, performance and cooling.

In the 1980's, a new technology was developed to study turbine performance at the Gas Turbine Laboratory at MIT: the Blowdown Turbine (BDT). Based upon transient testing techniques, researchers at MIT have produced highly accurate data for heat transfer and aerodynamic performance of axial flow turbines. The facility is a short duration test rig, with time scales on the order of several hundred milliseconds. With high frequency instrumentation, steady state data can be taken in less than one second. With scaling of relevant parameters—Reynolds number, total stage pressure ratio, gas-to-wall temperature ratio, and corrected speed—turbine inlet temperature can be significantly reduced. Compared with steady state rigs, the BDT requires much less power to run. This adds up to considerably lower costs of construction, maintenance and operation.

Heat transfer measurements on both turbine blades and tip casings have been demonstrated in previous research programs on the BDT. Thus, with instrumentation of high frequency response and accuracy, a test program to measure the heat transfer to the tip casing of a film-cooled turbine stage has been undertaken. This document is a summary of the research work and results.

1.2 Previous Work

A short history of the work conducted on MIT's Blowdown Turbine facility is reviewed below.

The BDT was designed by Guenette [9]. The initial work focused on the design and development efforts of the more salient components of the facility. In particular, the fast-acting main valve, eddy current brake, and heat flux instrumentation constituted significant engineering works. Initial testing in the facility consisted of tip casing heat transfer measurements of an uncooled turbine stage.

Halderman [11] studied the influence of turbine inlet temperature non-uniformities on the heat transfer to the tip casing.

Shang [24] examined the influence of turbine inlet temperature non-uniformities on the heat transfer of turbine blades. Radial temperature distortions were found to have a large effect on turbine heat transfer, while circumferential distortions revealed little effect.

Keogh [15] and Spadaccini [22] examined and compared aerodynamic performance of uncooled and film-cooled turbine stages. Extensive effort to modify an uncooled stage with film-cooling was executed.

Keogh [14] examined the specific aerodynamic loss due to film-cooling and quantified it. Additionally, this research provided a detailed breakdown of the losses associated with film-cooling for the turbine stage.

1.3 Motivation

Previous experimental work has been conducted to measure heat transfer in non-rotating cascades for uncooled turbines. Bunker et al [4] showed a decrease in heat transfer with decreasing tip gap for a 1.45 pressure ratio linear cascade. In computation results based upon the same cascade, Ameri et al [2] showed the migration of flow from leading edge pressure-side to mid-cord suction side, resulting in high levels of heat transfer around the mid-cord region of the blade tip and endwall. Ameri et al [1], through CFD calculations, showed an increase in tip casing heat transfer as the tip gap was increased—a trend prevalent along the entire cord.

Guenette [9], in his initial blowdown experiments, showed an increasing and then decreasing heat load, commensurate with rotor enthalpy extraction, for all test conditions. Additionally, he observed substantial variations in time-averaged heat loads at different operating points and independent parameters. He concluded that the tip leakage flow was coupled with incidence angle (largely a function of corrected speed) and airfoil loading (determined by Pressure Ratio and loading distribution) for the uncooled turbine stage tested.

Little research in available in the literature on heat transfer for a fully scaled, film-cooled turbine stage. The characteristics of an inherently unsteady, complex, three-dimensional endwall flow, exacerbated by the influence of convecting nozzle guide vane wakes and coolant-to-mainstream flow interactions, have not been extensively investigated. The research reported herein constitutes an initial exploration of the tip casing heat transfer under fully-scaled, rotating conditions for a film-cooled turbine stage.

1.4 Objectives

The primary objective of this research was to experimentally measure the tip casing heat transfer of a scaled film-cooled turbine stage. The project posed many engineering challenges to that end. In all, the principal objectives for this project include:

1. The construction and validation of surface temperature thermometers with sufficient frequency response, sensitivity, and stability to adequately measure tip casing heat transfer.

2. The design and fabrication of an instrumented device to hold surface temperature and pressure instruments on the rotor tip casing to resolve spatial and temporal trends in heat transfer and wall static pressure. This includes the necessary facility modifications to adequately house and support the device.

3. The measurement of heat flux on the tip casing of a film-cooled turbine stage.

4. The preliminary investigation of measured tip casing heat transfer to identify trends in time-averaged data and compare results for different operating points and tip gaps.

5. The creation of a detailed data set for use in physics-based modeling, CFD code validation, and eventually the improved design of film-cooled turbine stages of this class.

1.5 Thesis Outline

This chapter introduces the content of the thesis, reviews previous work in the Blowdown Turbine test facility and other related work, and outlines the objectives of the project. Chapter 2 introduces the MIT Blowdown Turbine facility and details all primary components. Facility scaling issues and typical run conditions are discussed. Recent modifications for this research are outlined. Chapter 3 outlines the development from concept through fabrication of semi-infinite heat flux gauges for measuring heat transfer to a turbine tip casing. The chapter presents a simple reduced order model to identify some criteria for material selection and gauge design.

Chapter 4 gives a comprehensive report of the tip casing insert instrumentation holder, identifying design criteria with instrumentation in mind in order to elucidate as much of the flow phenomena as possible without requiring substantial facility modifications. Calibration procedures are also presented. Chapter 5 presents measured turbine performance data to characterize the stage's operation. Chapter 6 presents and discusses the experimentally measured heat transfer data. Non-dimensionalized heat transfer results are displayed for both tip gap ratio tests. Comparisons are made within each test, within the same tip gap for different operating conditions, and between different tip gap tests. Relevant time scales for the purpose of time-averaging are also discussed in this chapter. The thesis concludes with Chapter 7, a summary of results and recommendations for future work.

Chapter 2

Blowdown Turbine Test Facility

2.1 Introduction

The MIT Blowdown Turbine Facility is a short-duration, blowdown wind tunnel capable of testing a complete, rotating stage in an environment that rigorously simulates the fluid physics and heat transfer phenomena that occur in a turbine. This chapter reviews the MIT Blowdown Turbine facility. Overall configuration and operational procedures are described. Scaling of the turbine operating point for achieving full-scale similarity is discussed. Individual components are examined as well as instrumentation and the recently modified coolant feed system. The data acquisition system is also briefly presented.

2.2 Facility Configuration

The MIT Blowdown Turbine test facility is shown in Figure 2-1. The facility consists of seven primary components: the supply tank, fast acting valve, test section, eddy current brake torque meter, critical flow venturi nozzle, coolant feed system (not shown), and dump tank. A detailed review of the overall design of the facility can be found in Guenette [9].

2.2.1 Supply Tank and Main Valve

The supply tank is a 364 cubic foot cylindrical pressure vessel rated at 150 psi. It is surrounded by an external jacket through which heat transfer oil is circulated to heat the tank to the desired test temperature. A stirring fan is employed to ensure a uniform test gas temperature

distribution.

The test section is separated from the supply tank by a fast-acting, axially traversing, plug valve. This valve is designed to fully open in approximately 50 ms and introduce disturbance-free flow into the test section. Valve dynamics are controlled by damping chambers which produce a force on the plug whose magnitude and direction depend on its position and velocity. In its fully closed position, this force acts to seal the plug. After the seal is broken, the valve plug is accelerated open. As it nears its fully open position the plug is decelerated to rest. The force used to break the seal is provided by an internal pneumatic piston assembly actuated by a small compressed gas cylinder.

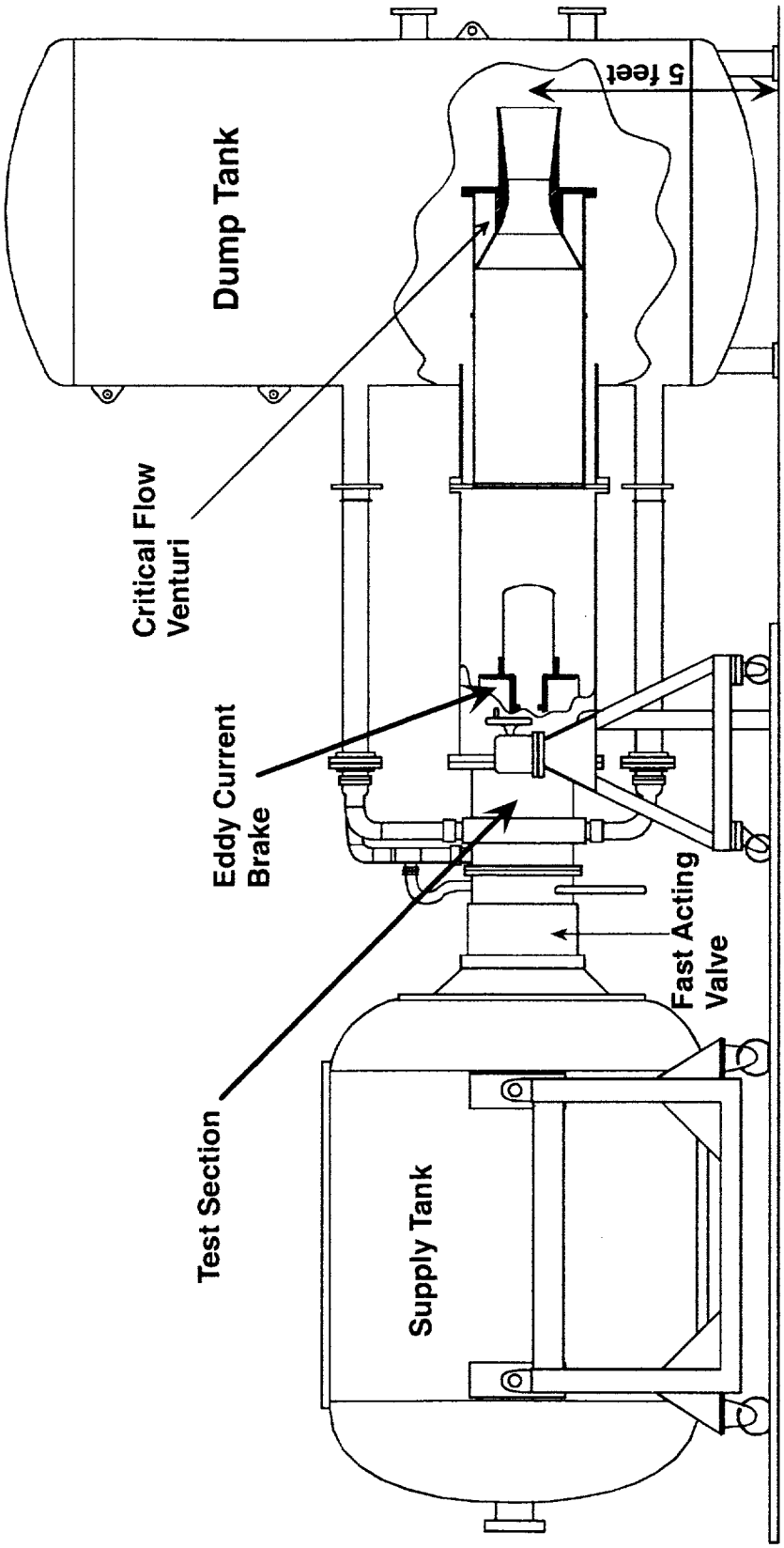

Figure 2-1: Blowdown Turbine Experimental Facility

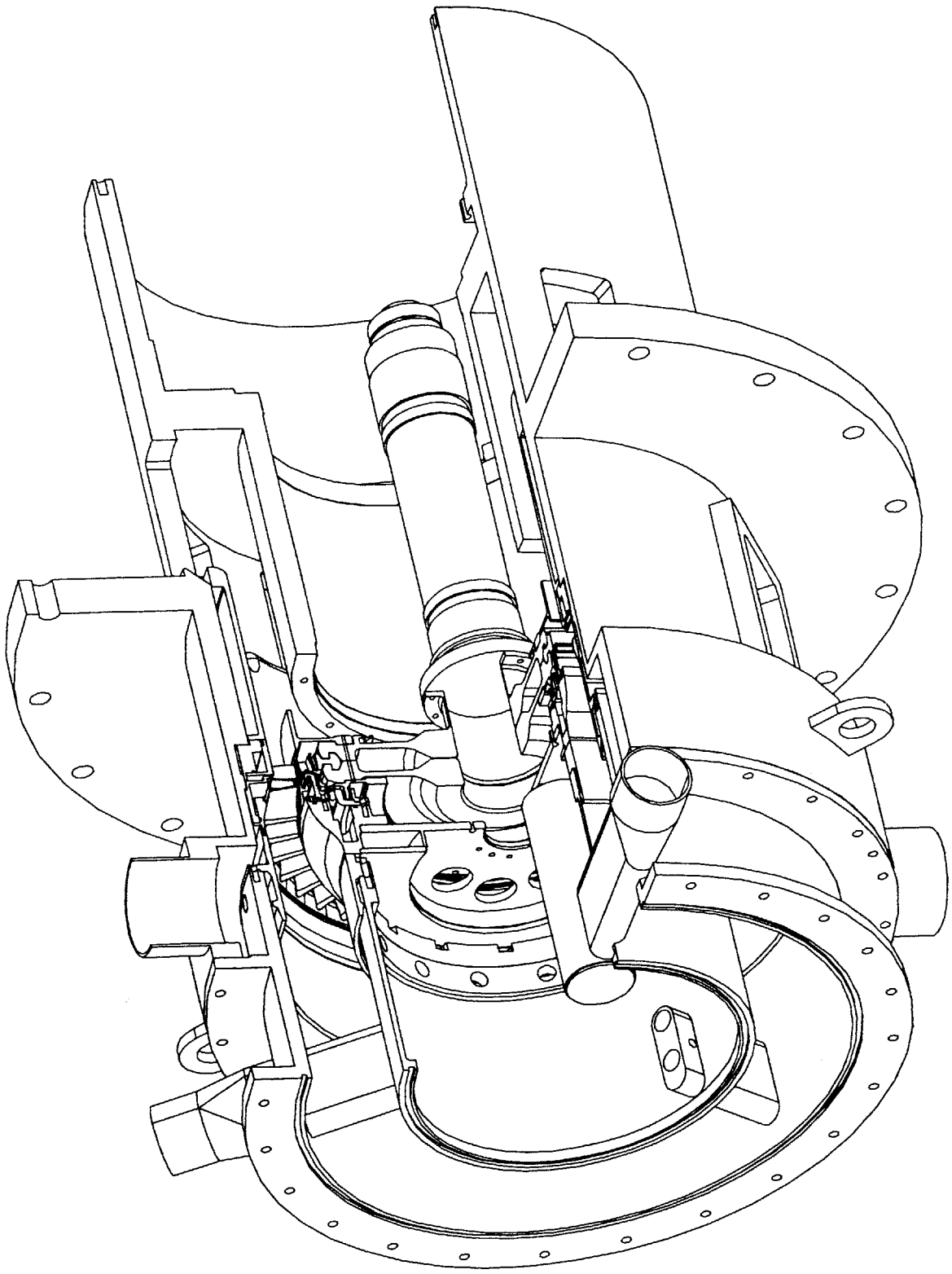

Figure 2-2: Test Section Detail

2.2.2 Test Section

A cut-away of the test section assembly is shown in Figures 2-2 and 2-3. The test section is composed of the forward frame, main frame, and the rotor unit. The forward frame contains the nozzle guide vanes, the inlet boundary layer bleeds, and the rotor heat shield and mates to the main valve. The forward frame is followed by the main frame which houses the turbine rotor assembly, the downstream probe translator package, the eddy current brake magnet assembly, the turbine throttle and drive motor. The rotor unit contains the rotor discs, blades, bearings, shaft, and the eddy current brake 'loss' drum (not shown). This drum is inserted into the eddy current brake magnet assembly.

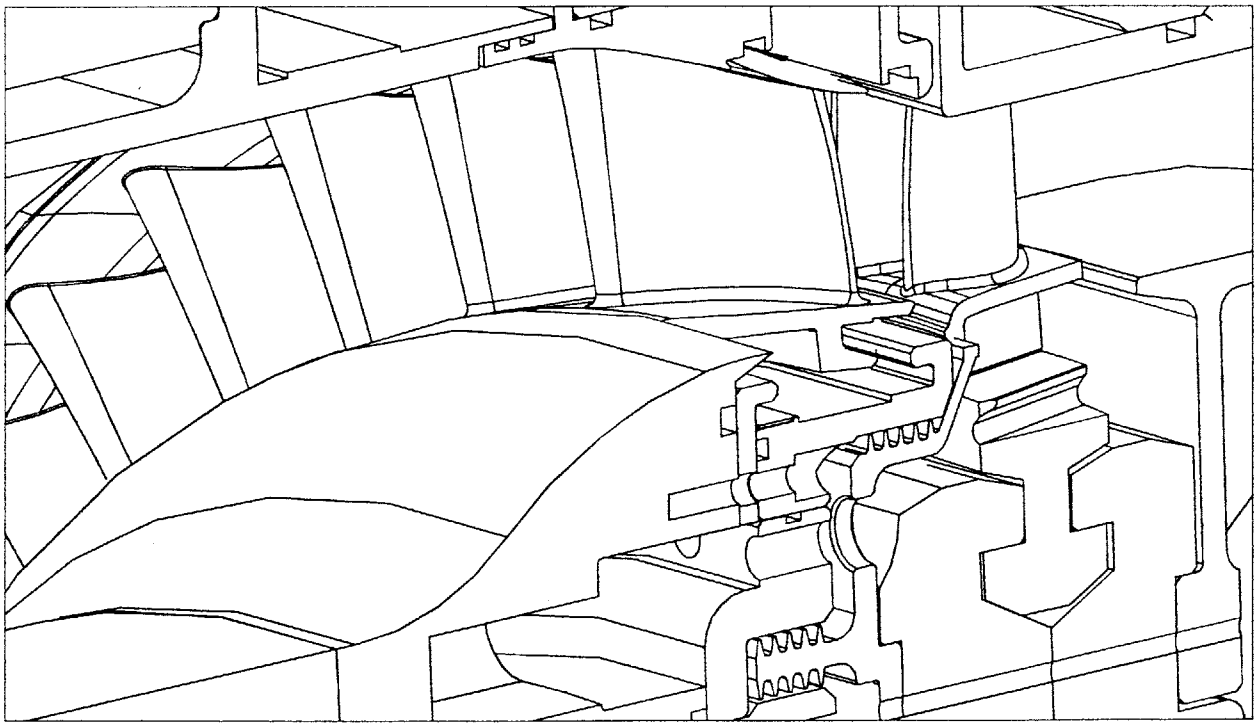

Figure 2-3: Turbine Installation Detail

A cross-sectional view of the test section flow path is shown in Figure 2-4. Upstream of the turbine stage a boundary layer bleed provides clean inlet flow. The rotor exit flow is exhausted through an adjustable throttling area to provide the desired pressure ratio across the turbine. During the usable portion of the test, this area is choked. Also shown in this figure are the upstream and downstream measurement locations. Downstream, the total temperature and pressure probes are mounted on a circumferential translator.

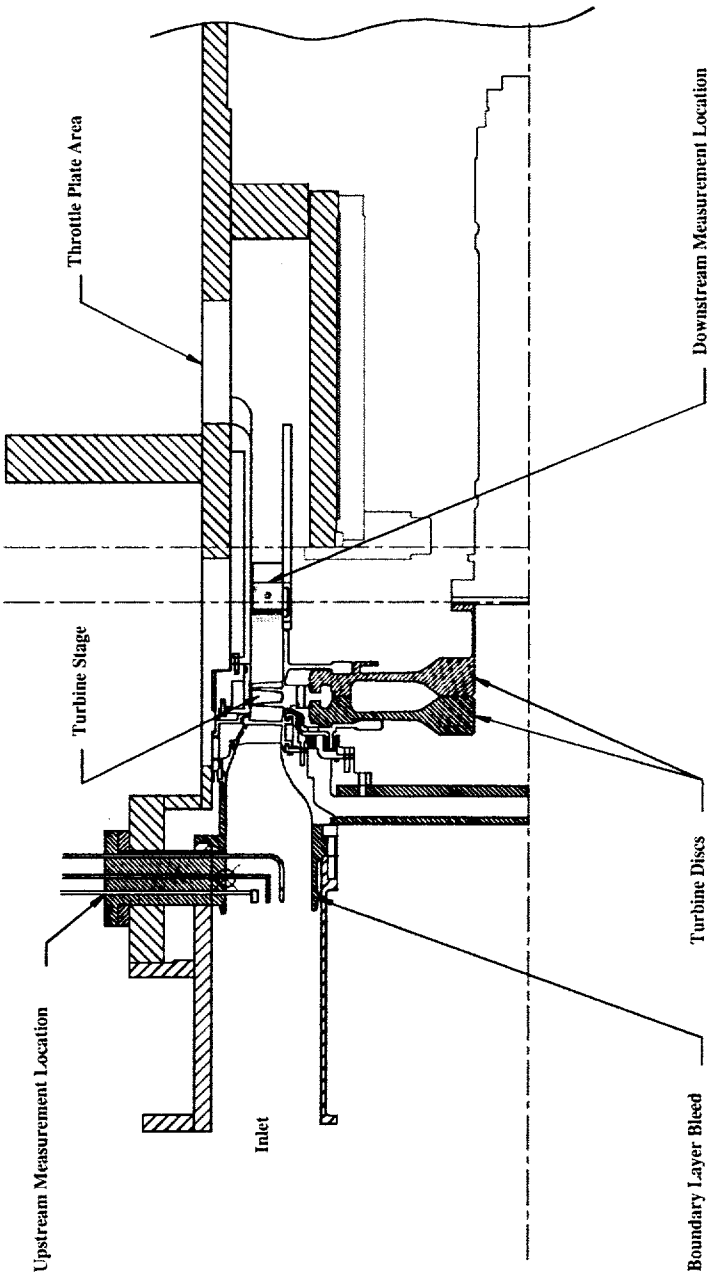

Figure 2-4: Test Section Flow Path

2.2.3 Circumferential Probe Translators

Both upstream and downstream circumferential translators are available to provide measurement of non-axisymmetric features of the turbine flow field. Both are composed of drums forming the inner annulus of the turbine entrance and exit and are mounted on thin-line bearings. For the experiments reported herein, only the downstream translator was employed.

The downstream translator houses three 'canisters' spaced 20° apart, which contain the appropriate electrical and pneumatic connections to support either total temperature or pressure rakes. Connections also provide for several wall static pressure taps. The translator is restricted to a 350° rotation angle by a spring-loaded hard stop to prevent the translator from freely spinning and destroying the canisters' electrical wiring. The translator is driven by a Baldor ME-4090-BLBCE servomotor, delivering approximately 3 in-lb of torque through an equivalent 13.5:1 gear ratio. This motor is controlled by a Galil DMC-400-10 card and powered by a Copley MB6-10 amplifier. In addition to the hard stop, an aluminum shear pin is installed on the shaft coupling exiting the servomotor to prevent translator runaway.

2.2.4 Eddy Current Brake

The eddy current brake serves as both the turbine load and the turbine torque meter. It consists of two components: a cylindrical, Inconel drum directly attached to the rotor shaft and a stationary array of DC excited electromagnets arranged circumferentially around the drum. Electric currents are induced in the drum as it rotates through the applied magnetic field. The flow of this current through electrical resistance of the drum dissipates the power produced by the turbine which appears as resistive heating of the drum. Turbine speed is controlled by setting the magnitude of the applied magnetic field.

The braking system was modified by Keogh, [14], to serve as a shaft torque meter. The electromagnet assembly was mounted on bearings and reacting the braking torque measured through two load cells.

2.2.5 Critical Flow Venturi Nozzle

A critical flow venturi, developed and installed by Keogh [14] and Spadaccini [22] in line with the exit flow path, is used to measure the mass flow rate through the turbine. The nozzle design and upstream duct requirements are based upon the ANSI standard, [3], for torroidal

throat critical flow venturi. Modifications to the facility were required to meet installation requirements for the nozzle. A 66 in. extension was added between the dump tank and main frame in order to relocate the eddy current brake and starter motor. Extensions were also required to connect the boundary layer bleeds to the dump tank, and to connect the fill system to the supply tank.

A 50% open area screen is installed at the entrance to the upstream duct. This reduces the total pressure non-uniformity caused by the stepped transition from annular to circular cross section around the starter motor. The nozzle was calibrated with the upstream duct and a simulated blockage in place.

The nozzle was designed and built by Flow Systems Inc. of Boulder Colorado and calibrated by Colorado EESI. This calibration is traceable to the National Institute for Standards and Technology (NIST). A cross section of the critical flow venturi nozzle is shown in Figure 2-1.

2.2.6 Coolant Feed System

The coolant system consists of a coolant supply tank, a fast-acting pneumatic ball valve, a pipe network, and several orifice plates for metering the flow. Like the facility itself, the cooling system operates in a blowdown mode. The existing facility coolant system was modified by Spadaccini [22] to provide three independent and separately metered streams to the rotor blades, vanes, and tip casing.

The coolant supply tank is 3.97 cu. ft. and has a pressure rating of 450 psia. Like the main supply tank, it is surrounded by a metal jacket and insulation for controlling tank temperature. A flow of liquid nitrogen mixed with compressed air is used to cool the tank lining and the test gas to the desired temperature. The fast-acting ball valve at the tank exit is actuated by a 1000 psi argon bottle. It is triggered simultaneously with the main valve and closes approximately 1.2 seconds later. The piping network feeds the coolant from the supply tank into the test section and to the turbine.

An overhead view of this network can be seen in Figure 2-5. Three independent feeds are employed. One each to the rotor blades, nozzles, and tip casing. The flow is split in a manifold downstream of the ball-valve. Each split is metered by a thick, square edged, choked

orifice with known discharge coefficient which accurately sets the mass flow ratios to each turbine component.

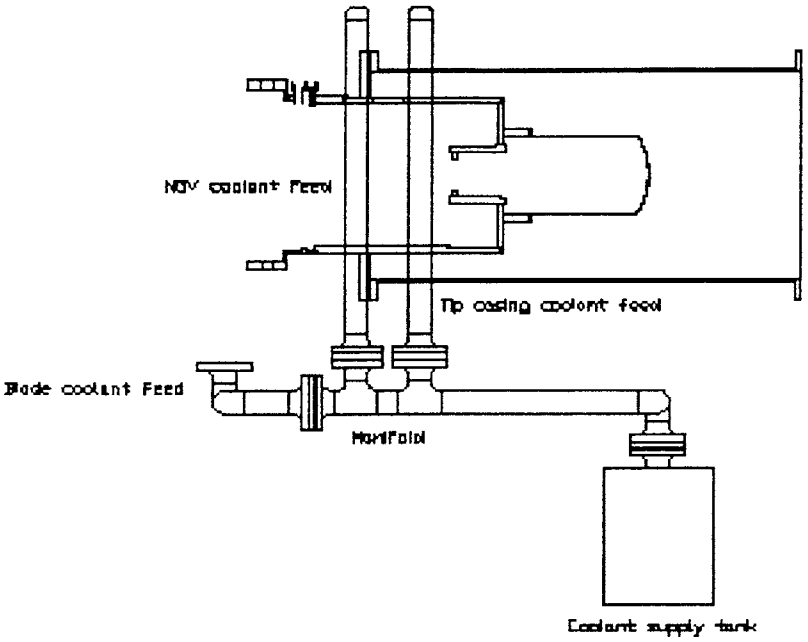

Figure 2-5: Coolant Feed System

2.2.7 Film-Cooled Turbine Stage

In order to modify the uncooled turbine stage for coolant flow injection, the ¼-scale film-cooled model turbine was required to have similar external geometry, including the film hole quantity, distribution, diameters, and injection orientations over the airfoil surfaces. The internal passages were not directly replicated since the focus of the program was on external heat transfer. Extensive work was done by Keogh [14] and Spadaccini [22] to modify the previously existing, non film-cooled turbine stage. Sophisticated machining techniques, including electrical discharge machining (EDM) and laser machining, were employed.

The nozzle guide vanes, turbine blades, and the tip casing were modified. Nozzle guide vanes were retrofitted with 12 rows of coolant injection holes on the airfoil surface, as well as several holes on the upper and lower platforms. Two vertical channels were required to feed all the airfoil surface cooling holes. Coolant was supplied to the platform holes via manifolds above and below the locations where the vanes mate to the facility. The scaled film-cooled turbine blades consist of five rows of coolant injection holes: two on the leading edge, one on the

suction surface and one on the pressure surface. The leading edge holes are also oriented at compound angles. Although not used for this experiment, the rotor tip casing was modified with film-cooling holes on the leading and trailing edges of the tip casing ring.

2.3 Scaling of Test Conditions

Validity of scaled wind tunnel experiments depends on the similarity between the test flow and the actual flow being simulated. In dimensionless form, the equations for mass continuity, momentum and energy transfer produce non-dimensional parameters that completely characterize the physics of flow field. Similarity between experiment and reality only requires that these non-dimensional parameters be reproduced.

For an uncooled turbine stage operating under adiabatic conditions, corrected mass flow and total temperature ratio (or efficiency) depend on four dimensionless parameters: total pressure ratio, corrected speed, Reynolds number, and specific heat ratio, [9]. Two additional parameters are required to simulate the heat flux distribution: the gas-to-wall temperature ratio and the Prandtl number. For a film-cooled turbine test, the coolant mass and momentum flux ratios must also be reproduced. These parameters, which govern test similarity, can be matched by properly setting the facility initial operating conditions.

The operating conditions consist of the test gas composition, upstream total temperature and pressure, coolant total temperature and pressure, mechanical speed, throttle area, and brake excitation. The supply tank temperature is set by matching the gas-to-wall temperature ratio. Specific heat ratio is matched by setting the test gas mixture ratio, typically *Argon* and CO_2. Shaft mechanical speed is set by matching the corrected speeds. Initial supply pressure is set by the Reynolds number, and pressure ratio by the downstream throttle position. Table 2-1 summarizes the conditions of a typical blowdown experiment and compares them to that of a full scale engine.

Table 2-1: MIT Blowdown Turbine Scaling

Parameters	Full Scale Engine	MIT Test Facility
Working Fluid	*Air*	*Argon – CO_2*
Ratio of Specific Heats	1.28	1.28
Mean Metal Temperature	1100 K	300 K
Metal to Gas Temp Ratio	0.647	0.647
Inlet Total Temperature	1700 K	464 K
Reynolds Number	$5.6\ 10^6$	$5.6\ 10^6$
Inlet Total Pressure	15 atm	7 atm
Exit Total Pressure	7.4 atm	3.47
Exit Total Temperature	1470 K	401 K
Prandtl Number	0.928	0.742
Design Rotor Speed	3600 rpm	5954 rpm
Design Mass Flow	312 kg/s	23.3 kg/s
Coolant/Inlet Flow	9.8%	9.8%
Stage Power Output	91 MW	1.26 MW
Test Time	Continuous	$\approx$ 0.800 s

2.4 Test Procedure

Preparations for a blowdown experiment begin by determining the required conditions for achieving full-scale turbine operating point. These consist of the upstream total temperature and pressure, coolant total temperature and pressure, test gas composition, mechanical speed, throttle area, and brake excitation. The experiment then proceeds as follows:

1. The entire facility is evacuated and the throttle plate is positioned for a predetermined area based on operational experience.
2. The main supply tank is heated to the desired upstream total temperature and is brought to thermal equilibrium.
3. The main valve is sealed and the supply tank is filled with the required test gas mixture to the desired upstream total pressure.
4. Simultaneously, the coolant supply tank is filled to the desired pressure and cooled to the predetermined temperature.
5. At this post-fill state, all differential pressure transducers are calibrated by cycling their back-pressure ports between vacuum and atmosphere. This provides a scale factor for

each transducer. Instrumentation and calibration are discussed in further detail in section 2.5.

6. The brake excitation is set.
7. The data acquisition system and translator servo-motor controller are set to stand-by mode and are waiting to be triggered.
8. The turbine rotor is then accelerated to the desired mechanical speed by a starter motor.
9. Once this speed is exceeded, the motor is powered down and the rotor spins freely in the vacuum. It is slowly decelerated by bearing friction and the applied back EMF of the drive motor.
10. When the decelerating rotor reaches the preset speed, a trigger occurs causing the main valve and coolant ball valve to open. Simultaneously, the data acquisition system begins collecting data, the downstream translator begins it traverse, and the eddy current brake torque meter is energized.
11. The test gases then flow through the test section and quasi-steady state operation is reached after a 300 ms transient. The useful test window is approximately 500 ms.
12. After approximately 1.2 seconds the coolant ball valve closes and the brake is turned off.
13. The rotor decelerates and comes to a stop.
14. Once the gas inside the tunnel stabilizes, all differential pressure transducers are re-calibrated to check for drift.
15. The tunnel is then re-evacuated and cooled to room temperature.

2.5 Instrumentation

2.5.1 Introduction

The facility was designed to provide a rather benign experimental environment for flow measurement. The nature of the short duration experiment casts a strict requirement on the time response of instrumentation used to sample its flow field. Performance calculations based on these measurements also require a high level of instrumentation accuracy. These considerations led to the development of highly accurate total temperature and pressure instrumentation with the capability of accurately characterizing turbine performance.

2.5.2 Total Temperature Instrumentation

The MIT Gas Turbine Laboratory has engaged in the development of total temperature probes for use in turbine aero-performance measurements in the Blowdown Test Facility. With each new design, time response and instrument accuracy generally improved. Work focused on reducing the transient errors resulting from the heat transfer processes within the thermocouple junction support wires and led to a design with much faster time response than previously achieved. Attention was also paid to the probe head design to reduce probe sensitivity to flow angle, which is important for downstream wake measurements.

Details of the temperature probes are shown in Figures 2-6 and 2-7. The measurement heads consist of 0.0005 in. diameter type-K thermocouple junctions mounted in vented stagnation tubes. The rake probe shown in figure 2-7 is mounted on the downstream translator and contains an internal temperature reference junction. An identical probe with four heads is also mounted on the downstream translator and a stationary six head version is mounted upstream of the turbine. The radial rake of 6 heads is positioned roughly mid-way between two of the facility's inner annulus support struts. The inlet rake can employ either an internally mounted or external reference junction.

Three additional single head probes, spaced 120° apart, are mounted upstream at mid-span on the inlet annulus. The thermocouple reference junctions for these probes are external. Three total temperature probes are dedicated to monitoring the flow through the critical flow venturi nozzle. These probes are also 0.0005 in. diameter type-K thermocouples and have similar time response and accuracy to the upstream probes.

The cooling system is instrumented with seven type-K thermocouples. These probes do not require the time response of the turbine inlet and outlet sensors and employ 0.003 in. junctions. These probes are located at points upstream of the choked metering orifices and as close as possible to where the coolant enters the test section.

With the exception of the turbine inlet and outlet rakes, all thermocouples are referenced to Omega TRCIII ice point cells. The signals are processed using high stability DC amplifiers and filters prior to being recorded by the data acquisition system. The long term static accuracy of the system—consisting of the measurement head, reference junction and signal conditioning electronics—is 0.13 K.

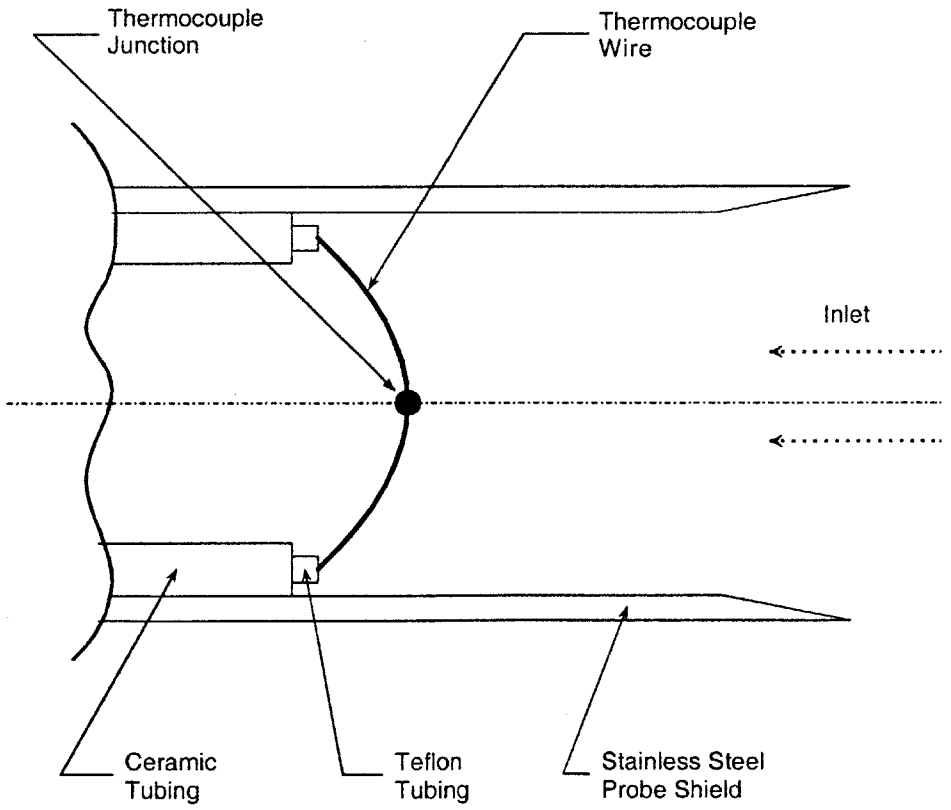

Figure 2-6: Temperature Probe Head Detail

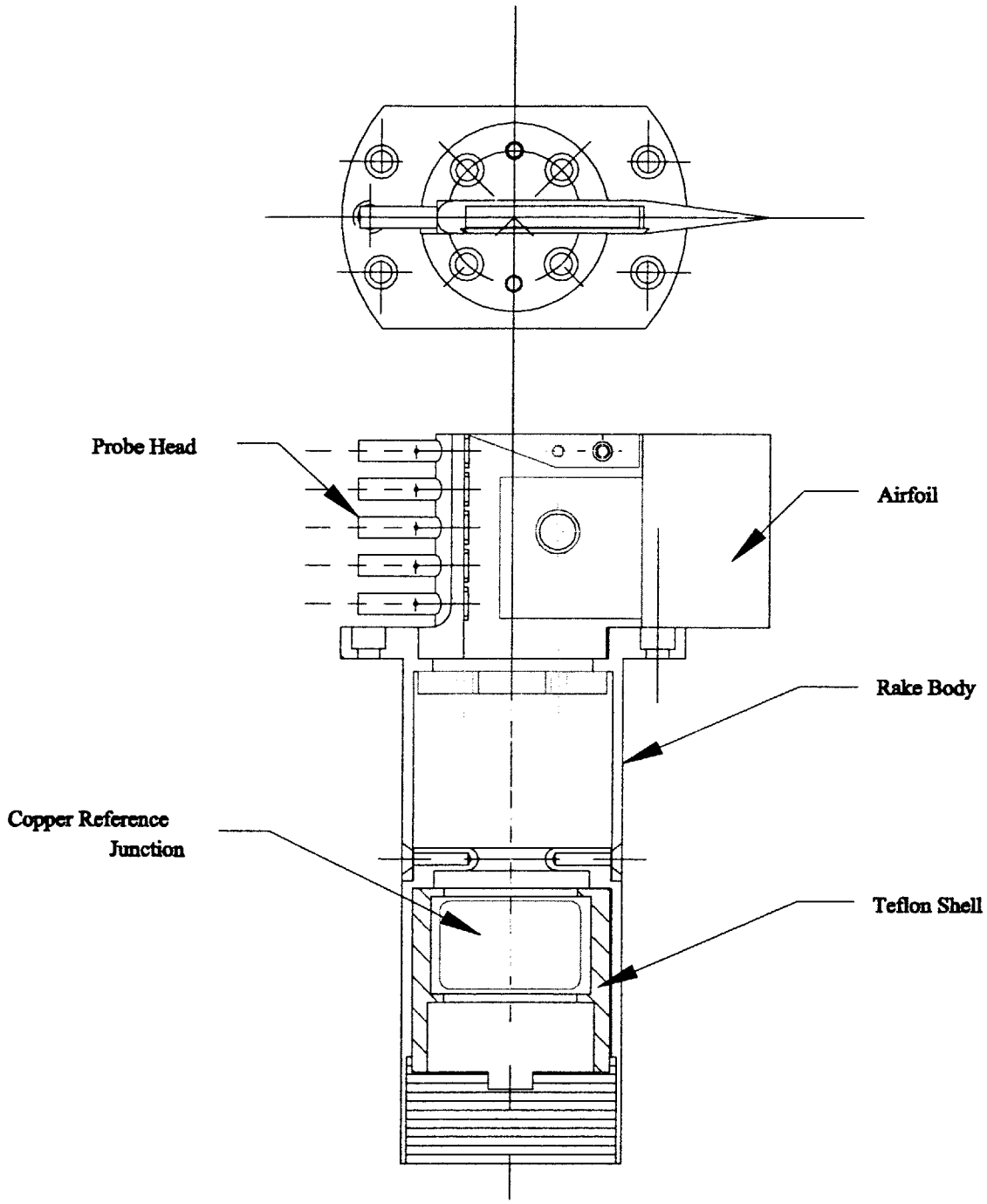

Figure 2-7: Downstream Total Temperature Rake

2.5.3 Total Pressure Instrumentation

The primary concerns in the design of the total pressure sensors for this facility are fast time response and flow angle insensitivity. Flow angle sensitivity is particularly important for downstream measurements where the probes are circumferentially translated through the NGV wakes. To achieve the desired time response, semiconductor strain gauge type pressure transducers, manufactured by Kulite, were used. A disadvantage of these transducers is their tendency to drift with changes in temperature. As a consequence, extensive run-time calibration routines were developed and used during every experiment. To allow a larger range of inlet flow angle to the probe head, either vented Keil type or 15° beveled impact heads were employed. Acceptable flow angles are estimated to be ±27.5°.

Downstream of the turbine stage a rake type pressure probe with eight 15° beveled impact heads is employed to survey the pressure in the radial direction. The probe is mounted on the downstream translator to resolve flow characteristics in the circumferential direction. The pressure transducers, (100psig XCQ-063-100), are mounted inside the probe body below the heads. Transducer reference backpressure is provided via a tubing arrangement within the translator. The estimated average uncertainty in total pressure measurement from these heads is 0.25%. More information on the design of this probe is available in [5].

In addition to this rake, there are differential sensors located upstream of the turbine and in the supply, coolant, and dump tanks. There are also several highly accurate (0.05%) Sensotec pressure sensors mounted throughout the facility for calibration reference. The coolant system is instrumented with several lower accuracy (0.1%) Sensotec transducers.

2.5.4 Nozzle Guide Vane Static Pressure Taps

To take static pressure measurements on the hub and tip region of the platform surfaces of the nozzle guide vanes, one NGV is instrumented with static pressure "taps" on the platform hub and tip surfaces. Four through holes were drilled into each platform surface one-quarter nozzle pitch apart. On the tip end, tubulations are bonded into grooves machined into the outer manifold support of the nozzle cassette. For the hub static tap, stainless steel tubes are bonded onto the top and run through the NGV's cooling plenum. The outer manifold support of the nozzle cassette was modified with a feed through hole to allow access to the static tap tubulations. With an access window removed, the tubulations are visible and accessible, as

shown in Figure 2-8. Nylon tubing connects each of four hub and four tip tubulations and is passed through Cajon fittings. The nylon tubing connects to brazed brass tubes on a brass support piece, which hold the tubes in place and provide a seal. Additional nylon tubes connect the brass tubes to a Scanivalve Direct Sensor Array pressure-monitoring device. To maximize frequency response and measurement fidelity, the DSA is placed as close to the tubulations as facility construction permits. This work is part of concomitant research on the MIT Blowdown Turbine and is ongoing.

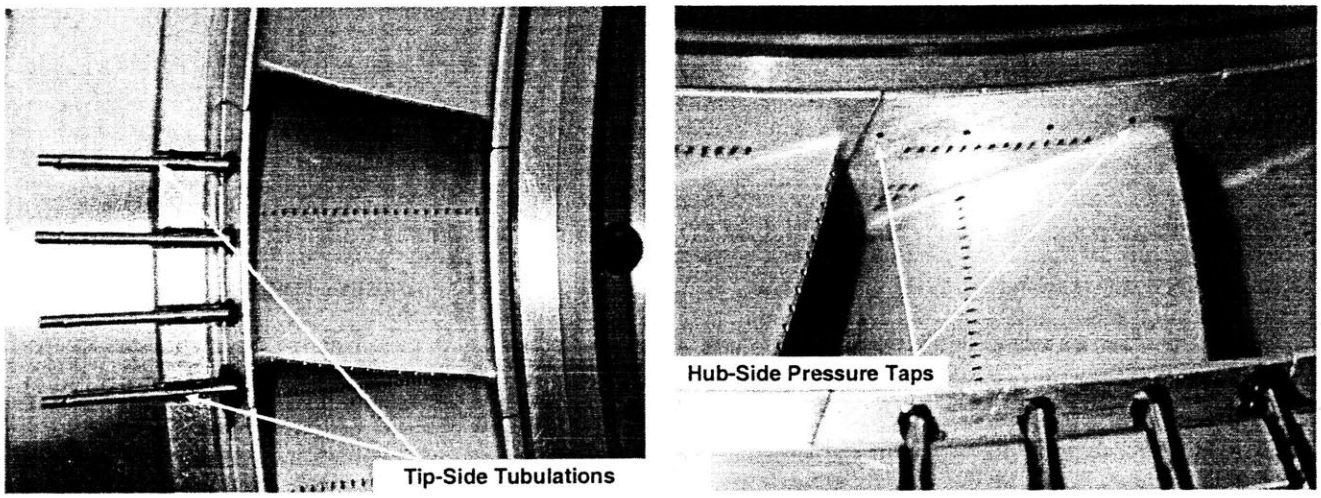

Figure 2-8: Static Pressure Taps

2.5.5 Tip Casing Heat Transfer Instrumentation

Heat transfer instrumentation was developed and fabricated for the project to measure the heat flux to the tip casing. Instrumentation design and construction is detailed in Chapters 3 and 4.

2.5.6 Other Instrumentation

Turbine speed and translator position are monitored by their respective digital encoders. The optical shaft encoder consists of two rings of 366 divisions per revolution in quadrature and a once per revolution ring. It is directly mounted to the turbine shaft. Both digital and analog circuitry process the encoder signals to provide shaft position and velocity for storage by the computer data acquisition system.

Two piezoelectric sensors are mounted on the bearing housing to record shaft vibration during an experiment.

The eddy current brake torque meter is instrumented with two load cells that provide a measure of shaft torque. The brake voltage and current are also recorded by the data acquisition system. A list of all instrumentation is provided in Table 2.2.

Facility reference instrumentation provides known conditions for use in the calibration procedures. For these, time response is traded for absolute accuracy and stability since all tunnel temperature and pressure measurements are based on these references. Pressure references are available in the supply tank and test section via slower, but more accurate capacitive type pressure transducers. Located on the supply tank is a Sensotec Super TJE 150 psia (0.05%) transducer. A Sensotec TJE 50 psia (0.1%) transducer is located in the critical flow venturi. The upstream Pitot probes are referenced to a Setra Model 228 1 psid capacitive type pressure transducer. Temperature calibrations are referenced to a Rosemount Standard Platinum Resistance Thermometer Model 162N100A (S/N3779), and when possible thermocouples are referenced to Omega TRCIII ice point calibration cells. Efforts are now being made to convert all temperature references to the ice point to simplify temperature data reduction.

Table 2-2: Blowdown Turbine Instrumentation

Sensor	Type	Location
Facility Reference		
PFEF300	300 psia, Sensotec: STJE/1835/15 S/N: 589494	Calibration: Coolant Tank / Facility Run Time: Coolant Tank Initial Pressure
PREF150	150 psia, Sensotec: STJE/1833-12-04 S/N: 587965	Calibration: Supply Tank / Facility Run Time: Supply Tank Initial Pressure
PREF050	50 psia, Sensotec: TJE/0713-04TJA-12 S/N: 631656	Calibration: Facility Run Time: Critical Flow Venturi, Test Section Initial Pressure
PREF001	1 psid, Setra: 228-1 S/N:708984	Calibration: Inlet Pitot Tubes
TREF3997	Rosemount Model 162N100A, S/N3779 Standard Platinum Resistance Thermometer	Standard Calibration Reference
TREF10	0-100 °C Platinum RTD	Run Time Reference
Supply Tank		
PT0A	150 psid, pressure, Kulite	Supply Tank, Internal
PT0B	150 psid, pressure, Kulite	Supply Tank, Internal
TT0A	600 °F temperature, type J T/C	Supply Tank, Internal
TT0B	600 °F temperature, type J T/C	Supply Tank, Internal
TT0C	600 °F temperature, type J T/C	Supply Tank, Internal
Shaft Monitoring		
FTACH	Speed, Digital	Shaft/Bearing Assembly
ATACH	Speed, Analog	Shaft/Bearing Assembly
FBRING	Vibration, forward	Shaft/Bearing Assembly
RBRING	Vibration, rear	Shaft/Bearing Assembly
Eddy Current Brake		
VTOT	Excitation Volt	External
ITOT	Total Current	External
IBRK	Excitation Current	External
ECBF1	Load Cell #1	Internal
ECBF2	Load Cell #2	Internal
Main Valve		
PVLV	450 psia Kulite	Valve Damping Chamber
XVLV	0-8 in Linear Potentiometer	Valve Slider
Turbine Inlet		
PT2x, (x=A,B,C)	Total Pressure	Main Frame, 120° apart
TT2x. (x=A,B,C)	Total Temperature	Main Frame, 120° apart
PP2x, (x=A,B,C)	Dynamic Pressure	Main Frame, 120° apart
PTYRn, (n=1,2,3,4,5,6)	Total Pressure, 6 head radial rake	Main Frame, fixed location
TTR101-n,(n=1,2,3,4,5,6)	Total Temperature, 6 head radial rake	Main Frame, fixed location

Table 2.2: Blowdown Turbine Instrumentation, continued

Sensor	Type	Location
Turbine Outlet		
PT45Rn,n=1,2,3,4,5,6,7,8	Total Pressure, 8 head radial rake	Downstream Translator
TTR103-n, n=1,2,3,4,5	Total Temperature, 5 head radial rake	Downstream Translator
RTD103-n, n=1,2	T/C Reference RTD's, 2 locations	Downstream Translator
TTR104-n, n=1,2,3,4	Total Temperature, 4 head radial rake	Downstream Translator
RDT104-n, n=1,2	T/C Reference RTD's, 2 locations	Downstream Translator
P45HUB	50 psid wall static pressure	Downstream Translator Hub
P45A	50 psid wall static pressure	Main Frame Window
Critical Flow Venturi		
PREF050	Static Pressure	Venturi Inlet
PNOZ	Static Pressure	Flow Conditioning Nozzle
TTMFM1	Total Temperature	Venturi Inlet
TTMFM2	Total Temperature	Venturi Inlet
TTNOZ1	Total Temperature	Flow Conditioning Nozzle
TTNOZ2	Total Temperature	Flow Conditioning Nozzle
Dump Tank		
PDMP	Static Pressure	Dump Tank
Cooling System		
PREF300	300 psia, Sensotec: STJE/1835/15 S/N: 589494	Coolant Supply Tank
PTC0	300 psia Kulite	Coolant Supply Tank
PTC1	Total Pressure, 300psig Sensotek	Coolant Supply Manifold
PTC2V	Total Pressure, 100psig Sensotek	Vane Feed Manifold
PTC2B	Total Pressure, 100psig Sensotek	Blade Feed Manifold
PCCV	Static Pressure, 100psig Sensotek	Vane Feed Entrance
PCCC	Static Pressure, 100psig Sensotek	Tip Casing Entrance
TTC0	Total Temperature	Coolant Tank Exit
TTC1	Total Temperature	Coolant Supply Manifold
TTC2B	Total Temperature	Blade Feed Manifold
TTCBV	Total Temperature	Vane Feed Entrance, B window
TTCBC	Total Temperature	Casing Feed Entrance, B window
TTCCV	Total Temperature	Vane Feed Entrance, C window
TTCCC	Total Temperature	Casing Feed Entrance, C window

2.6 Pressure Transducer Calibration

A standard calibration procedure is responsible for the calibration of all differential pressure transducers. It is performed immediately after the supply tank is filled and at the conclusion of each experiment. Calibrating data just before and after each experiment allows transducer drift and non-linearity to be quantified. Figure 2-9 shows a typical calibration trace of a differential pressure transducer. This figure and the calibration sequence are described below.

1. All transducers are provided a vacuum back-pressure reference by an external vacuum pump. For a post-fill calibration this produces a zero pressure differential across the transducers which are located inside the tunnel. For those in the supply or coolant tanks, a pressure differential equal to the initial tank pressure is recorded.
2. Data is taken at this condition for approximately two minutes as shown by the first segment of the trace in Figure 2.9.
3. After two minutes, the back-pressure reference is exposed to atmospheric pressure. Data is acquired for two minutes as shown in Figure 2.9.
4. After four minutes, the back-pressure reference is returned to vacuum where it remains for the experiment.
5. This procedure is repeated after the blowdown experiment has been completed.

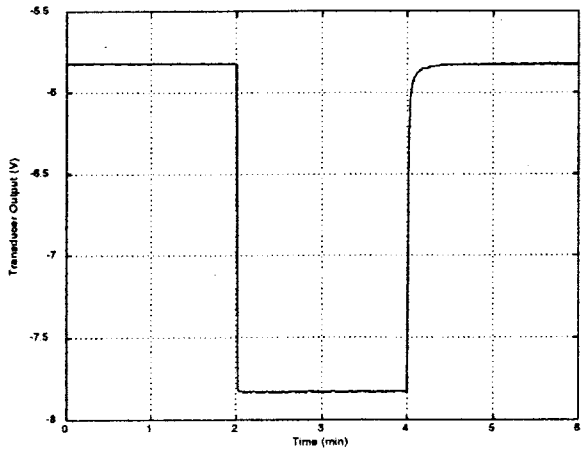

Figure 2-9: Typical Differential Pressure Calibration Trace

This data provides a voltage change for each differential transducer which corresponds to the local atmospheric pressure. A transducer scale factor can then be computed. Transducer zeros are taken to be the average output prior to the opening of the main valve. The scale and zero can then be used in the data reduction process via the linear calibration relation.

2.7 Data Acquisition

The short duration nature of the blowdown experiment not only places special requirements on instrumentation, but on data acquisition (DAQ) as well. The DAQ systems must monitor all instrumented channels at a sampling rate sufficient to capture all time scales of interest for the duration of the experiment. For aerodynamic performance measurements, 5 kHz data sampling is sufficient to resolve the necessary time scales; however, for heat transfer measurements, a 200 kHz high speed system is necessary. The 200 kHz high-speed system is often utilized to accurately monitor turbine speed. The DAQ envelope typically spans 2-4 sec. to record useful data and monitor tunnel 'spin-down.' The precise clocking sequence can be modified to capture the desired window. In addition, the post-test calibration lends further insight into the post-test tunnel state.

The data acquisition system monitors all instrumented channels at a sampling rate sufficient for capturing time scales of interest during the experiment. The system typically acquires data for 2-4 seconds depending on the experimental conditions being monitored. The current hardware includes a Pentium II 450 MHz computer which is programmed with LabVIEW lab automation software.

The current DAQ system consists of four computers. The low-speed system, which is capable of monitoring up to 64 channels, samples at 2.5 kHz and 5 kHz. The high-speed system monitors eight channels at up to 200 kHz. An IBM ThinkPad laptop computer collects NGV static pressure data. Table 2.3 summarizes the Blowdown Turbine DAQ equipment.

Table 2.3: Blowdown Turbine Data Acquisition

Specification	AST 4/66D A	AST 4/66D B	IBM PII 450	IBM ThinkPad 386CD
System	1	2	3	4
Speed	High	High	Low	Low
Operating Sys.	Dos	Dos	NT 4.0	Windows 95
DAQ Platform	In-House	In-House	LabView	DSALink 2
DAQ Board	ADTEK AD-830	ADTEK AD-830	NI MIO-64E3	
Resolution	12-bit	12-bit	12-bit	
Board Channels	8	8	64	16
No. of Boards	4	3	1	1
Total Channels	32 simultaneous	24 simultaneous	64 multiplexed	16
Sampling Rate	200 kHz	200 kHz	5 kHz	200 Hz

2.8 Summary

This section has discussed the MIT Blowdown Turbine short duration experimental facility used to acquire turbine data for calculation of adiabatic efficiency. It has covered run-time preparations including determination of blowdown operating conditions to achieve full-scale turbine similarity. Total temperature and pressure instrumentation for highly accurate flow field measurements was briefly discussed along with other instrumentation used to characterize turbine performance. This was followed by descriptions of the standard differential pressure transducer calibration procedure and the downstream translator, a device for circumferentially surveying the downstream flow field. This section concludes with information on Blowdown Turbine data acquisition system.

Chapter 3

Heat Flux Gauges

3.1 Introduction

The design and implementation of heat flux instruments was of chief importance to this research effort. The following sections outline the development from concept through fabrication of the semi-infinite heat flux gauges for measuring heat transfer to a turbine tip casing. A simple reduced order model is presented to identify some criteria for material selection and gauge design. Gauge fabrication procedures conclude the chapter.

Two methods of measuring surface heat flux have recently been used in the MIT Gas Turbine Laboratory: a) multi-layer thin film gauges and b) thin film semi-infinite gauges. Guenette [9] fabricated multi-layer gauges by plating nickel temperature sensors onto both sides of 25 μm polyimide (Kapton) film; these gauges were used on tip casings and rotor blades. Kirk[1] constructed semi-infinite thin film gauges using platinum paint on machineable ceramic (MACOR) to detect the presence of a reacting flow in flat plate film-cooling schemes. With institutional knowledge available, as well as documented success, variations of these techniques were explored for use in this project.

The goals of this research required measurement of both time-averaged and time resolved (blade passing) heat flux to the turbine rotor endwall. The design criteria for the heat flux gauge development required that it must:

1. Be easily adaptable to the facility

---

[1] Ongoing research in the MIT Shock Tunnel Facility by D.R. Kirk and G.R. Guenette to study Reaction Effects on Film-Cooled Flat Plate Heat Transfer

2. Be compatible with the operating conditions (450 K gas temperature)
3. Have frequency response from DC to 5 times blade passing frequency
4. Be small in scale (about 20-30 gauges along an approximately 1.5" by 1" instrumentation region) to spatially resolve heat transfer
5. Minimize the disturbance in the flow field
6. Be simple to manufacture
7. Be replaceable in small denominations in the event of minor gauge failure

Both multi-layer and semi-infinite techniques were adaptable to the above criteria. Multi-layer gauges of deposited thin film metal on a sheet of 25 μm Kapton film have been used extensively in the MIT Blowdown facility. This technique imparts very little disturbance to the flow. Frequency response has been demonstrated to nearly 60 KHz through appropriate choice of substrate material and thickness. These gauges operate in a low frequency direct mode (direct measurement of upper and lower temperatures) and a high frequency mode (one-dimensional semi-infinite heat conduction based upon upper temperature). Notwithstanding these advantages, fabrication techniques have proven unreliable and difficult[2].

The semi-infinite gauge was chosen to measure heat transfer on the tip casing. Frequency response and robustness were demonstrated by Kirk [17] in conditions much more severe than the Blowdown Turbine facility. When aligned properly, these gauges also create minimal flow disturbances. An attractive feature of these gauges was their simplicity of fabrication and their relatively small size in the instrumentation region. Compared to the multi-layer gauges, semi-infinite gauges are much simpler to construct and were fabricated with in-house resources. They can be installed and removed individually to replace inoperative gauges. Many gauges could be installed in the same area—arrayed in rows and columns—to increase spatial resolution and illuminate both circumferential and axial variations in heat transfer.

[2] Improved multi-layer heat flux gauge fabrication technology is currently under development for use on film-cooled turbine blades

3.2 Semi-Infinite Heat Flux Gauge

The semi-infinite gauge is essentially a heat conducting substrate of known thermal properties combined with a surface temperature sensor. For applications where heat transfer can be considered one-dimensional within the body under investigation, the semi-infinite gauge is advantageous because it can be mathematically modeled to provide exact solutions of its internal thermal response to known external input heat load. Exact solutions were used to develop: a) the design criteria for the heat flux gauges and b) the calibration and data reduction techniques. This section discusses the gauge model and develops the background for gauge design criteria.

3.2.1 One-Dimensional Unsteady Heat Conduction Model

The heat flux measured by a particular gauge is modeled as one-dimensional unsteady heat conduction. Heat flux is assumed to be spatially uniform within the length scale of the gauge. The heat conduction equations are solved for a rod that appears semi-infinite in depth. The following assumptions apply:

1. Heat flow is uniform (one-dimensional)
2. Gauge thermometer and substrate make perfect thermal contact
3. Thermal penetration depth does not exceed gauge length (semi-infinite)
4. Gauge and substrate properties are uniform throughout.

If no heat is generated within the region of interest, the general equation governing the temperature distribution, T(x,t) is,

$$\frac{\partial T}{\partial t} = \kappa \frac{\partial^2 T}{\partial x^2} \tag{3.1}$$

where κ is the thermal diffusivity of the substrate. The initial temperature is assumed uniform:

$$T(x,0) = T_0 \tag{3.2}$$

and the semi-infinite condition requires that,

$$T(\infty,t) = T_0 \tag{3.3}$$

Since the tip casing may include both DC and periodic heat load components, temperature responses to both a step in surface heat flux and steady harmonic surface heat flux must be evaluated. The model provides exact solutions for both cases.

3.2.2 Response to Step in Surface Heat Flux

For a gauge suddenly subjected to a step in heat flux applied at the surface,

$$\dot{q}_s = \begin{Bmatrix} 0, t<0 \\ q_s, t>0 \end{Bmatrix} \tag{3.4}$$

the surface boundary condition becomes:

$$-k\frac{\partial T}{\partial x}\Big|_{x=0} = \dot{q}(0,t) \tag{3.5}$$

The solution to (3.1)-(3.5) gives the temperature distribution,

$$T(x,t) = \frac{q_s}{k}\left[\left(\frac{4\kappa t}{\pi}\right)^{1/2} e^{-x^2/4\alpha t} - x\left(erfc\frac{x}{(4\kappa t)^{1/2}}\right)^{1/2}\right] \tag{3.6}$$

Temperature distribution for a constant surface heat flux is shown in Figure 3-1 below.

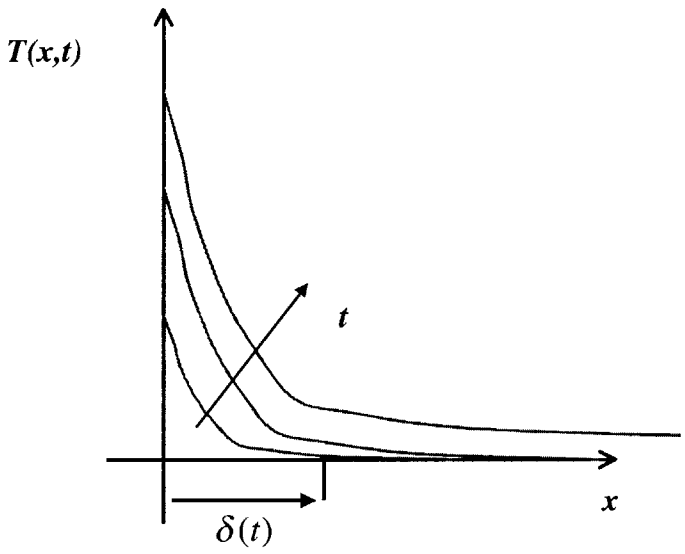

Figure 3-1: Response to Step in Surface Heat Flux

The thermal penetration depth, $\delta(t)$, is seen to be proportional to $\sqrt{\kappa t}$. It is noteworthy here to discuss the implications of this thermal penetration depth. In order for the semi-infinite condition—and thus equation (3.6)—to be valid in a region, δ must be smaller than the gauge length (L). Since the thermal penetration depth is a function of time, a time constant can be established based upon $\sqrt{\kappa L}$ to determine valid test windows. Thus, for times less than the time constant, the heat flux gauge can be considered semi-infinite and heat transfer data can be reduced from a surface temperature history commensurate with equation (3.6). The temperature response of equation (3.6) is portrayed graphically in Figure 3-2, contrasting the thermal penetration depth with the length of the gauge.

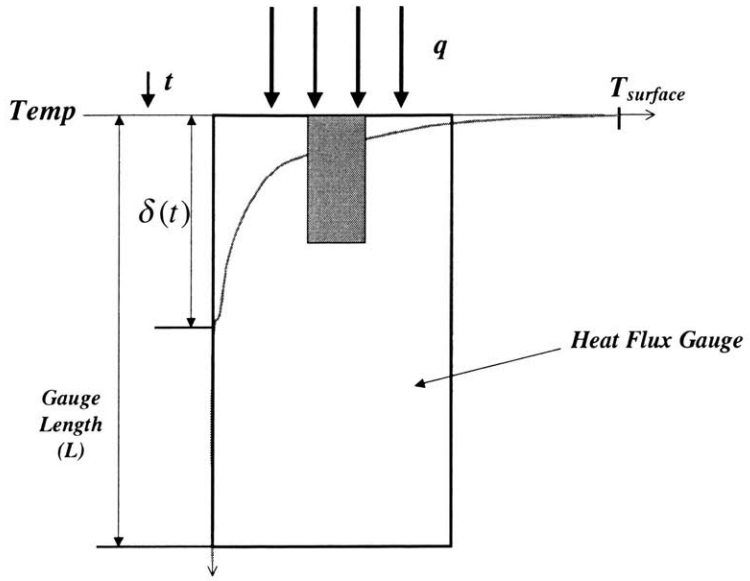

Figure 3-2: Thermal Penetration Depth

Equation (3.6) provides the temperature distribution in the heat flux gauge as a function of: the position *(x)* and time *(t)*; the heat flux applied (q_s); and the thermal properties of the gauge. Thus, to specify the temperature at any point and time, the thermal properties of the gauge must be accurately known. Written a different way, equation (3.6) becomes:

$$T(x,t) = \frac{2q_s}{\sqrt{\rho ck}}\left[\left(\frac{t}{\pi}\right)^{1/2} e^{-x^2/4\kappa t} - x\left(erfc\frac{x}{(4\kappa t)^{1/2}}\right)^{1/2}\right] \qquad (3.7)$$

The thermal properties of the gauge— ρ, c and k —form two parameters that govern its performance: 1) $\kappa \equiv k/\rho c$ governs the penetration and 2) $\sqrt{\rho ck}$ governs the sensitivity. The significance of $\sqrt{\rho ck}$ is illustrated in the surface temperature solution to a step in surface heat flux:

$$T_{surface} = \frac{2q_s}{\sqrt{\rho ck}}\left(\frac{t}{\pi}\right)^{1/2} \qquad (3.8)$$

Temperature sensitivity per unit of heat flux applied is proportional to $1/\sqrt{\rho ck}$. This relationship clearly shows that a low value for $\sqrt{\rho ck}$ is desirable for high sensitivity gauges.

3.2.3 Response to Steady Harmonic Variation in Surface Heat Flux

The passing of turbine blades imparts a time varying heat load on the tip casing. Previous experiments have shown the time-resolved heat flux to be rich in harmonics, with the fundamental component at the blade passing frequency. An exact solution is available for the case of a steady harmonic heat flux. The boundary condition describing this heat flux is:

$$q_s(t) = -k \left.\frac{\partial T}{\partial x}\right|_{x=0} = q_0 \sin(\omega t)\Big|_{-\infty<t<+\infty} \tag{3.9}$$

and the temperature distribution is found to be:

$$T(x,t) = \frac{q_0}{\sqrt{\rho ck}}\omega^{-1/2}\left(e^{-x\sqrt{\omega/2\kappa}}\right)\left(\sin(\omega t - x\sqrt{\omega/2\kappa} - \pi/4)\right) \tag{3.10}$$

Again, the temperature distribution depends upon time, position, and the thermal properties of the gauge material. As in the case of the step response, the thermal scale factor ($\sqrt{\rho ck}$) appears. For the temperature response due to a steady harmonic surface heat flux, $\sqrt{\rho ck}$ affects the frequency response of the heat flux gauges. As shown by Guenette [9], the impact of this factor can be readily seen in the temperature distribution of the surface ($x=0$). This gives:

$$T_{surface}(t) = \frac{q_0}{\sqrt{\rho ck}}\omega^{-1/2}\left(\sin(\omega t - \pi/4)\right) \tag{3.11}$$

Since the surface temperature response drops off as $\omega^{-1/2}$, lower values of thermal scale factor will improve the response for higher frequencies of heat load. As with the response due to a step in heat flux, a low value of $\sqrt{\rho ck}$ also increases gauge sensitivity ($\Delta T/q$).

3.2.4 Gauge Material Selection

In addition to thermal properties, durability and machineability were also considered in selecting the substrate material. It was desirable to develop a fabrication method that could be easily mastered and executed with in-house resources. Materials that could be easily machined were given strong consideration. Of the materials evaluated, Machineable Ceramic (MACOR) was chosen. MACOR has a low value of $\sqrt{\rho ck}$, is widely available, and is simple to machine. Unlike glass pyrex, another candidate material, MACOR gauges were machineable in the lab.

The length scale of the gauge was given much consideration during the design phase. Gauges were desired to be as small as possible to maximize spatial resolution. However, mechanical design and fabrication constraints limited the size. An optimal size was selected by balancing spatial resolution and construction.

3.3 Temperature Sensor

The temperature sensor is a film resistance thermometer constructed of a material whose resistance is sensitive to temperature. When passing a current through it and observing the voltage drop, it can be used to accurately measure surface temperature. The criteria used to develop the thin temperature sensor include:

1. Thin Film Sensitivity and Stability
2. Thin Film Frequency response
3. Adhesion of Metal Film and Substrate
4. Abrasion resistance

These criteria will be discussed in this section.

The semi-infinite gauges are resistance thermometers mounted on a substrate. The temperature coefficient of resistivity (α) defines the sensitivity of the metal films to a change in temperature. Guenette [9] developed an extensive gauge model and used it to identify many design criteria for multi-layer thin film gauges.

Since $\alpha(T)$ is normally a very weak function of temperature for the metals considered, the change in resistance with temperature can be expressed as:

$$\Delta R = R\alpha\Delta T \tag{3.12}$$

This change in resistance can be measured with analog devices, appearing as a voltage drop. For a constant current circuit, the voltage drop across the metal film gauge becomes:

$$\Delta V = (V\alpha)\Delta T \tag{3.13}$$

If the gauge sensitivity is now defined as the ratio of the voltage drop to temperature change, it is clearly evident that this sensitivity is directly proportional to both the excitation voltage (V) and the temperature coefficient of resistivity :

$$\frac{\partial V}{\partial T} = V\alpha \tag{3.14}$$

Equation (3.14) shows that excitation voltage and metal film coefficient of resistivity are important variables in gauge design. Thus, for high sensitivity, a metal film must have high temperature coefficient of resistivity (α).

The ability of the metal film to dissipate the heat generated by resistive heating is an additional factor in gauge design. The resistive heating—V^2/R—can be written as a heat flux:

$$q_0 = \frac{V^2/R}{(lw)} \tag{3.15}$$

where l and w are the sensor length and width, respectively. This heat flux represents a disturbance, and therefore must be kept small compared to the heat flux being measured by the thin film gauges. Additionally, Kirk [17] discovered that metal film gauges can "burn out" if excited by too high an excitation voltage.

Platinum was chosen as the metal film for the sensor due to its availability for use with ceramics. Platinum has high resistivity and temperature coefficient. When painted onto a substrate and then baked on at high temperatures, platinum retains its thermal properties well. Coated with a thin layer of protective strain gauge glue, the platinum thin film becomes nearly impervious to abrasions. Platinum thin films give reasonably high resistances and good resistance stability, and platinum paint was also available at a reasonable cost.

3.4 Fabrication

The thin film temperature sensors were fabricated using a widely used and proven technique. A platinum-in-oil suspension was painted on the MACOR and fired in a kiln. This technique has been used to produce heat transfer gauges since the 1950's [23]. Additionally, the ongoing research of Kirk [17] in the MIT shock tunnel has validated the robustness of these gauges in an environment more severe than that of the MIT Blowdown Turbine. The choices of both substrate and thin film thermometer have proven reliable.

For fabrication, MACOR was procured in long cylinders close in diameter to the gauge diameter. The MACOR rods were first machined down to the precise outer diameter of a gauge, with a tolerance of 0.0015 in. or less. MACOR rods were cut to a length of 0.35 in. to allow

some length to protrude out of the back side (connector side) of the tip casing insert. Square grooves were cut in the side of each MACOR cylinder, as shown in Figure 3-4 below.

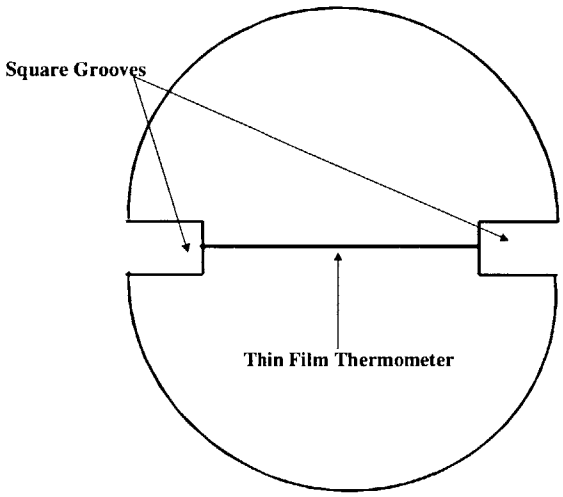

Figure 3-3: MACOR Cylinder Top View

The MACOR cylinder was initially cleaned and the top (gauge) ends were smoothed with pumice powder and dental floss. This edge must be rounded to facilitate current flow from the side of the gauge (from wire leads) to the top of the thin film thermometer. A sharp edge would pose a hurdle to current in the form of a discontinuity. Gauge cylinders were then thoroughly cleaned in an ultrasonic bath and dried in a low temperature oven.

Prior to painting on platinum, the MACOR cylinders were inspected for surface smoothness and rounded edges. Platinum was applied first to the top—the most critical painting step. Using a single-hair paint brush, the metal film was painted as a smooth and thin strip. The thin film top strip was then baked up to a temperature of 1200° F and then slowly cooled to avoid cracking of the MACOR and the platinum thin film. The baking temperature and cooling techniques were adopted from Vidal [23]. Following a post-bake microscope inspection of the thin film strip, side coats were painted in the square grooves. Figure 3-5 depicts the position of the side coat conductors with respect to the gauge. One layer was initially painted on both side grooves and then baked and cooled. Multiple layers were painted to achieve a thick coat of platinum. Since the platinum paint only serves to connect the top thin film to the wire leads, the resistance of the sides must be as low as possible to avoid introducing uncertainty to the gauges. Through experience, it was determined that four to five side coats of platinum paint reduced the

conductor resistance to less than 2 ohms. Side resistance surveys were conducted to ensure compliance.

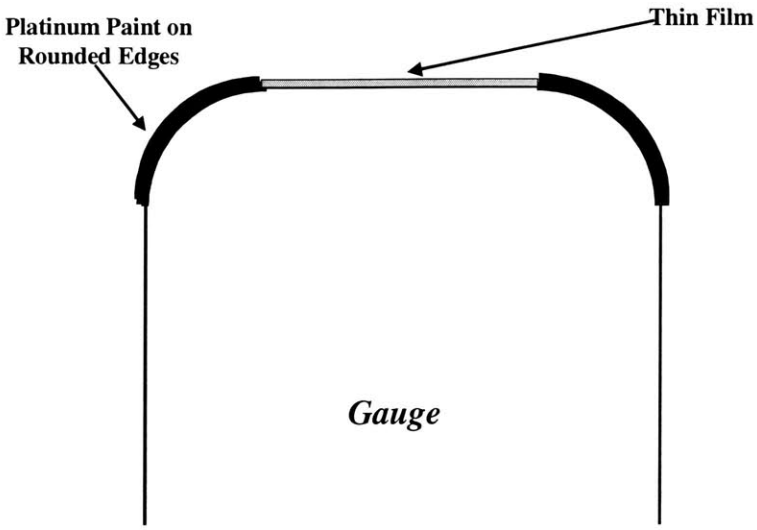

Figure 3-4: Gauge Side Cutaway View

In order to connect the gauge to a wiring board, 36-gauge insulated copper wire was soldered onto the side conductors of the gauges. The square grooves permitted an open space to feed these wires through to the wiring board. To protect the platinum top strip, a thin film of strain gauge glue was applied evenly to the top of the gauge. Once the protective coat was cured, gauge resistances were very stable and nearly impervious to abrasion and cracking. In experiments in the MIT Shock Tunnel, Kirk [17] demonstrated that the presence of the protective coating had a negligible effect on gauge sensitivity or frequency response. This thin glue layer is shown below in Figure 3-6

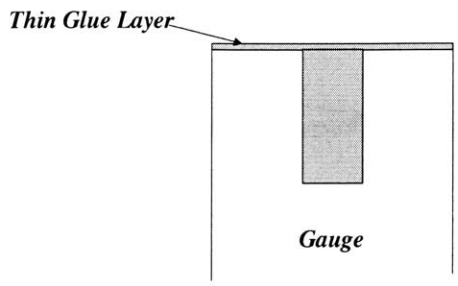

Figure 3-5: Side View Sketch showing Gauge Protective Coating

Gauges were tested for reliability and robustness by thermally cycling each gauge in an oven at temperatures similar to those encountered in turbine testing. Each gauge resistance was measured initially. Then all gauges were placed in an oven for ten minutes, cooled at room temperature, and resistances again measured. Most gauges were quite reliable, showing less than 1% deviation in resistance. Less than 10% of gauges were found to be unstable or inoperative during this initial thermal cycling.

Gauges were fabricated in groups of six or eight. In all, 64 gauges were built, with the best 32 chosen for use in the tip casing insert. The overages were stored for use as replacements. Chapter 4 provides more detail on the position and orientation of all 32 gauges with respect to the flow.

3.5 Summary

The preceding sections detailed the heat flux gauges used for the investigation of heat transfer to the tip casing of a power generation turbine. Beginning with a comparison of two instrumentation techniques, a semi-infinite type gauge was selected and justified for use in this research project. A semi-infinite transient heat conduction model was presented with solutions for both a step and a steady harmonic surface heat flux. The model was used to understand the temperature response of a gauge and the effects of material properties. Design criteria were identified from the model, providing convenient metrics for comparison of substrate materials.

An analysis of sensitivity yielded design criteria specifically for the metal film thermometer. Materials for both thin film and substrate were compared with respect to the design criteria identified. Finally, the method of gauge fabrication was outlined. The use of these gauges in the MIT BDT facility will be the subject of the next chapter

Chapter 4

Instrumented Tip Casing Insert

4.1 Introduction

In order to effectively measure heat transfer in the tip gap region, an instrumented tip casing insert (TCI) was developed. This chapter details the TCI from design through calibration. After reviewing the instruments contained within the TCI, the chapter concludes with fabrication and calibration sections.

4.2 Tip Casing Insert Design

Critical design considerations for the tip casing insert include:

1. Ease of insertion and installation
2. Minimal modification to the facility structure
3. Accommodation of wire leads from the TCI to the data acquisition system

The flow side (or sensor side) was designed to approximately match the curvature of the tip casing and be inserted in a cutout in the tip casing ring. The TCI curvature was designed for use with both 1.5% and 3.0% tip casing rings, resulting in negligible variations in fit. Figure 4-1 shows a three-dimensional view of the TCI.

The TCI was sized so that it could be inserted into the tip casing through an external window in the main frame of the test section with the facility assembled. The tight spacing between the main frame and tip casing ring precluded other installation techniques. Although somewhat difficult, this technique was favored due to its ability to easily pass wire leads from

the TCI out to the data acquisition system. Figure 4-2 shows the TCI inserted into the main frame.

The TCI was constructed from machined Aluminum. Gauge holes for both heat flux gauges and pressure transducers were drilled at angles to match the curvature of the tip casing. The TCI was gold anodized to eliminate the possibility of short circuits or interference between instrumentation and the TCI.

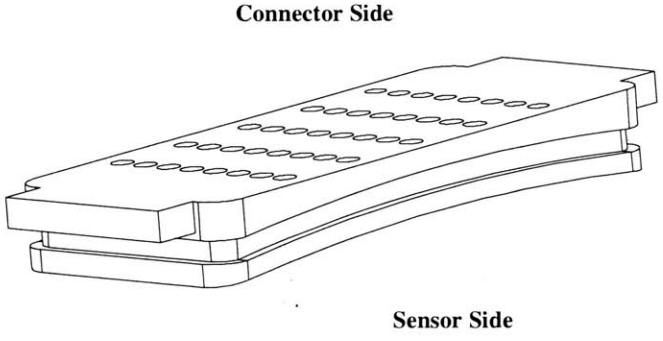

Figure 4-1: Three Dimensional View of TCI

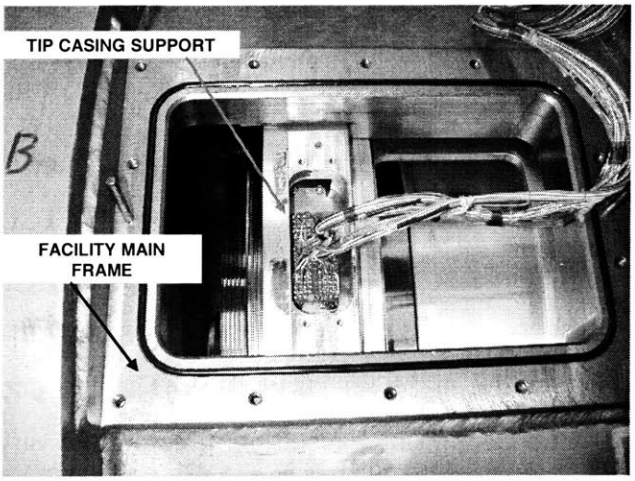

Fig. 4-2: TCI Inserted into Main Frame

Due to the fragility of the film-cooled turbine blades, an abradable coating was added to the tip casing and is known as the "rub strip." The rub strip protects the turbine blades and the

rotor from catastrophic damage that could be caused by a tip rub. In this vein, protective coating for the TCI was considered. Although no protective coating to the TCI was examined, the severity of instrument damage that would certainly result from even a slight tip rub eliminated this alternative. Several other possibilities were considered, including:

1. A thin sheet of polyimide (Kapton) film bonded on the surface
2. A thin sheet of rubber bonded on the surface
3. An abradable coating to match the existing coating on the tip casing

The final choice, and the one adopted, was a spray-on abradable coating identical to the coating on the rest of the tip casing. This alternative provided the best surface finish and the best bond onto the surface of the TCI. Additionally, the abradable coating eliminated concerns of downstream thermal disturbances due to a circumferential discontinuity on the tip casing. The sensor side of the TCI, with the gauges against the abradable coating, is shown in Figure 4-3.

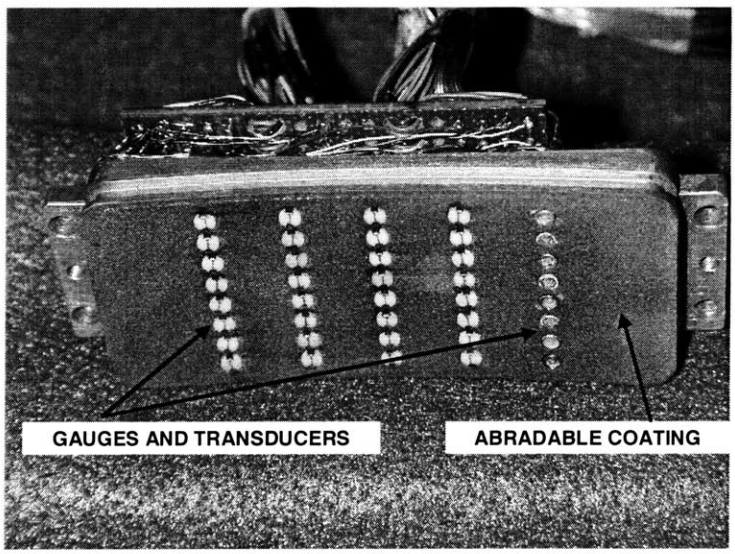

Figure 4-3: TCI Sensor Side

The TCI in the tip casing ring is portrayed in Figure 4-4, showing the matching abradable surfaces.

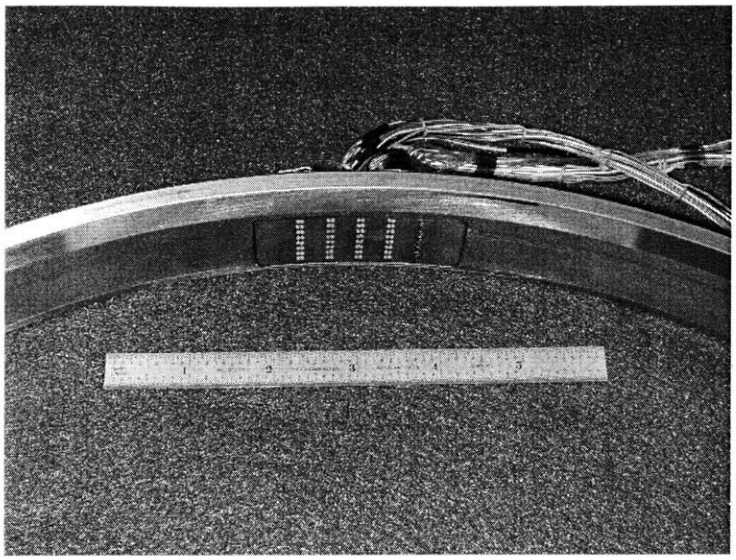

Figure 4-4: TCI in Tip Casing (Looking Upstream)

4.3 Instrumentation

4.3.1 Heat Flux Gauges

The heat flux gauges described in Chapter 3 were employed in the TCI. Thin wire leads were attached to bring the analog signal out to the data acquisition system. Chapter 3 provides the theoretical background for the gauges and details design criteria.

4.3.2 Pressure Transducers

The pressure transducers used were Kulite XCQ-062-100D differential pressure transducers. The Kulites measure pressure differential between the tip casing and backpressure tubes. These transducers were calibrated three times during the course of a run—before the supply tank was filled, after the supply tank was filled, and immediately after a test. These calibrations are discussed in greater depth in Chapter 2.

The transducers were placed in sheaths machined from stainless steel tubing. The ID of the tubes was machined to 0.066 in. to fit the 0.064 in. Kulites. The OD of the tubes was designed to fit snugly into the TCI. Transducers were bonded into the sheaths using epoxy. Back pressure tubes, made of Tygon tubing of 0.010 in. ID and 0.030 in. OD, were fitted onto

the back of the pressure transducers. All eight backpressure tubes were secured to the wiring harness and were brought outside for calibration.

The pressure transducers were specially ordered without front protective screens to improve the frequency response. For protection of the micro-scale strain gauge in the transducer, a thin coat of rubber was added. RTV11 was applied to the sensor surface of each Kulite prior to insertion into the TCI. The rubber coating was estimated to be 0.002 in. thick; the effect on frequency response was assumed to be negligible.

4.3.3 Resistance Temperature Detectors

The reference temperature devices were platinum thin film Resistance Temperature Detectors (RTDs). RTDs were used as accurate reference temperature devices to determine an accurate "zero" for all gauges. Prior to testing, the RTDs were calibrated in an oil bath against a NIST traceable reference thermometer. They measure the temperature of the entire TCI during both calibrations and test runs and provide reference measurements during a run. In addition, the RTDs give supporting verification that the tip casing has come to thermal equilibrium by the end of a run and is not in a thermal gradient. During a run, each heat flux gauge initial temperature is matched to the temperature read by an average of both RTDs.

4.3.4 Instrumentation Arrangement

Two possibilities for axial arrangement of heat flux gauges and pressure transducers existed: 1) along an axial line, or 2) along a blade chord line. The arrangement of blade chord line might have provided better resolution of tip passing effects than along a straight axial line. However, drilling instrument holes along a blade chord line would have greatly increased the complexity of machining the TCI. Since heat transfer gauge holes were drilled at angles to match the radius of the TCI, a blade chord arrangement would have required setting each hole angle individually. Thus, for simplicity, a straight axial line arrangement was used for both heat transfer gauges and pressure transducers. The effect of this arrangement on data resolution was estimated to be negligible.

The TCI was designed to hold three types of instrumentation: 1) heat flux gauges; 2) pressure transducers; and 3) resistance temperature detector (RTD) thermometers. Since the flow physics in this region may be influenced by the film-cooled nozzle guide vane wakes,

quantity and spacing of instrumentation was given significant consideration in the design of the TCI. The semi-infinite gauges were arrayed to provide both axial (8 locations) and circumferential (4 locations) spatial resolution of the endwall heat flux distribution. This arrangement is portrayed in Figure 4-5.

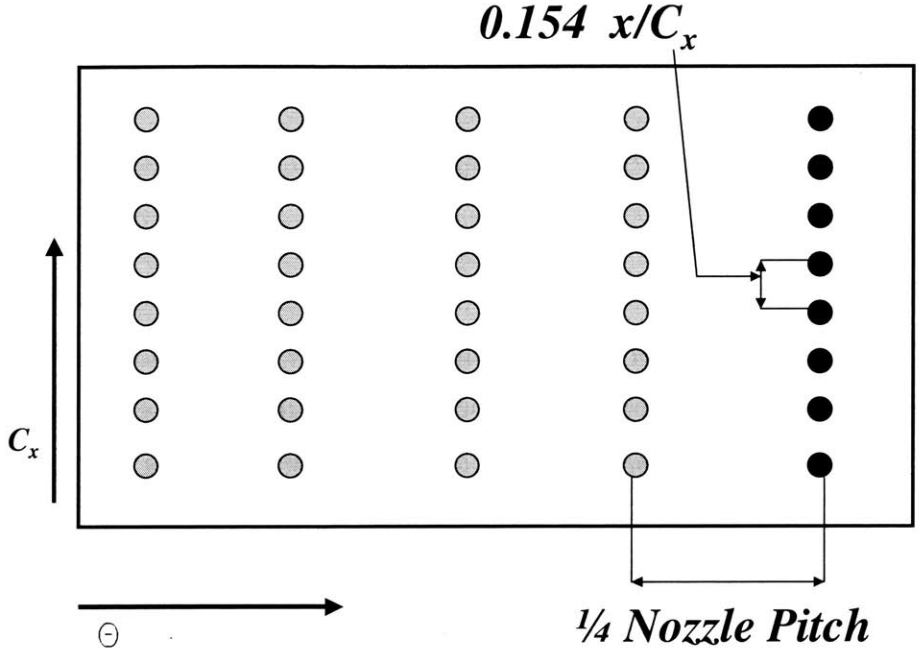

Figure 4-5: Instrumentation Arrangement and Spacing

The columns of gauges and pressure transducers were spaced evenly at one-quarter nozzle pitch (approximately 0.36 in.) in an attempt to resolve nozzle wakes in the heat transfer data. The column of Kulite pressure transducers was evenly spaced from the last row of heat flux gauges. Thus, one row of instruments included four heat flux gauges and one pressure transducer. On the connector side (side opposite the gauge and transducer sensor), two RTDs were onto the surface at opposite ends of the TCI. Figure 4-6, a view of the rotor looking downstream, shows the position of the instruments with respect to the blades.

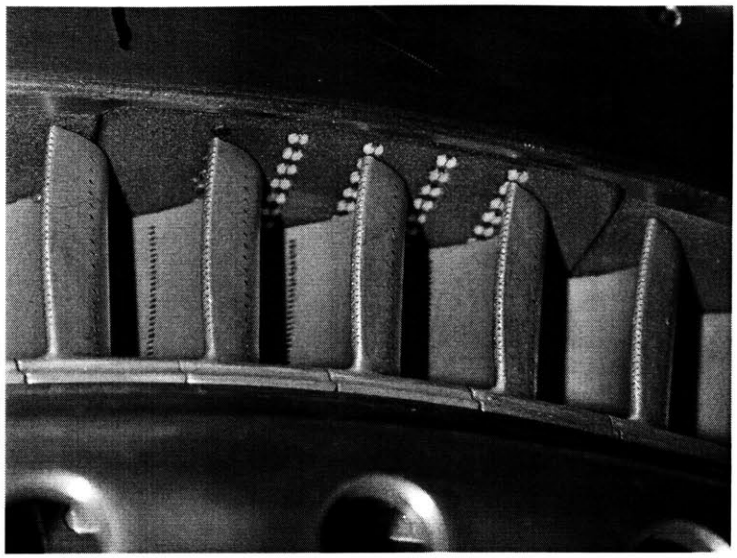

Fig. 4-6: Inserted TCI Looking Downstream from Rotor

4.4 Assembly

Heat flux gauges and Kulite pressure transducers were inserted into the TCI so that the sensor side of each gauge was flush with the curved surface of the TCI. The alignment process required care for two reasons: 1) the gauge surface must align with the concave surface of the TCI with minimal flow disturbance and 2) the abradable surface of the TCI was fragile and susceptible to wear. To assist in the sensor side alignment, a convex aluminum tool was machined to exactly match the concave surface of the TCI. Gauges were inserted and bonded using epoxy. To ensure that each gauge was fully seated and oriented correctly, the gauges were adjusted after the epoxy began to firm.

The grooves in the MACOR base of the gauges allowed the wire leads to feed through to the connector side of the TCI. Wires were connected to solder tabs. The tabs were bonded onto the aluminum surface of the connector side TCI. Five tabs were used for four gauges (one tab was common). Wires from the solder tabs were run along the outside of the TCI to a circuit board. The wiring configuration for each heat flux gauge is shown in Fig. 4-7 (note: this photograph shows the TCI prior to the installation of the pressure transducers). With the circuit board mounted on the TCI to facilitate wiring assembly, each heat flux gauge was connected to its corresponding circuit board pin.

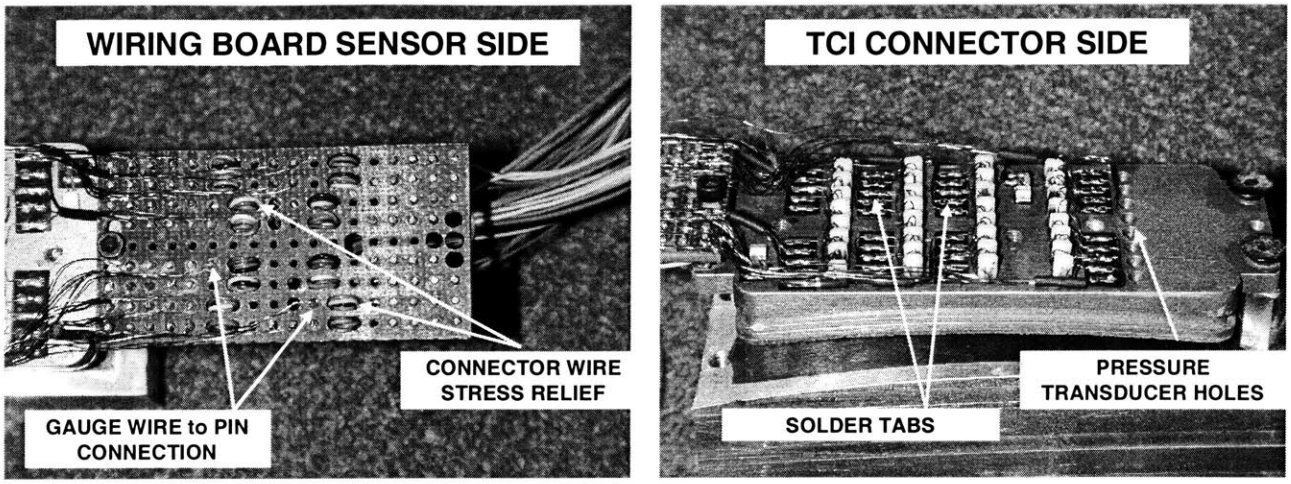

Fig. 4-7: TCI Connector Side wiring

The wiring of pressure transducers presented another challenge. The Kulites were manufactured with four wires in a wheatstone bridge configuration. Thus, the wiring task for these transducers was nearly as large as the heat flux gauges. Once wired, small back pressure tubes were attached to the Kulites to provide a vacuum reference for the purpose of calibration. A side view of the final wiring board is presented in Figure 4-8 below.

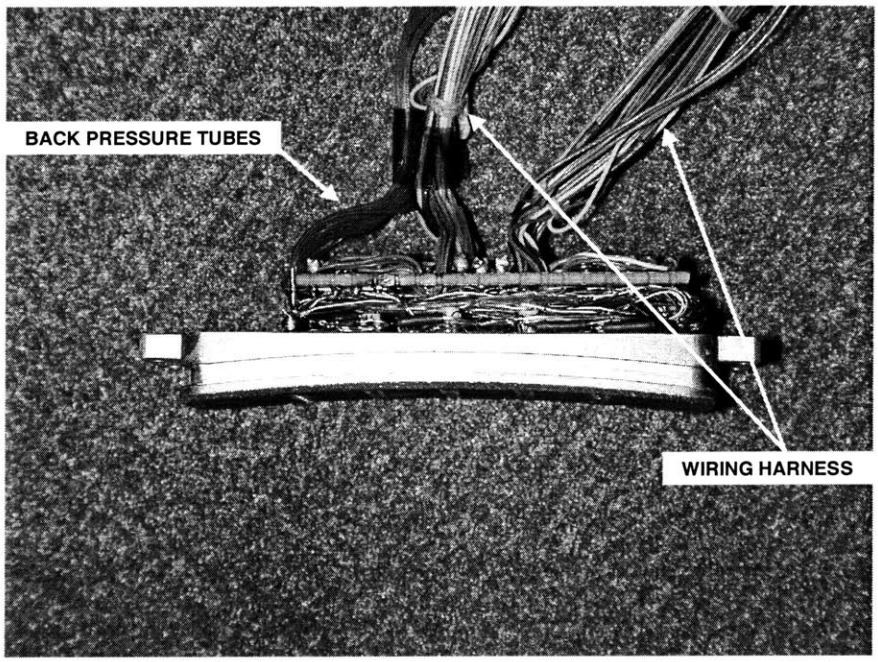

Fig. 4-8: Side View of Completed TCI

Each instrument on the tip casing was connected to the Blowdown Turbine DAQ system. Pressure transducers, heat flux gauges and RTDs were all connected to the high frequency ADTEK card systems. From the circuit board, the wiring harness comprised two Nanonics 44-pin connectors[1]. All 88 wires were laced together to provide ample rigidity and support to the wiring harness. The wiring harness was brought outside of the test section and contained in a tunnel feed through housing, as shown in Figure 4-9.

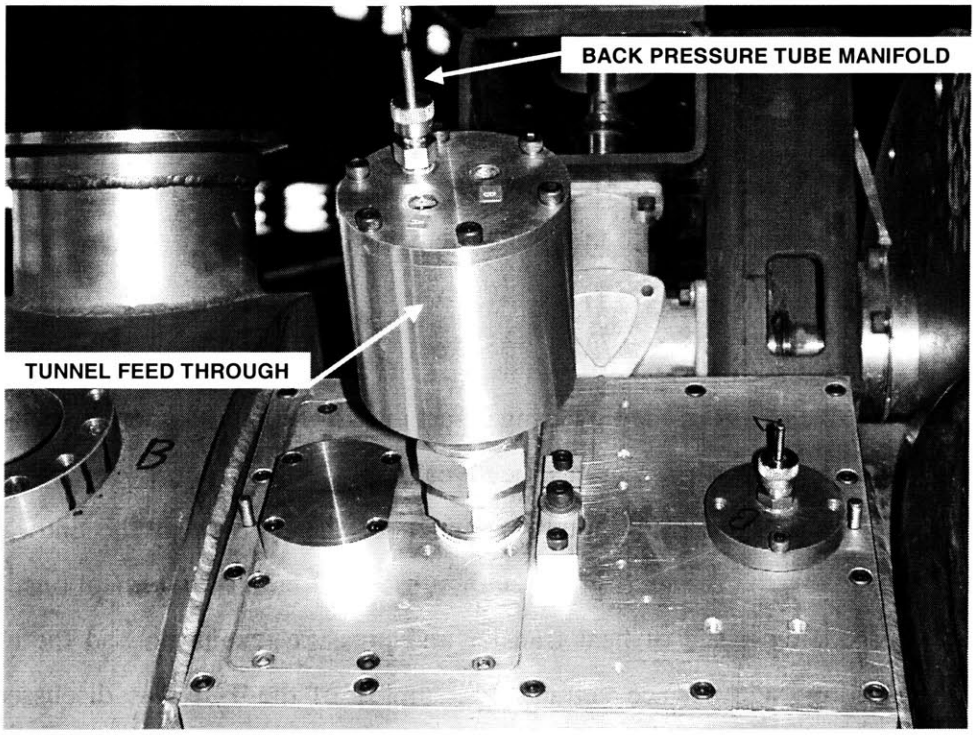

Fig 4-9: Tunnel Feed Through

4.5 Calibration

During testing, the heat flux gauge measured a surface temperature on the tip casing, which was reduced to determine heat flux. To compute an accurate heat flux, the thin film thermometers were calibrated as accurately as possible. The calibration technique used was to submerge the gauges and RTDs in a heated oil bath and record gauge analog output signal (a voltage) and the analog output signal from a highly accurate reference thermometer. The TCI,

[1] The Nanonics connectors are manufactured hermetic

with gauges and RTDs installed and fully wired, was submerged in the bath along with NIST traceable reference thermometer. A stirring mechanism was used to maintain an approximately constant temperature throughout the bath. The TCI wiring harness was connected through the wheatstone bridge amplifiers and into the DAQ for data collection. To begin the calibration, the heating unit was powered and the oil temperature brought up over 100^0 C. As the oil temperature cooled to 100^0 C, the DAQ system was started. Data was recorded every 5 seconds as the system cooled down to 40^0 C. Voltage signals for each heat flux gauge and RTD were matched to temperatures of the reference thermometer to determine both a scale ($^0C/_V$) and a zero ($X\ Volts = Y\ ^0$C). Three calibrations were performed prior to testing. The thermal properties of the MACOR gauge substrate were not calibrated, however published data has been shown by Kirk [17] to be very accurate in calculating heat flux.

4.6 Summary

A comprehensive report of the tip casing insert instrumentation holder has been presented in this chapter. Beginning with research objectives, TCI design criteria were identified with instrumentation in mind in order to capture as much of the physics of the endwall flow as possible without saddling the research group with substantial facility modifications. Emphasis was given to the academic issue of heat transfer and pressure resolution and the engineering issue of the TCI's flow side surface coating. Assembly of the TCI was discussed, and the chapter concluded with calibration procedures.

Chapter 5

Experimental Testing: Turbine Operating Point

5.1 Introduction

The purpose of this chapter is to present the experimentally measured turbine performance results for selected test conditions in order to fully characterize the operating point of the film-cooled turbine stage. This chapter also discusses the development of the turbine test matrix and defines the time window of useful data. This chapter forms the fundamental basis for comparison of the measured heat transfer data in Chapter 6.

5.2 Development of Test Conditions

The goal of the tests was to experimentally measure the time-resolved and time-averaged heat loads to the tip casing of the turbine over a range of turbine stage operating points at two rotor tip-gap-to-span ratios. To minimize the number of tests required, the development of an effective and efficient test conditions matrix was paramount.

A test matrix was developed to capture these trends in as few experimental tests as possible. Design point conditions for each tip gap ratio were used as a starting point. The design point was tested twice, serving as the first and last tests of each tip gap test series, to assess both flow condition and instrumentation repeatability. Four additional tests at each tip gap were conducted: low Nc, low PR, high PR, and high Nc. These tests represent the four cardinal directions on a Pressure Ratio Corrected Speed turbine operating map and were chosen to

elucidate the changes in heat transfer for one changing operating condition. The 3.0% tip gap test matrix is shown below, including the total percentage of coolant flow to the vane and blade.

Table 5.1: 3.0% Tip Gap Test Matrix

Test	Gas	PR	Nc	Mcool, %
T203	CO2	Design	Design	10%
T204	CO2	Design	Low	10%
T205	CO2	Low	Design	10%
T206	CO2	High	Design	10%
T207	CO2	Design	High	10%
T208	CO2	Design	Design	10%

A similar test matrix was developed for the 1.5% gap, shown below in table 5.2.

Table 5.2: 1.5% Tip Gap Test Matrix

Test	Gas	PR	Nc	Mcool, %
T210	CO2	Design	Design	10%
T211	CO2	Design	Low	10%
T212	CO2	Low	Design	10%
T213	CO2	High	Design	10%
T214	CO2	Design	High	10%
T215	CO2	Design	Design	10%

The tip casing remained uncooled throughout this test series.

5.3 Turbine Operating Point Test Results

Measurements were conducted on the film-cooled stage under the conditions shown in Tables 5.1 and 5.2. This section outlines the procedure for obtaining the turbine operating raw data for use in the interpretation of the tip casing heat transfer results presented in Chapter 6. Example data for turbine power, inlet total temperature, inlet and outlet total pressures, stage

non-dimensional parameters and a summary of measured operating parameters are presented for the test series.

5.3.1 Measured Total Temperature and Pressure

Turbine inlet temperature was measured at three circumferential locations at midspan around the annulus. Inlet temperature was also measured at one circumferential location using a five-head radial total temperature rake. For the performance and heat transfer results presented in this document, the midspan measurements were used. The inlet total temperature was averaged using a simple arithmetic mean. The inlet circumferential temperatures are plotted in Figure 5-1 for the design point conditions test, T208.

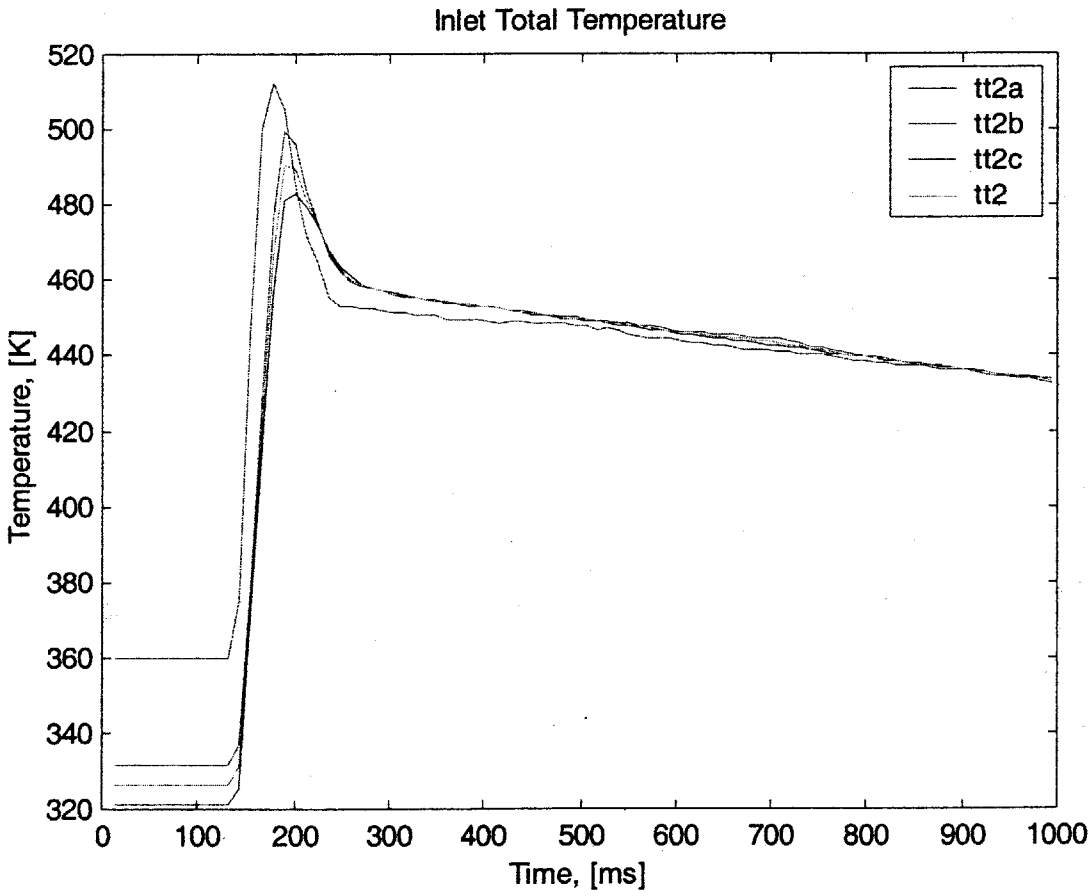

Figure 5-1: Inlet Circumferential Temperatures, Test T208

A steady decrease in total temperature after the initial transient (approximately 0.3 seconds) is the result of the expansion of the test gas from the supply tank and follows the isentropic model. The initial spike in the temperature figures is due to compressional heating.

The inlet total pressure is measured at three circumferential positions upstream of the test section, and is presented in Figure 5-2. Outlet total pressure is measured using an eight-head radial pressure rake that translates around the annulus to detect any non-axisymmetric features of the flow. The outlet total pressure is plotted in Figure 5-3; the oscillations in the figure are the result of NGV wake passing.

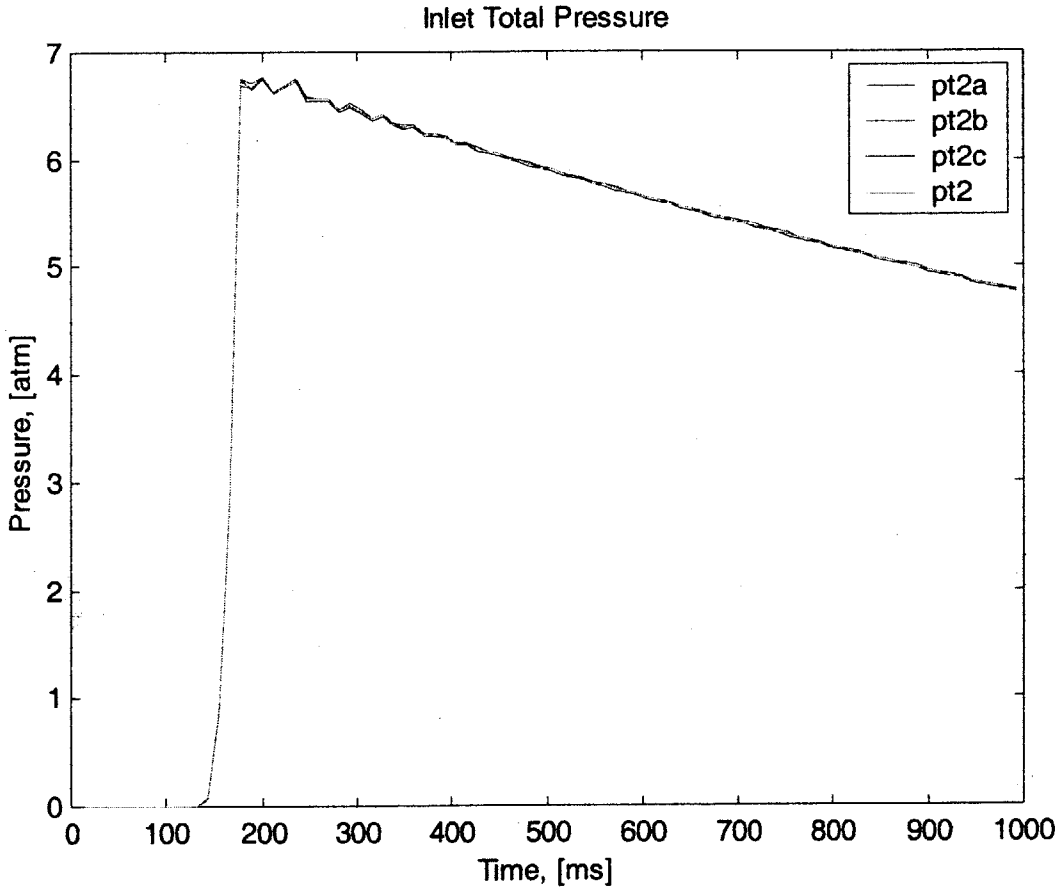

Figure 5-2: Inlet Total Pressure, Test T208

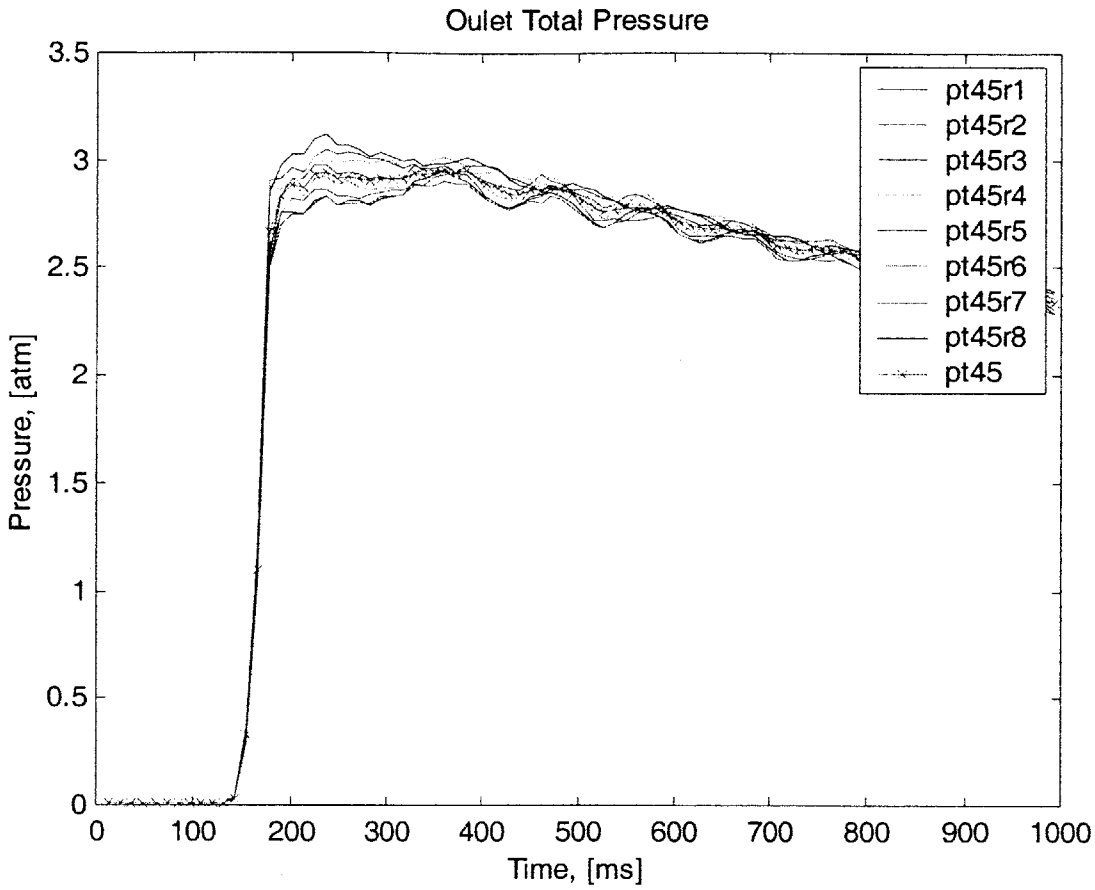

Figure 5-3: Outlet Total Pressure, Test T208

5.3.2 Flow Similarity Test Interval

The turbine stage experiences an initial unsteady transient during the startup of the facility. Data taken during this period is not useful. The flow similarity test interval defines the time window at which the flow is appropriately scaled. A time history of entropy of the inlet flow and the turbine pressure rates are used to ascertain the interval. For these tests, the FSTI begins at approximately 300 ms and ends near 900 ms.

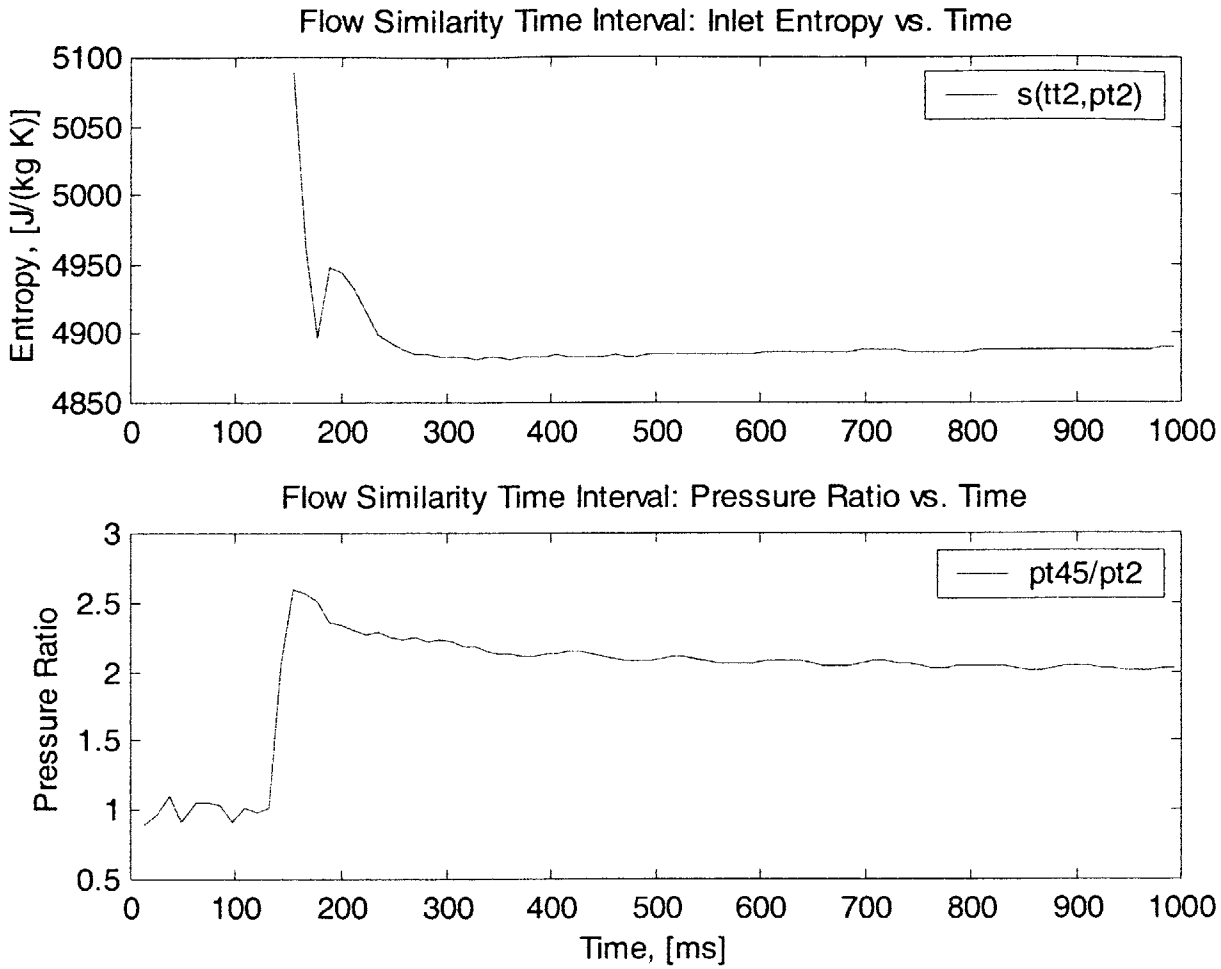

Figure 5-4: Entropy and Pressure Ratio, Test T208

Total pressure and temperature were fit using a 4th order polynomial fit over the flow similarity test interval. The data regression scheme smooths outlet pressure measurements to account for the NGV wakes, observed in the measured data presented above in Figure 5-3, and renders data more convenient for calculations. The 4th order fits of inlet and outlet total pressure and pressure ratio are presented below in Figures 5-5 to 5-7, over the flow similarity test interval.

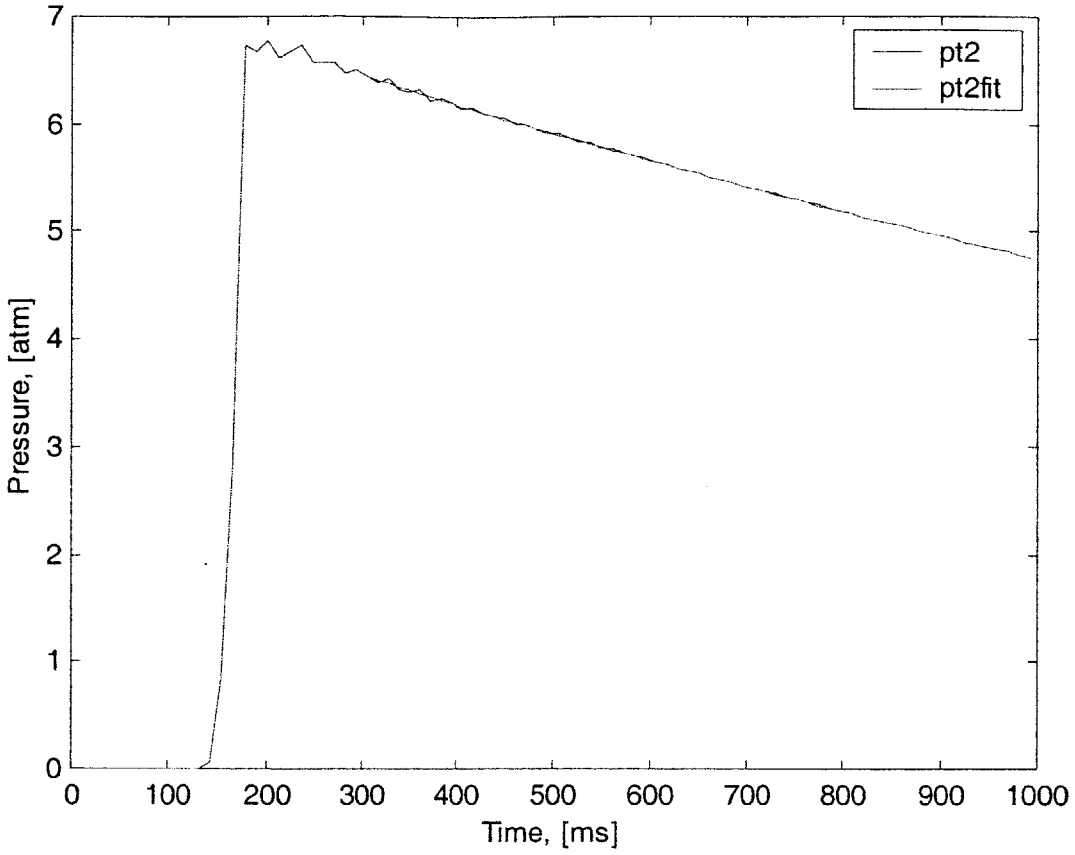

Figure 5-5: Average Inlet Total Pressure over FSTI, Test T208

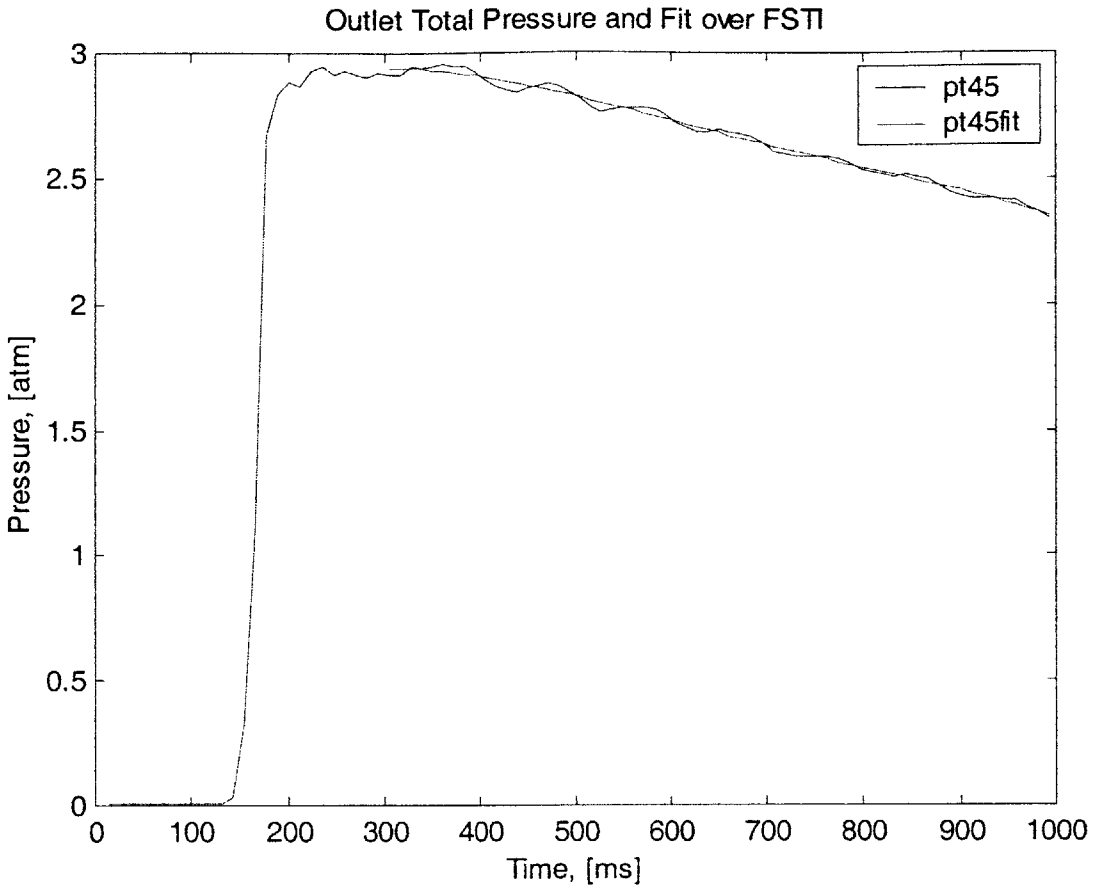

Figure 5-6: Outlet Total Pressure over FSTI, Test T208

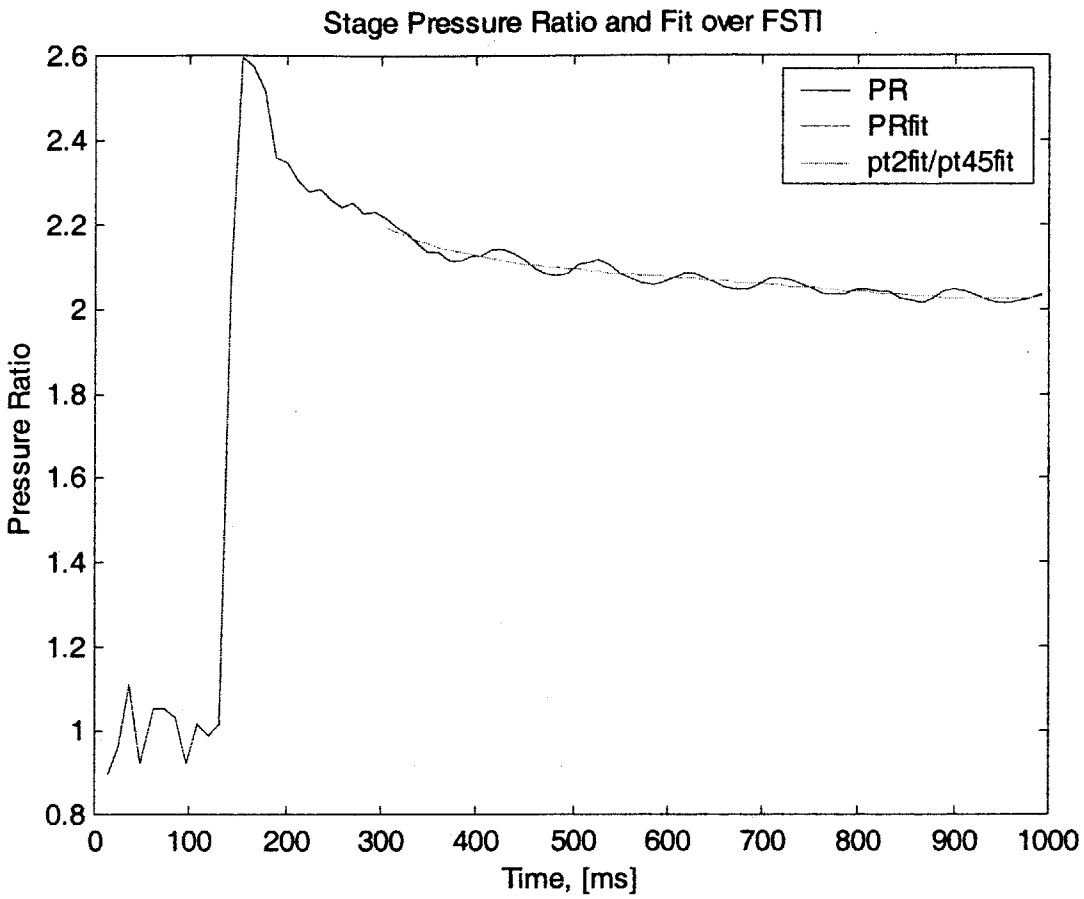

Figure 5-7: Stage Pressure Ratio, Test T208

5.3.3 Turbine Shaft Speed and Power

Figures 5-8 and 5-9 display the mechanical speed, shaft acceleration, turbine torque and power over the flow similarity test interval.

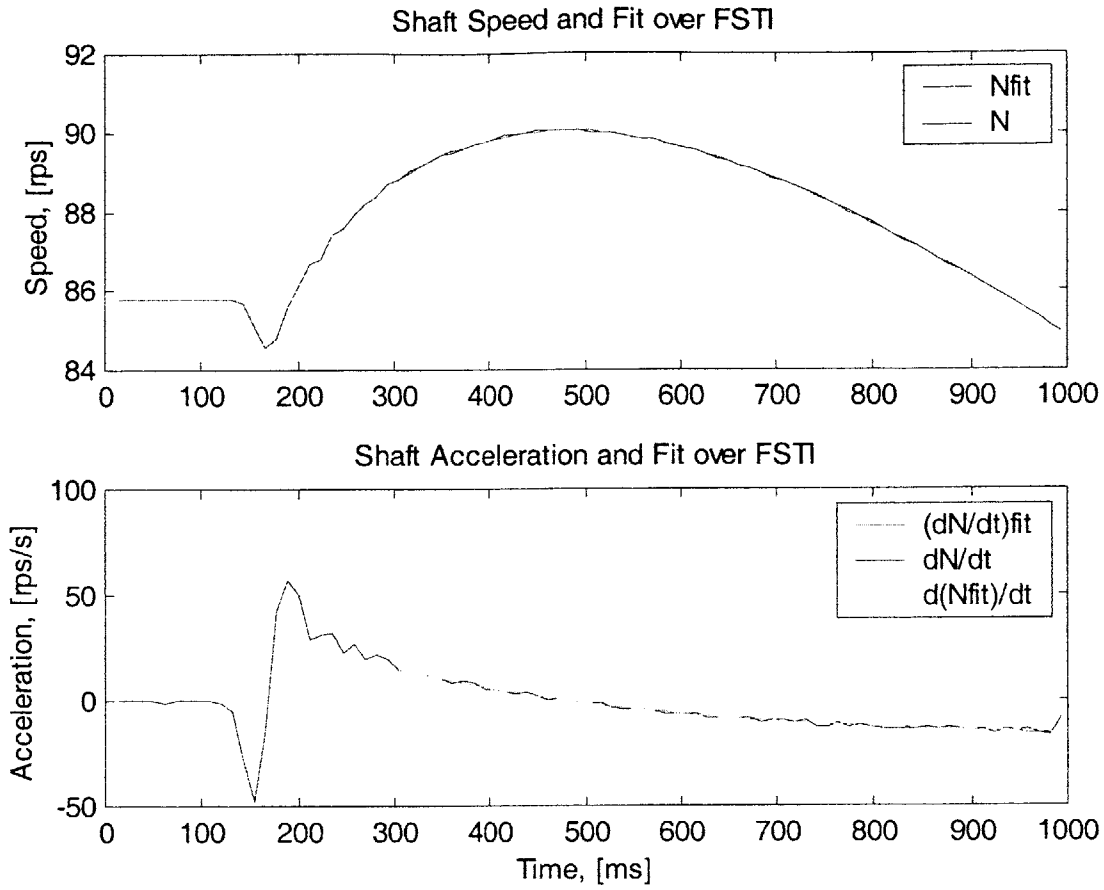

Figure 5-8: Shaft Speed and Acceleration, Test T208

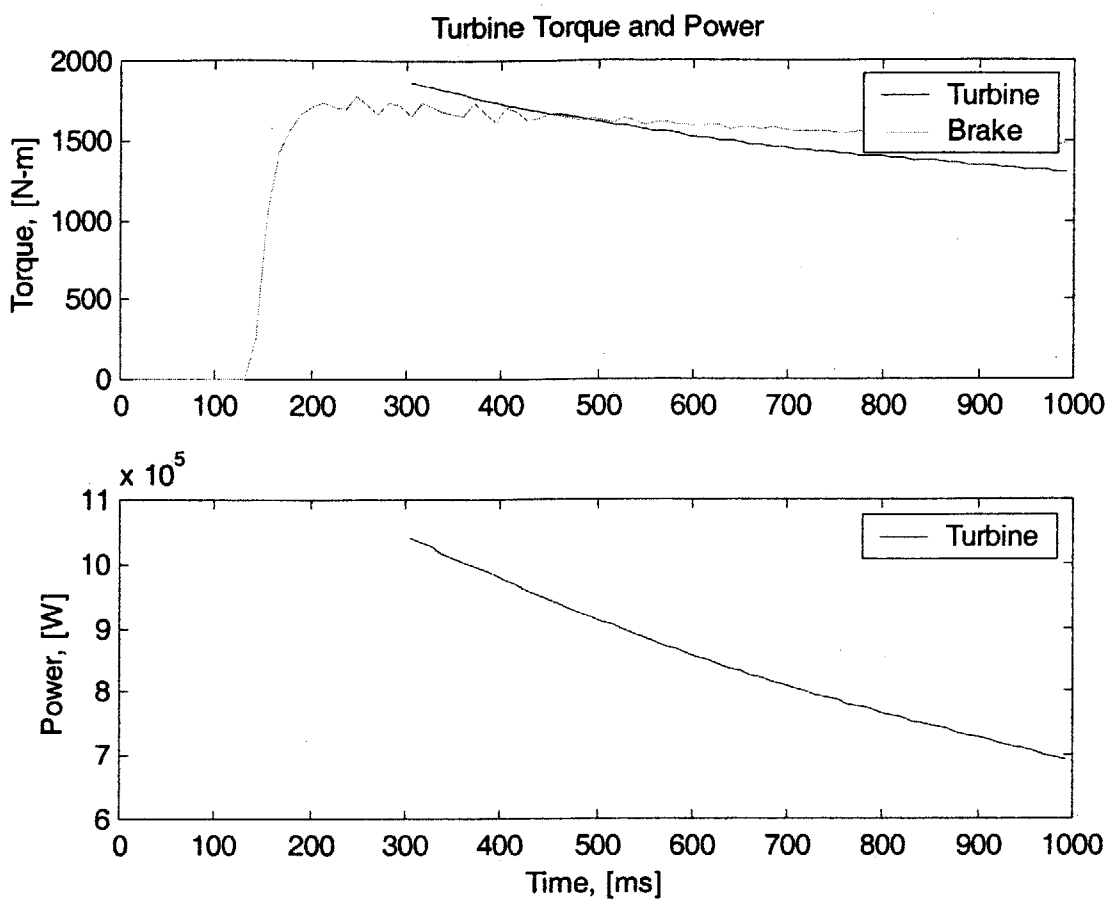

Figure 5-9: Turbine Torque and Power, Test T208

5.3.4 Corrected Speed

The turbine stage non-dimensional parameters of corrected speed, pressure ratio, Reynolds number, and ratio of specific heat (γ) must be matched to the actual engine in order to appropriately scale results. The pressure ratio and corrected speed are of primary importance for these runs (R_e and γ are kept the same for the series), since these two parameters define the turbine's operating point. Corrected speed is defined as:

$$N_c = \frac{\Omega L_{ref}}{\sqrt{\gamma R T_{ta}}} \tag{5.1}$$

Figure 5-10 illustrates the time history of corrected speed and its 4th order fit over the FSTI.

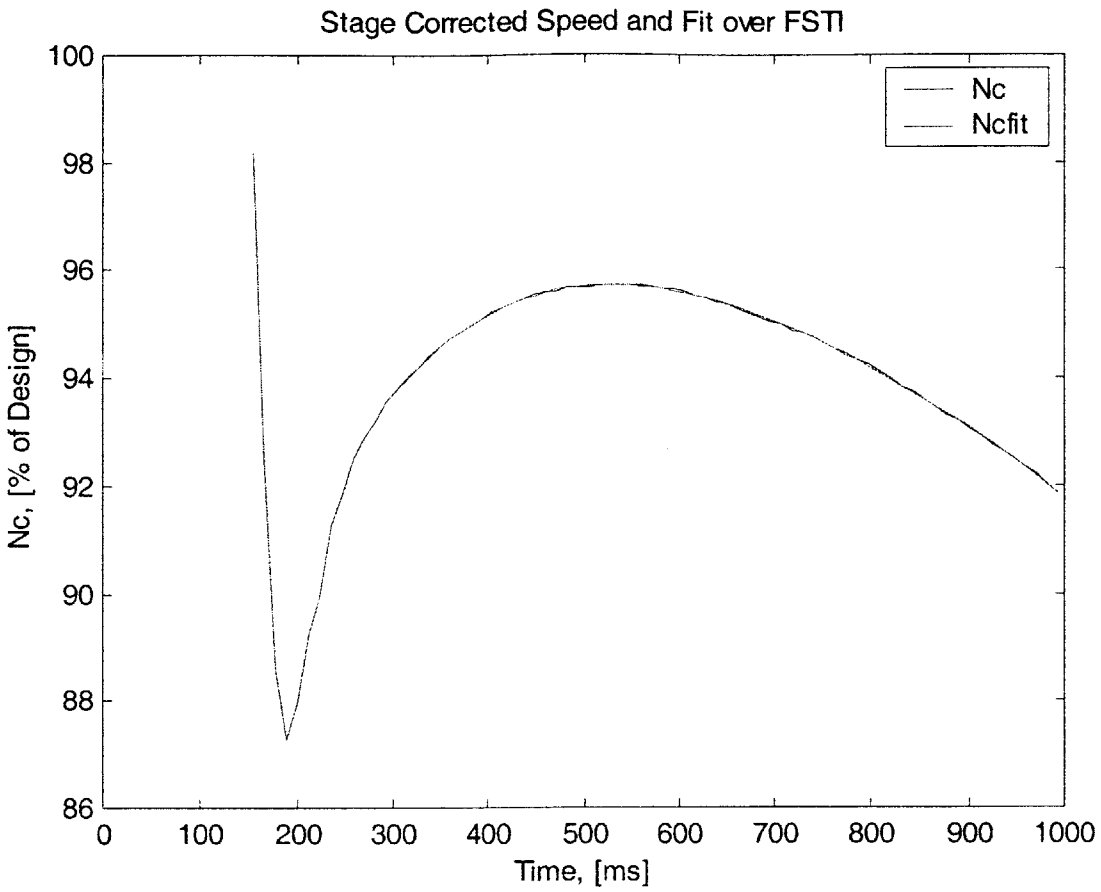

Figure 5-10: Corrected Speed, Test T208

5.3.5. Stage Operating Point

The turbine stage operating point is presented below over the flow similarity test interval. Markers for the start and stop time of the FSTI, as well as indicators for every 5 complete rotor revolutions, are indicated on Figure 5-11 for test T208. The operating maps, with FSTI start and stop indicated, are presented in Figure 5-12 for all tests conducted. These figures form the basis for determining suitable windows of comparison for heat transfer results. Operating point stability as a function of rotor revolution will be addressed in the context of time averaging in Chapter 6.

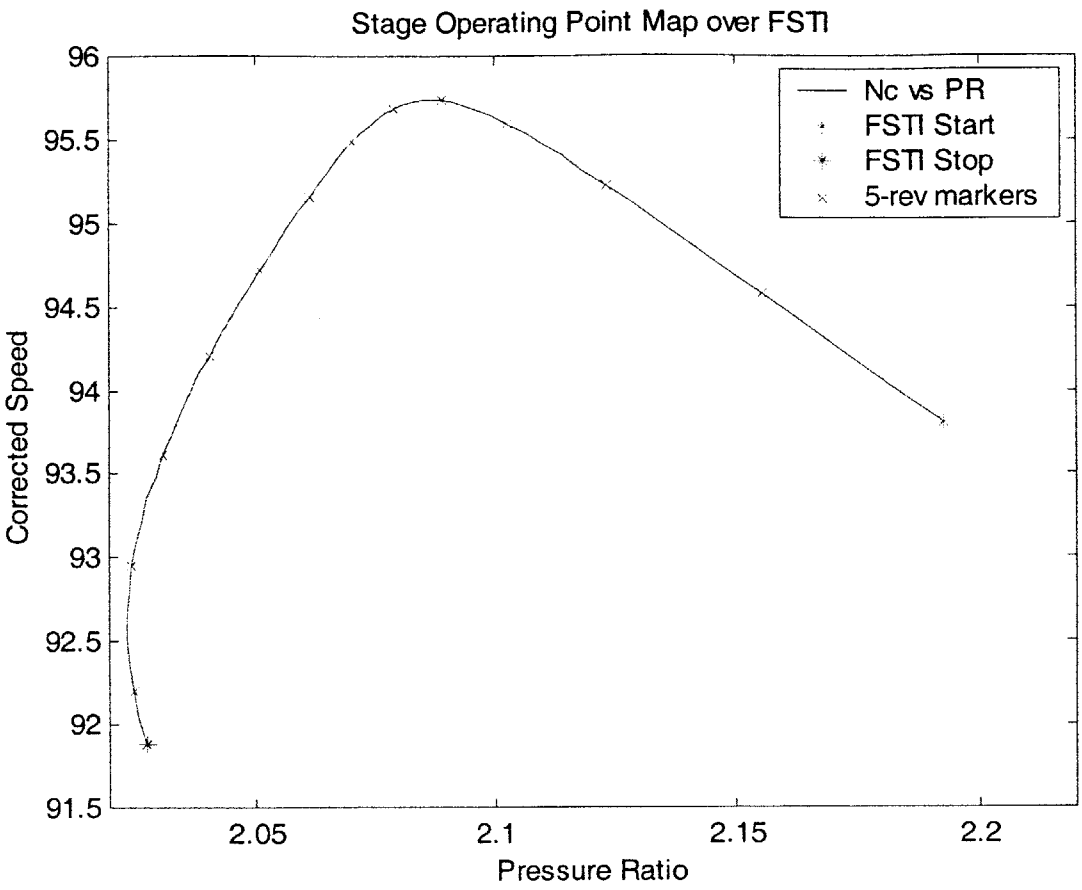

Figure 5-11: Stage Operating Point Map, Test T208

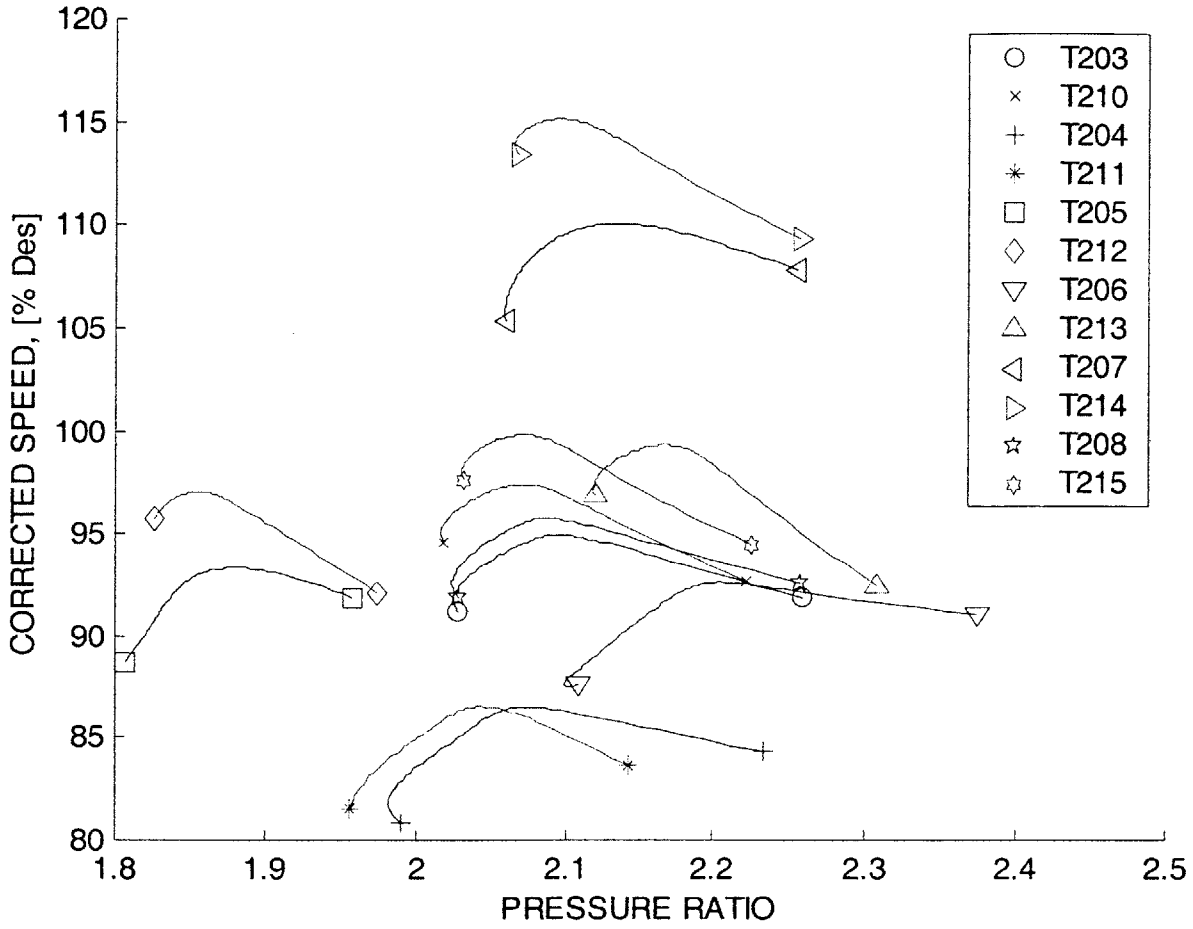

Figure 5-12: Test Series Operating Maps

5.4 Summary

The data reduced from turbine tests and the relevant parameters have been presented. A test matrix was developed to identify trends in heat transfer and has been discussed in this chapter. Previous work—including experimental work at the MIT BDT facility and elsewhere and computational work—were considered in the design of the test matrix. The experimental turbine stage operating conditions have been presented and will form the basis of comparison for heat transfer results presented in the next chapter.

Chapter 6

Experimental Testing: Tip Casing Heat Transfer Results

6.1 Introduction

The flow field on the tip casing surface is a complex, unsteady, three-dimensional flow. It is heavily influenced by the passing of turbine blades in close proximity to it. Tip casing heat transfer was measured for a fully scaled film-cooled turbine stage under rigorous conditions to re-create the phenomena found in a full-sized engine. The results reported herein represent an initial experimental investigation of the time-averaged heat transfer to the tip casing conducted to elucidate trends and identify significant features of the flow that are pertinent to heat transfer. Heat transfer measurements were taken over a range of operating points (pressure ratio and corrected speed) for two different tip gap ratios. Heat transfer comparisons are made within each test and between operating conditions at the same tip gap. The chapter concludes with a comparison of tip gap measurements.

6.2 Approach

6.2.1 Time Averaging

For this research, several time scales are relevant. Surface temperature data was sampled at high speed (200 kHz) to resolve the pertinent physics of the flow, particularly blade passing phenomena. A stage steady state time scale is also relevant, as it represents an adequate time

over which to compute the DC levels of heat flux that are valuable in design and analysis. For the turbine, through flow times are roughly equivalent to the time required for several blade passings. Additionally, the time scale for the operating point of the turbine must be considered, since the operating point changes over the test time. A one-rotor-revolution technique was selected as the averaging scheme for the steady state time scale. Over the time period of a rotor revolution, the operating point remains nearly constant and can be considered quasi-static. Since 88 blade passings occur within this time, it also reasonably approximates steady state conditions. Thus, for comparison of heat flux results within a test, a rotor-revolution average provides a set of steady state operating points.

The operating points (Nc vs PR) of all experimental tests were observed to ascertain a suitable averaging window (Figure 5-12). Corrected speed was plotted against pressure ratio to find a period of stability in the operating point. This plot is shown again in Figure 6-1. The start and end point of each run are annotated. For all runs the time period that provided the most suitable window for averaging heat flux data was approximately 500 – 600 milliseconds (about 5 rotor revolutions). Results for heat flux are averaged over this time period.

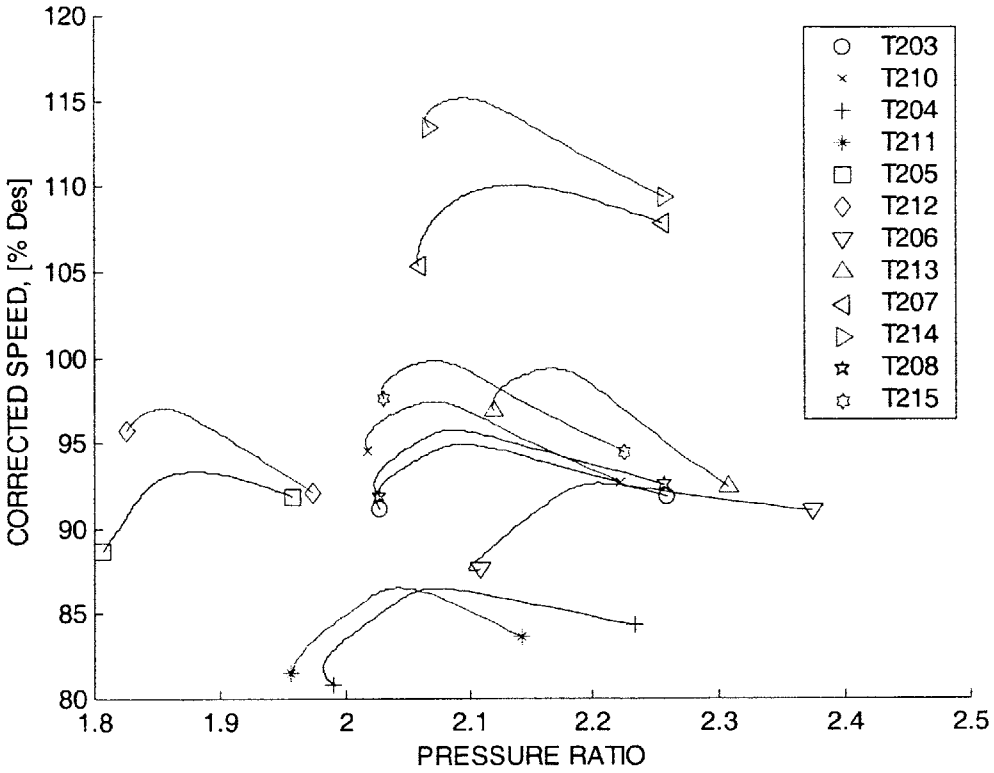

Figure 6-1: Test Operating Point Maps

6.2.2 Non-dimensionalized Heat Flux

To effectively compare data within a test and between different tests, the tip casing heat flux was non-dimensionalized based upon the inlet total temperature and the local static temperature. In the form of a Nusselt number, N_q , it is defined as:

$$N_q = \frac{\dot{q} C_x}{k(T_w)[T_{to} - T_w(x)]} \tag{6.1}$$

In the above equation, $\dot{q}$ and T_w are the heat flux and local wall static temperature averaged over one rotor revolution; $k(T_w)$ is the thermal conductivity of the test gas based upon wall static temperature; and C_x is the axial cord. In this form N_q represents the non-dimensionalized heat flux. It is important to note that it is based upon the global quantity of inlet total temperature, and thus allows heat loads to be scaled for comparison with the full-scale turbine.

6.2.3 Film Heat Transfer Coefficient

A second form of normalization is used to depict the changes in heat transfer coefficient and to provide insight into the characteristics of the endwall boundary layer. Again in the form of a Nusselt number, it is based upon the local total temperature and local wall static temperature. A linear profile was assumed to estimate the local total temperature. The total temperature drop across the rotor was computed using the measured stage pressure ratio and calculated efficiency. Identified as N_h, it is defined as:

$$N_h = \frac{\dot{q}C_x}{k(T_w)\left[T_{tl}(x) - T_w(x)\right]} \tag{6.2}$$

N_h accounts for the total temperature drop across the rotor due to rotor enthalpy extraction. Unlike N_q, N_h represents the inverse of a film's resistance to heat transfer—a heat transfer coefficient. Defining the film coefficient h,

$$h \equiv \frac{\dot{q}}{T_g - T_w} \tag{6.3}$$

N_h becomes:

$$N_h = \frac{hC_x}{k} \tag{6.4}$$

Written this way, N_h reveals itself as a normalized heat transfer coefficient. To further illustrate the implications of N_h, Figure 6-2 depicts an analogous situation. On the left, the figure shows conduction through a film of static fluid with a representative temperature profile. On the right, the film of fluid is now moving and heat convected to the wall, resulting in a different temperature profile. Since both heat transfer mechanisms prevail in the turbine, the ratio of convection to conduction is certainly relevant. In this way, N_h reveals characteristics of the endwall boundary layer.

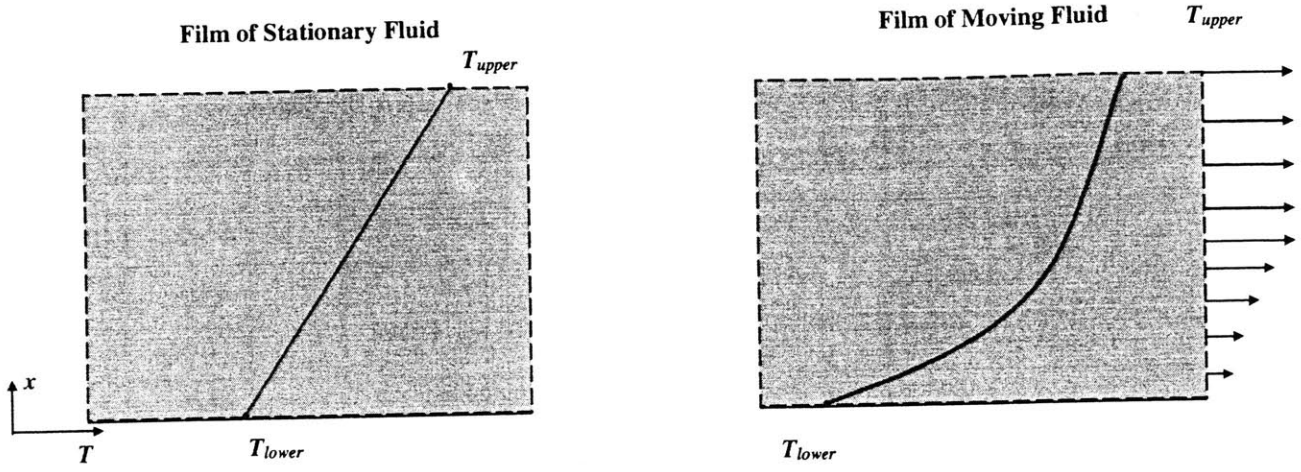

Figure 6-2 Graphical Analogy of N_h

6.3 3.0% Tip Gap Results

A summary of the casing average values for N_q and N_h for the different operating point tests, given below in Table 6.x, is provided up front for initial comparison of results for different operating conditions.

Table 6.1: Heat Flux Summary for 3.0% Tip Gap Tests

Test	PR	Nc	$\bar{N}_q$	$\bar{N}_h$
T203	2.09	94.8	1465	2424
T204	2.05	86.0	1439	2302
T205	1.86	93.0	1493	2258
T206	2.19	92.0	1428	2424
T207	2.11	109.8	1443	2481
T208	2.08	95.7	1435	2382

6.3.1 Heat Flux and Surface Temperature

Surface temperature histories on the tip casing insert were measured during each experimental test for the 3.0% gap. A representative surface temperature history for one gauge during test T203 is presented in Figure 6-3. Noteworthy is the significant temperature rise at approximately 0.2 seconds. Wall surface temperature shows a steady increase and then tails off toward the end of the run.

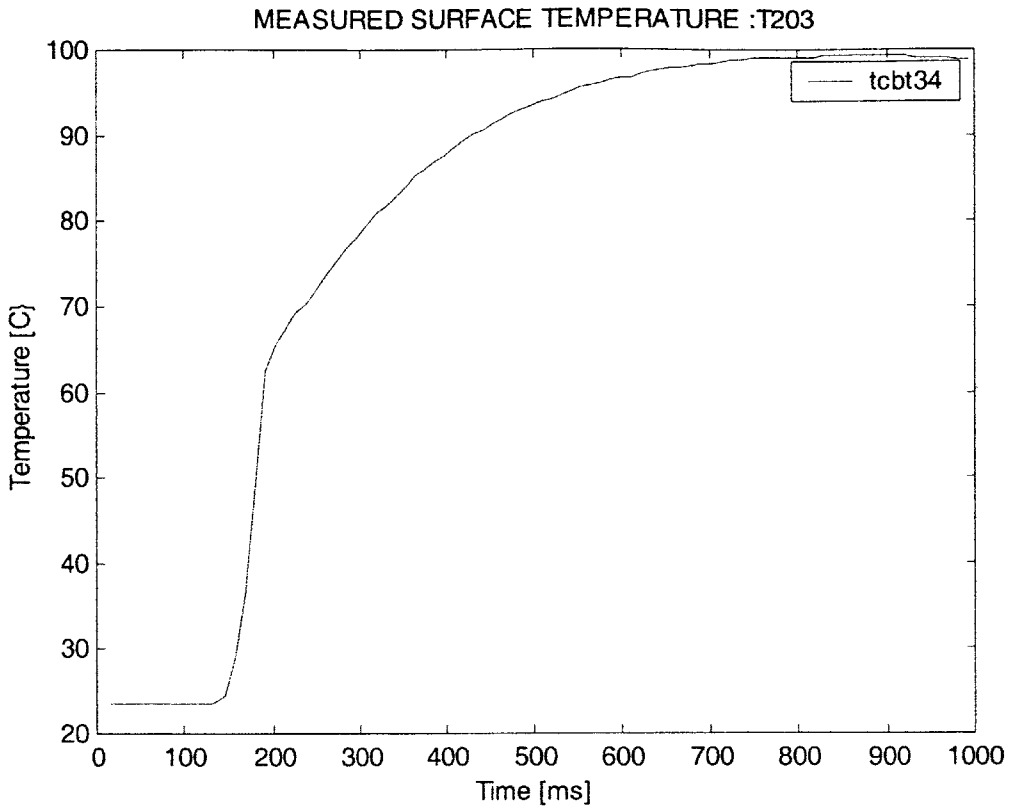

Figure 6-3: Measured Tip Casing Surface Temperature, Test T203

Heat flux was calculated, using the numerical technique discussed in reference [24], based upon rotor-revolution averaged surface temperature. This technique yielded an approximate heat flux time history, smoothing out extremity points from the true time-resolved data. The rotor revolution averaged heat flux for test T203 is illustrated in Figure 6-4.

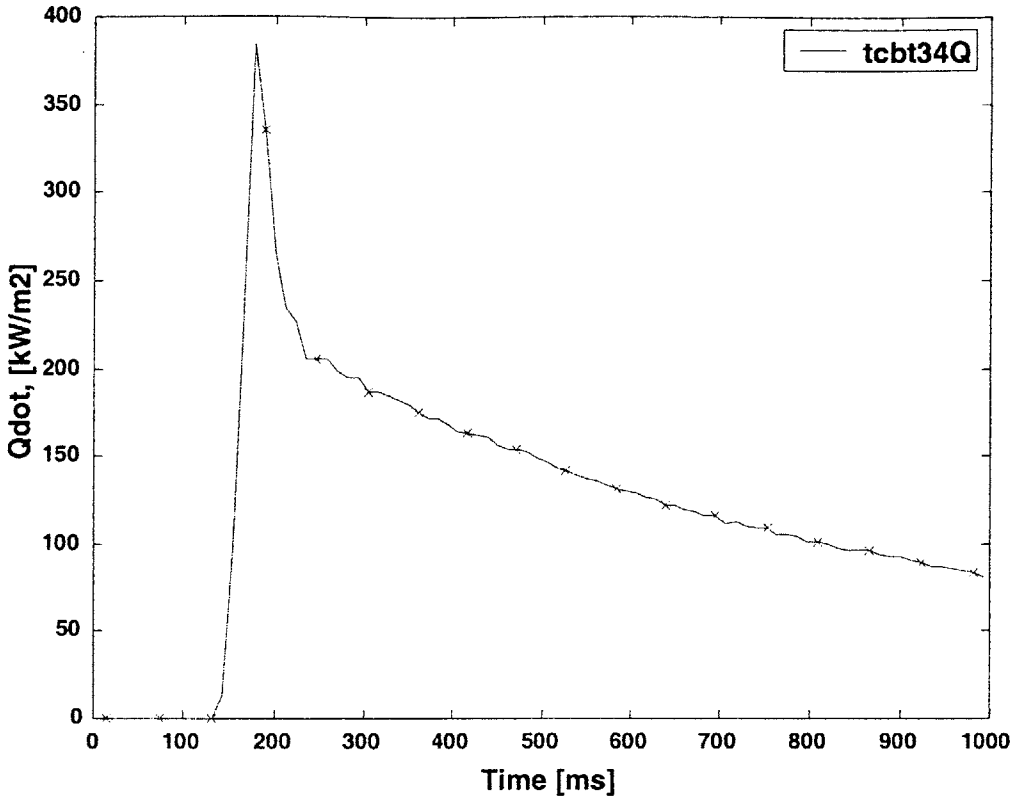

Figure 6-4: Rotor Revolution Averaged Heat Flux, Test T203

6.3.2 Non-dimensional Heat Flux: N_q

When non-dimensionalized, the time resolved heat flux can be used in comparing run conditions. Values for N_q were computed from dimensional heat flux and temperatures that were averaged over a rotor revolution, and then averaged over the period of 500 to 600 ms. Surface color contour plots of both design point tests are shown below in Figures 6-5. The x-axis represents the axial cord position, normalized by the blade cord, and the y-axis represents the circumferential position normalized by one vane pitch.

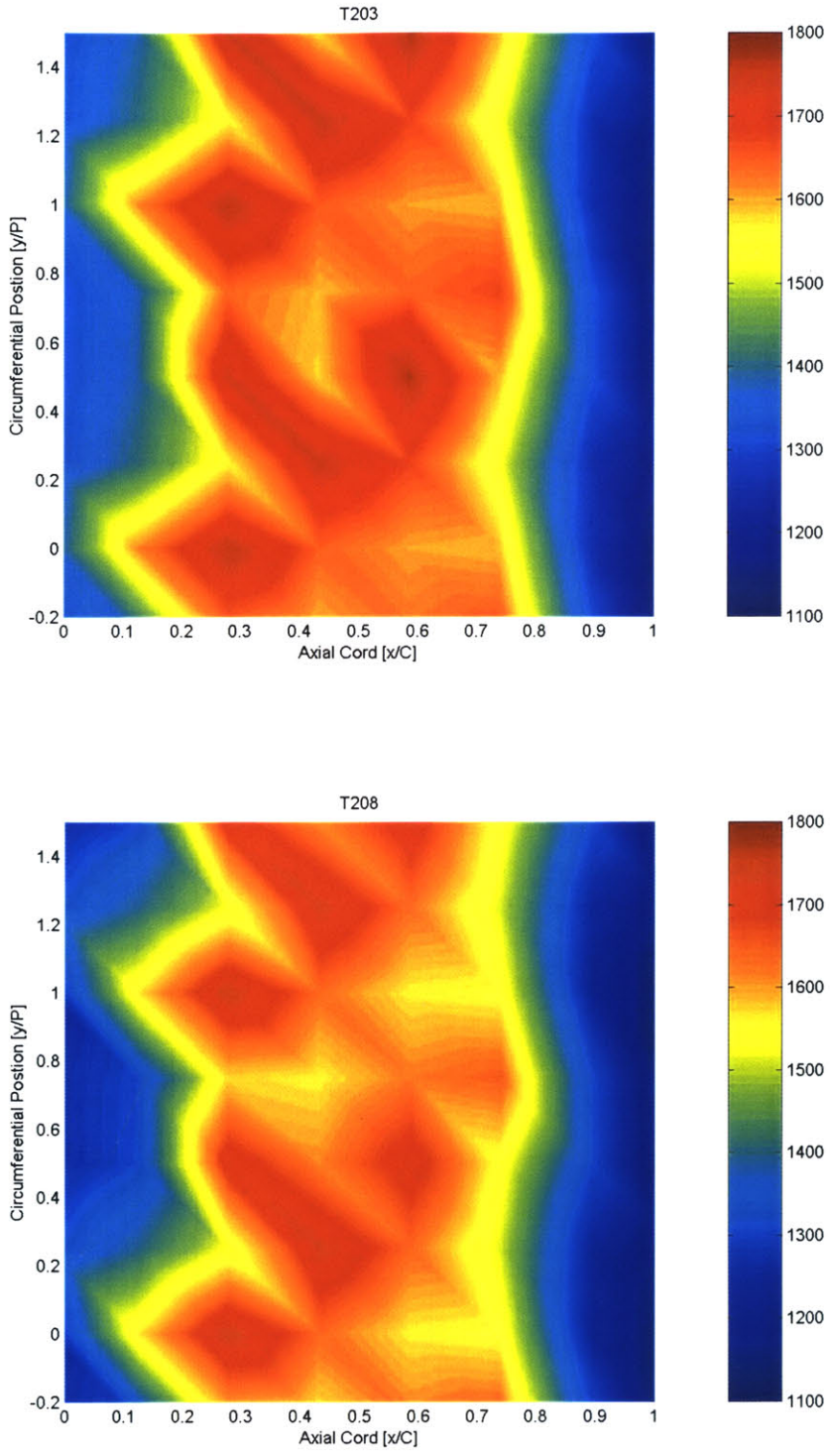

Figure 6-5: N_q for Design Point Tests (T203, T208)

The heat flux contours show good agreement, lending credence to the repeatability of measurements for this test series[1]. Heat flux contours appear in the approximate direction of the vane exit flow (stationary frame), implying an influence of nozzle wakes on heat transfer. Additionally, the drop in N_q along the cord is the result of the rotor extracting work from the fluid and thus reducing the gas total temperature. This trend is similar to other experimental data [9]. The axial variation is highlighted in Figure 6-6 below, which show time-averaged N_q plotted against normalized axial position for gauge locations at one-quarter normalized pitch. Note the convention of the legend— "Nq1x" –where 1 represents the circumferential locations (row number), while "x" identifies the axial position.

[1] It should be noted that run T203 was conducted at the beginning of the test series; T208 was the final test in the series

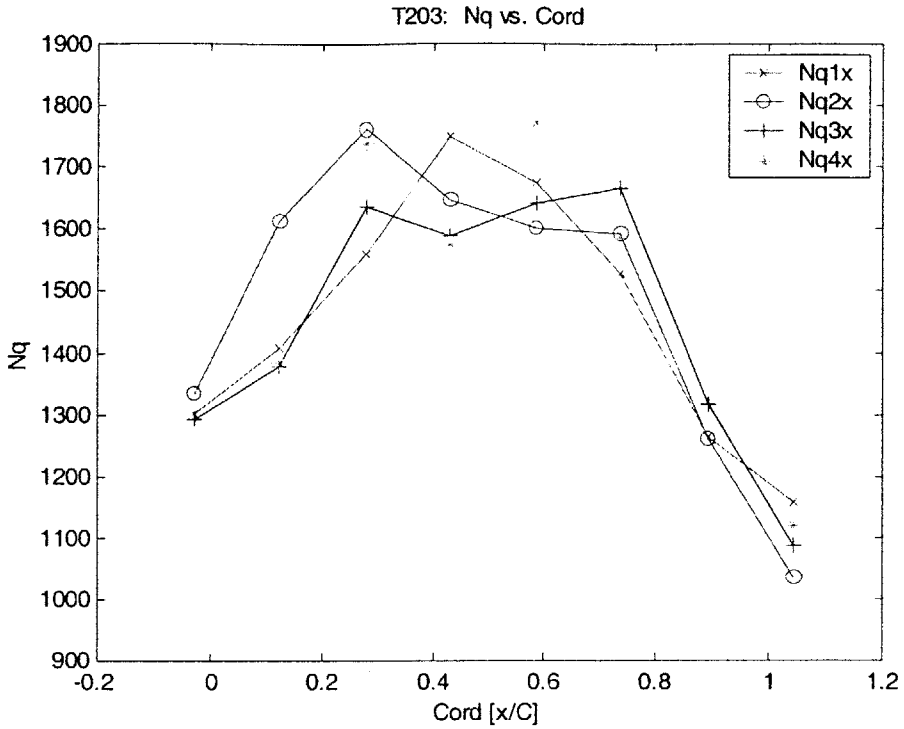

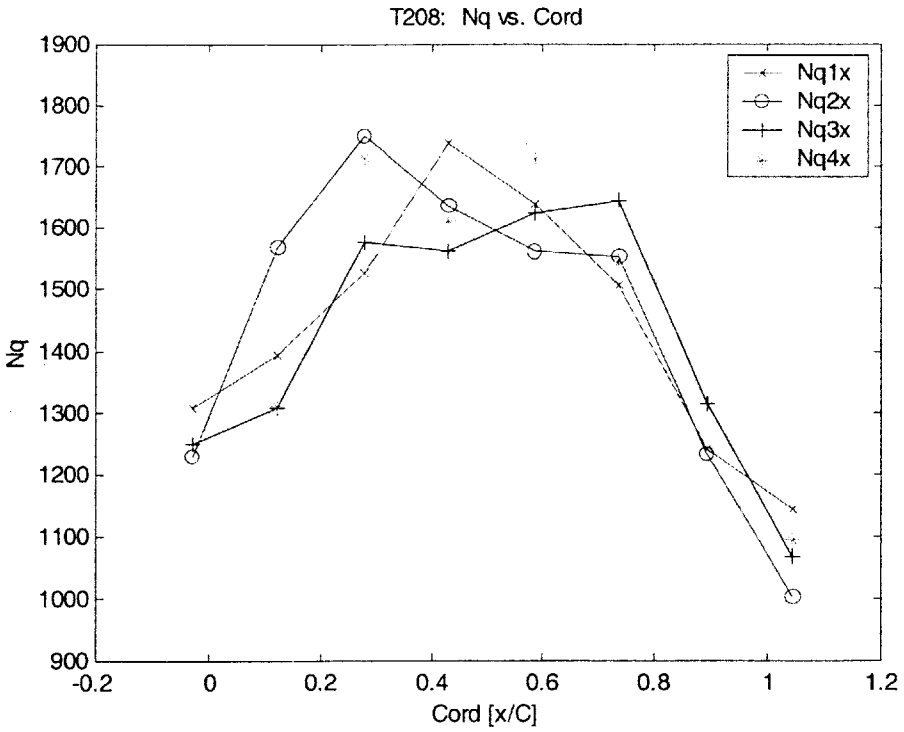

Figure 6-6: Design Point N_q vs. Cord (T203, T208)

6.3.2.1 Pressure Ratio Tests

Heat flux contours for pressure ratio tests are shown in Figure 6-7. Axial distribution of heat flux is presented in Figure 6-9. Low pressure ratio, design and high pressure ratio runs are presented.

In the non-dimensional form, heat flux shows a decreasing trend with increasing pressure ratio. For lower pressure ratios, there is less work and thus a lower total temperature drop across the stage. Thus, the total temperature—and therefore the "driving temperature" difference—remained higher. The higher driving temperature accounts for the higher endwall heat load in lower pressure ratio runs

6.3.2.2 Corrected Speed Tests

Corrected speed was varied over three tests, with set conditions of 90%, 100%, and 112%. Contours are displayed in Figure 6-8 and axial distribution is plotted in Figure 6-10. Corrected speed runs show only a slight increase in heat flux to the casing for higher speed runs. Rotor corrected speed directly influences the incidence angle of the flow entering the rotor from the vane row, which results in changing the rotor relative inlet flow angle. Additionally, higher corrected speed tests have shown a higher stage efficiency. Both of these effects, to some degree, may influence the heat load to the tip casing. The relative magnitude of the axial plots (Figure 6-10) shows some agreement with previous tip casing heat transfer data taken by Guenette in the MIT BDT [9].

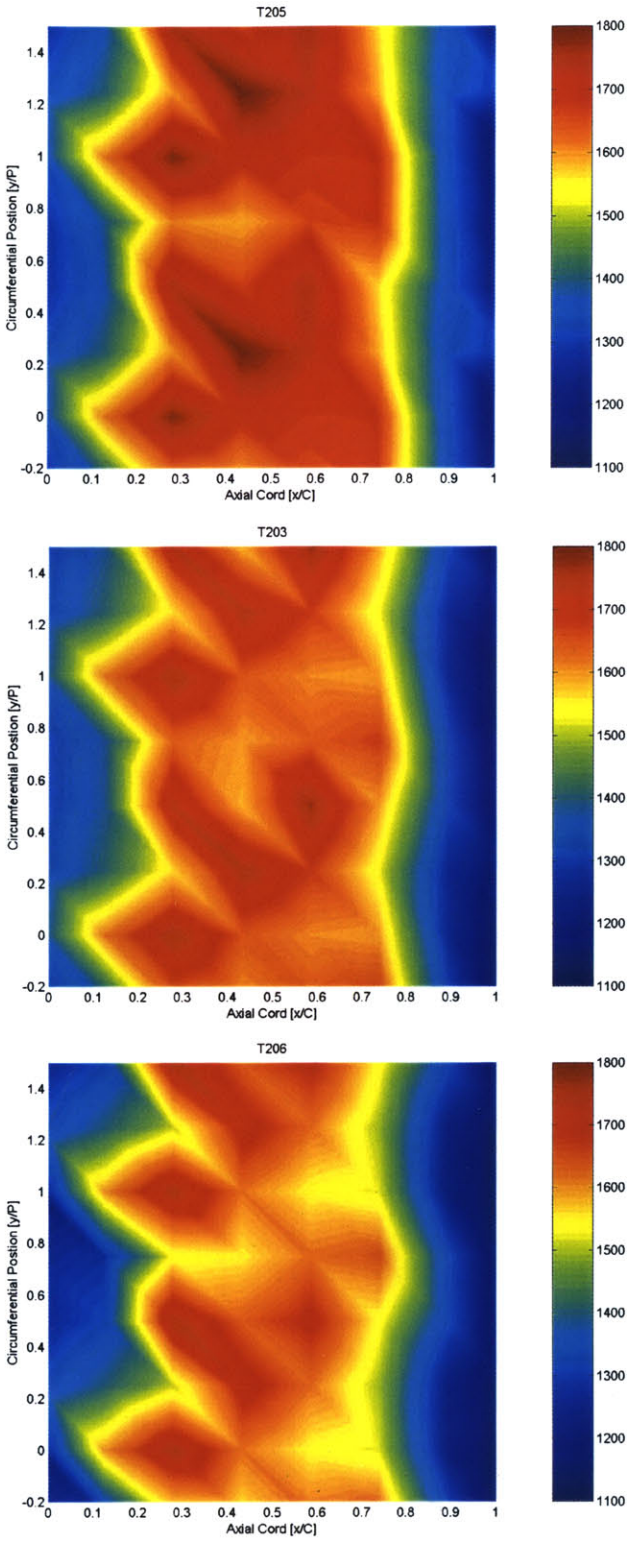

Figure 6-7: N_q for Pressure Ratio Runs (T205, T203, T206)

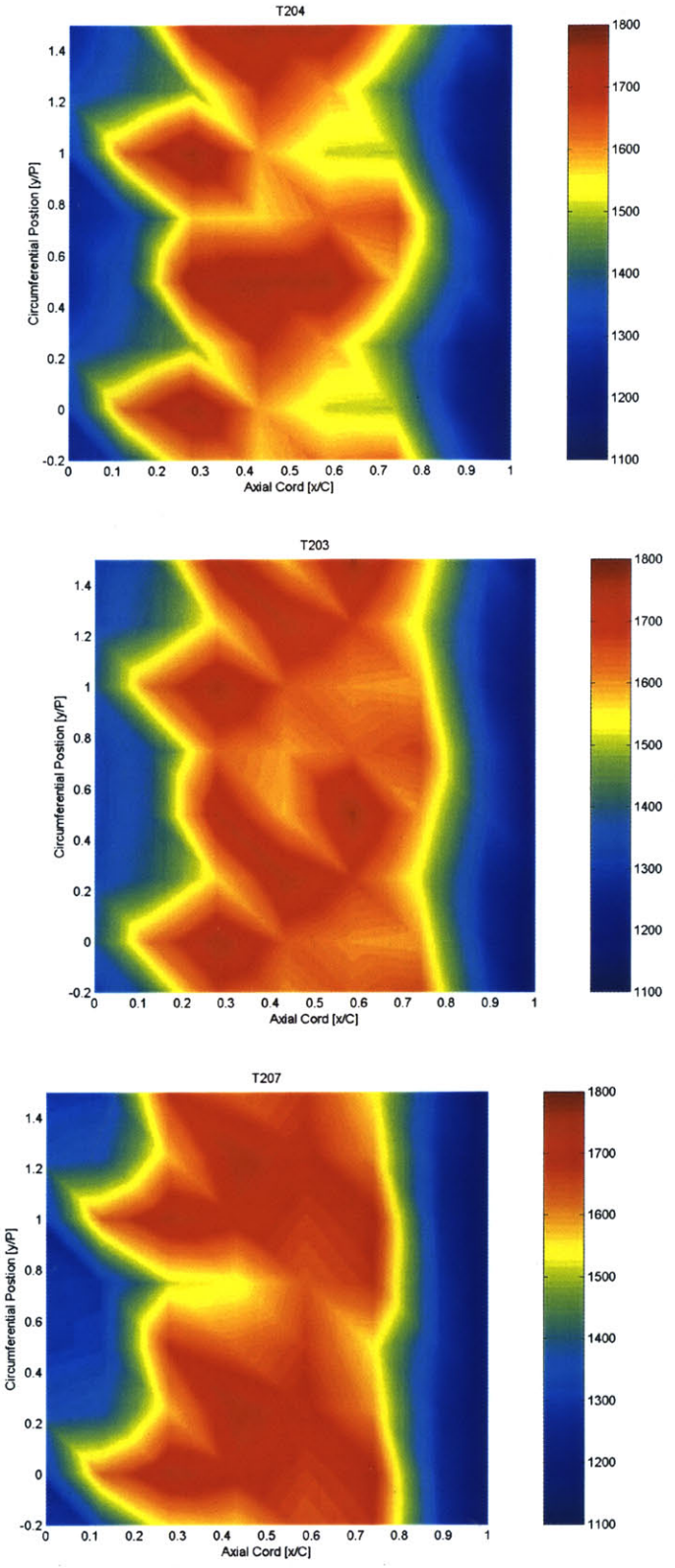

Figure 6-8: N_q for Corrected Speed Runs (T204, T203, T207)

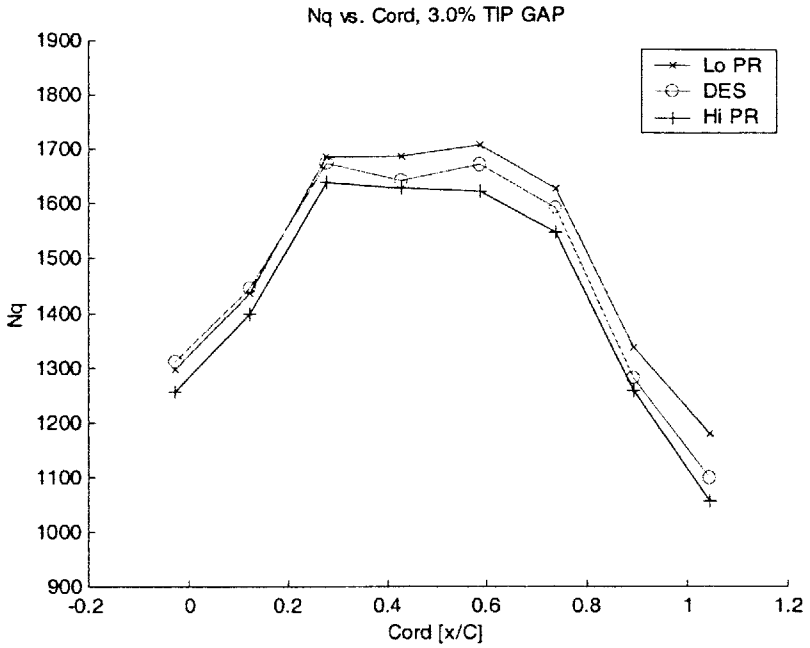

Figure 6-9: Axial Distribution of Nq for Pressure Ratio Tests

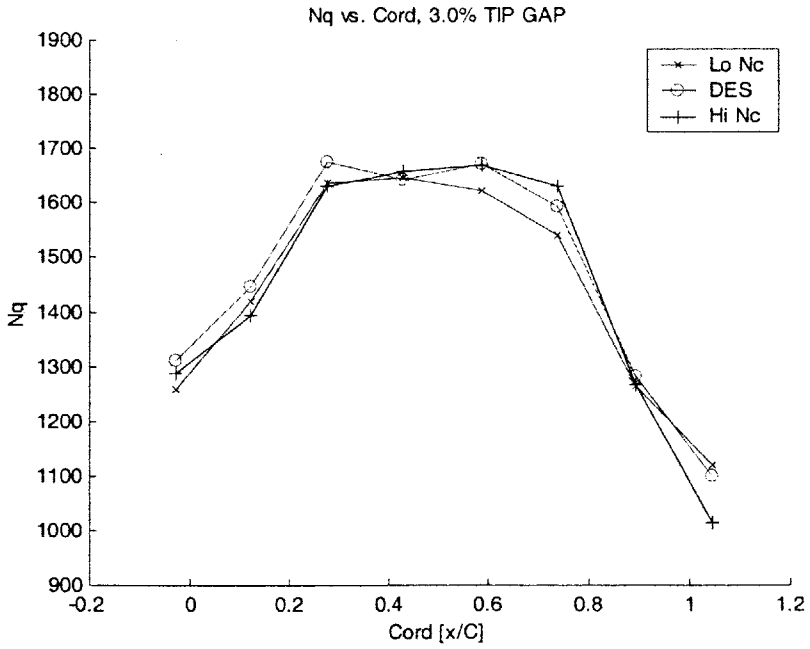

Figure 6-10: Axial Distribution of Nq for Corrected Speed Tests

6.3.3 Non-Dimensionalized Heat Transfer Coefficient

The normalized heat transfer coefficient based upon local total temperature, N_h, is presented here for all experimental tests at 3.0% gap. N_h accounts for the drop in total temperature across the stage, commensurate with equation (3.2), which is presented again for reference:

$$N_h = \frac{\dot{q}C_x}{k(T_w)[T_{tl}(x) - T_w(x)]}$$

The driving temperature, normalized by its value at the stage inlet, is shown below in Figure 6-11.

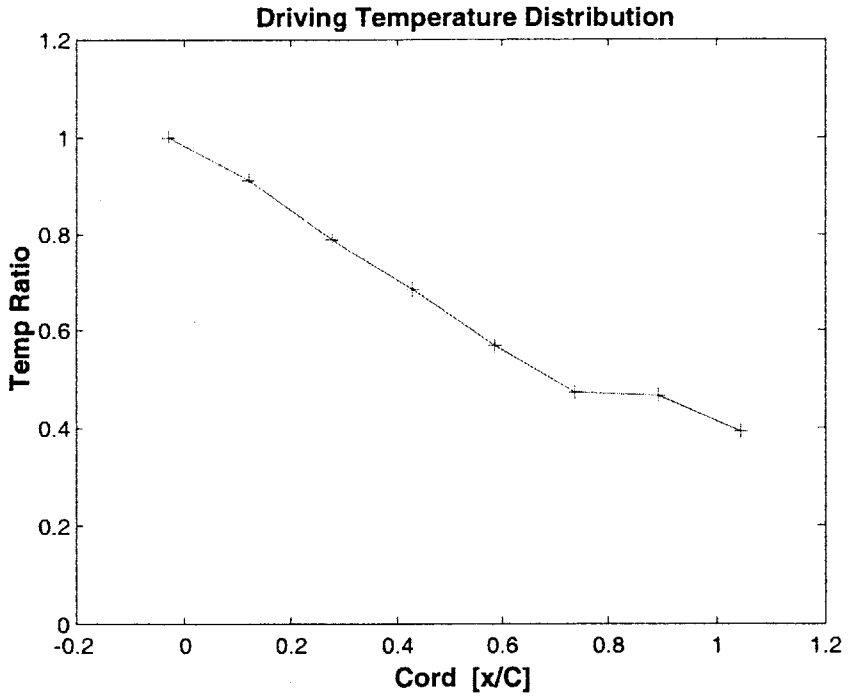

Figure 6-11: Driving Temperature Profile $\frac{[T_{tl}(x) - T_w(x)]}{[T_{to} - T_w(x)]}$

The significance of the driving temperature down the cord is evident; adjusting for this drop provides insight into the characteristics of the endwall boundary layer along the cord.

At the design point tests, N_h shows strong agreement between tests. Design point tests are illustrated below in Figure 6-12, again shown as color contour plots.

The larger variation in N_h, compared to N_q, is evident. N_h continues to increase along the cord after the point at which heat flux begins to drop off. The magnitude of the cordwise variations in N_h can also be observed from plots of time-averaged N_h vs. cord, shown in Figure 6-13 for a design point test. Axial values of N_h and N_q are displayed together in Figure 6-14. All test runs show similar trends in the broad sense. From Figure 6-14, the difference in shape of the N_h and N_q axial variations is obvious. N_h, and thus the endwall boundary layer's ability to transfer heat, continues to increase along the entire cord, dropping off at the gauge position which is just downstream of the blade trailing edge (x/C=1.05). From Figure 6-14, the considerable difference between the two non-dimensional values, beginning at approximately 30% x/C and continuing along the length of the cord, is evident and due, in part, to the rotor enthalpy extraction in N_h.

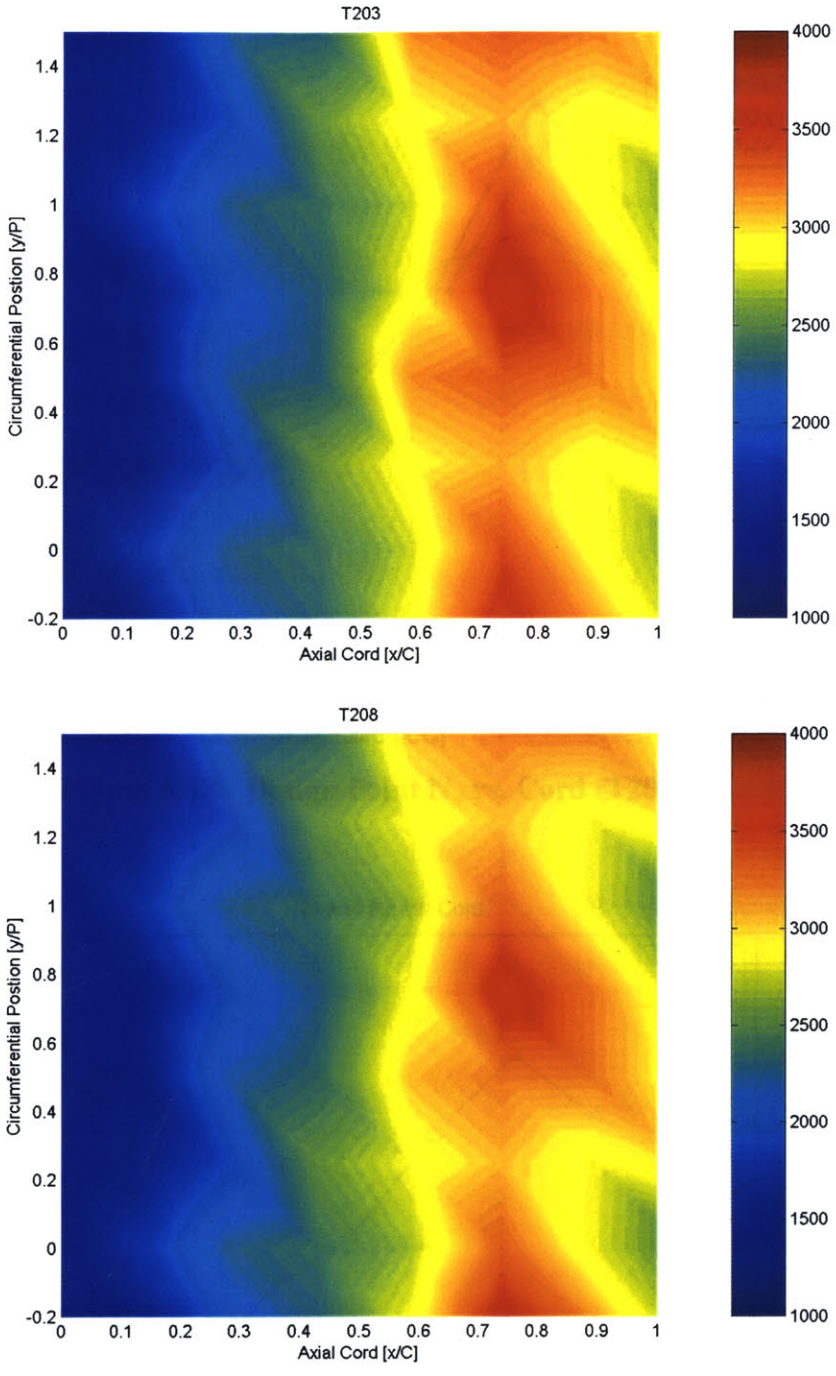

Figure 6-12: N_h, Design Point Tests (T203, T208)

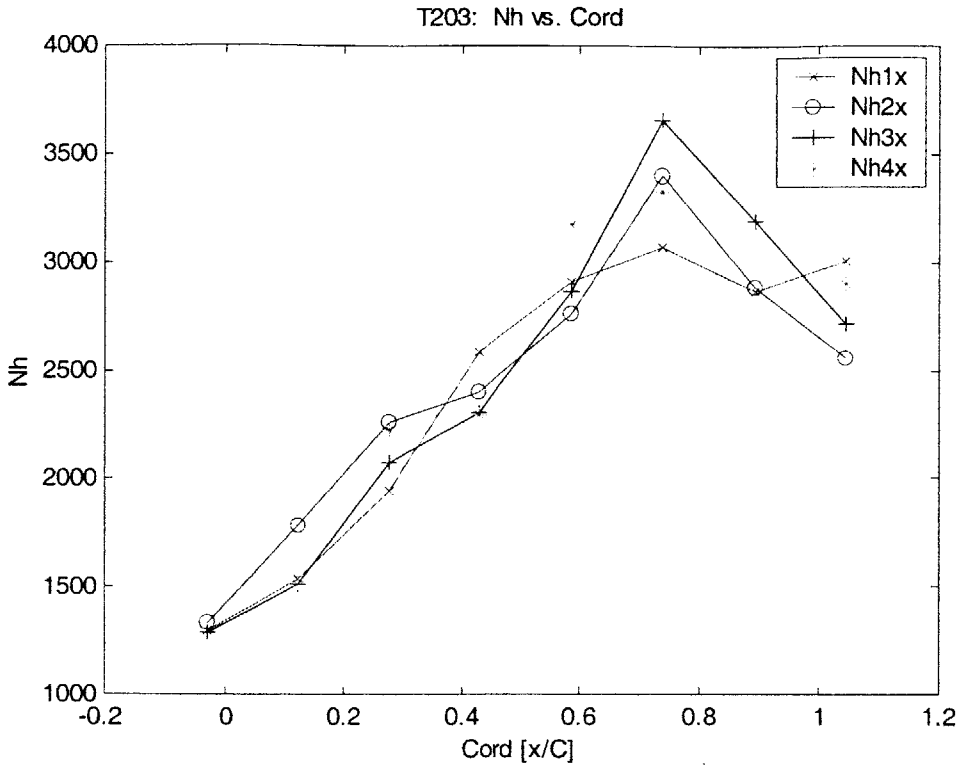

Figure 6-13: Design Point N_h vs. Cord (T203)

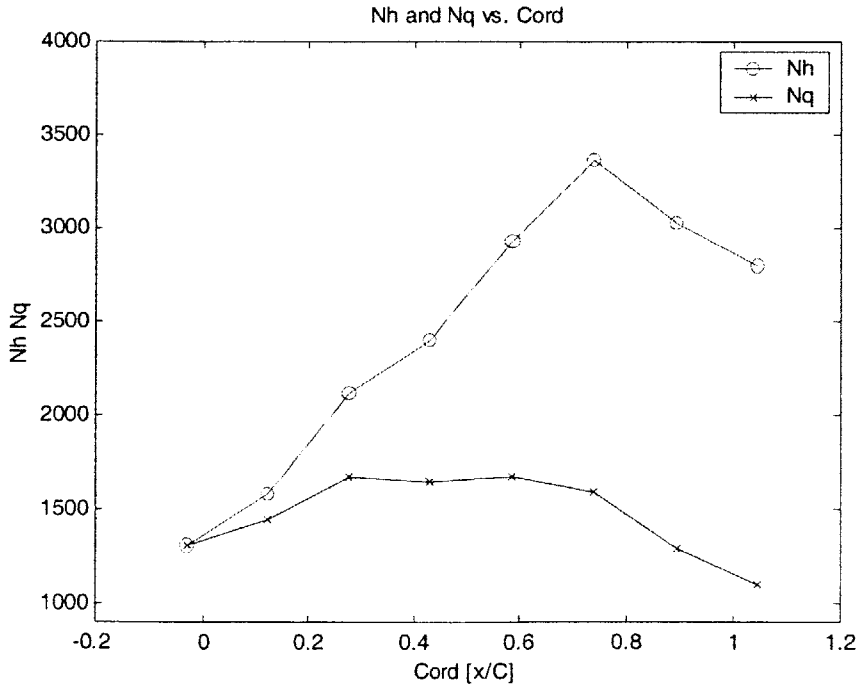

Figure 6-14: N_h and N_q vs. Cord (T203)

6.3.3.1 Pressure Ratio Tests

Heat transfer coefficient data for varying pressure ratio runs is displayed in Figures 6-15 and 6-17.

Of particular interest, the color contour plots for N_h for varying pressure ratio runs reveal the opposite trend as N_q. Whereas time-averaged N_q decreased as pressure ratio increased, N_h increased with higher pressure ratio. The trend in N_h may be due to the difference in the loading distribution along the blade for different stage pressure ratios. Since the higher driving temperature is higher for lower pressure ratio runs, it is possible that this also contributes to the differing behavior of N_q and N_h.

6.3.3.2 Corrected Speed Tests

Film heat transfer coefficient is shown for the different corrected speed runs, illustrated as a color contour in Figure 6-16 and axially in Figure 6-18. Film coefficient showed very similar trends to heat transfer for corrected speed runs. In both cases, the effect of increasing corrected speed was to increase both N_q and N_h. The implications of these observed trends will be discussed later in this chapter

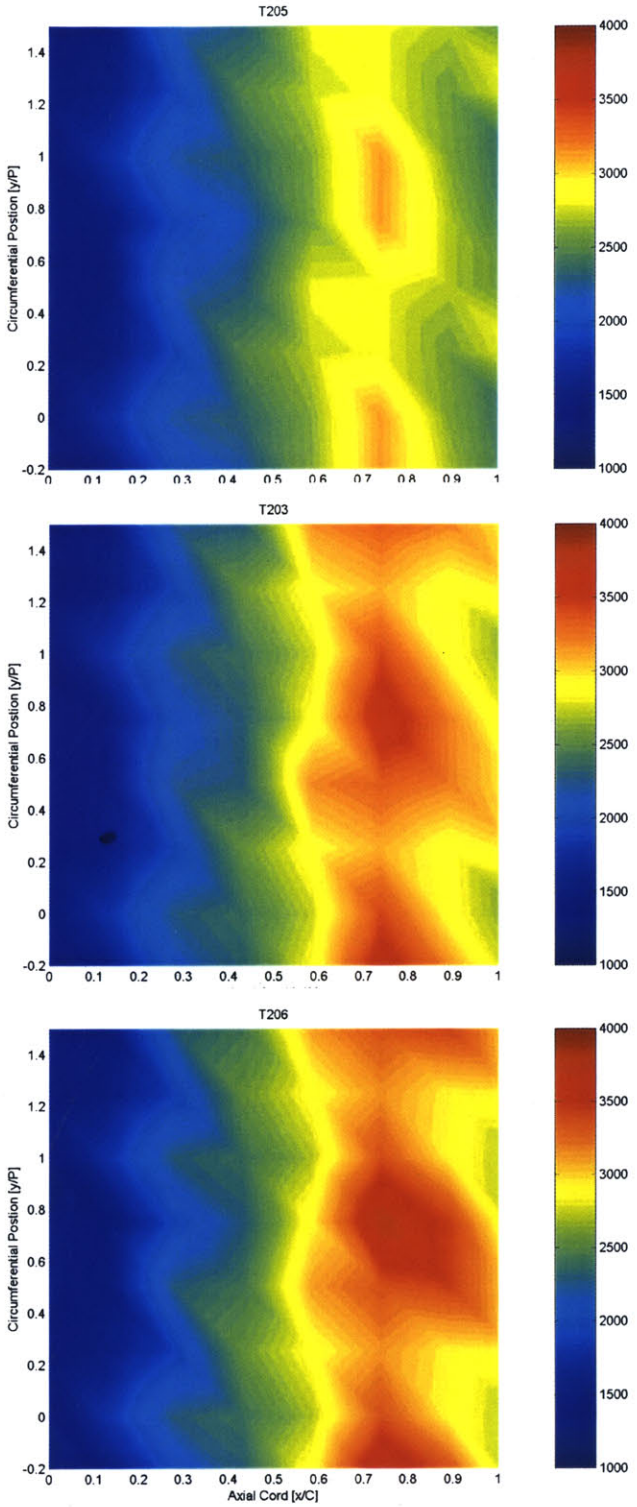

Figure 6-15: N_h for Pressure Ratio Runs (T205, T203, T206)

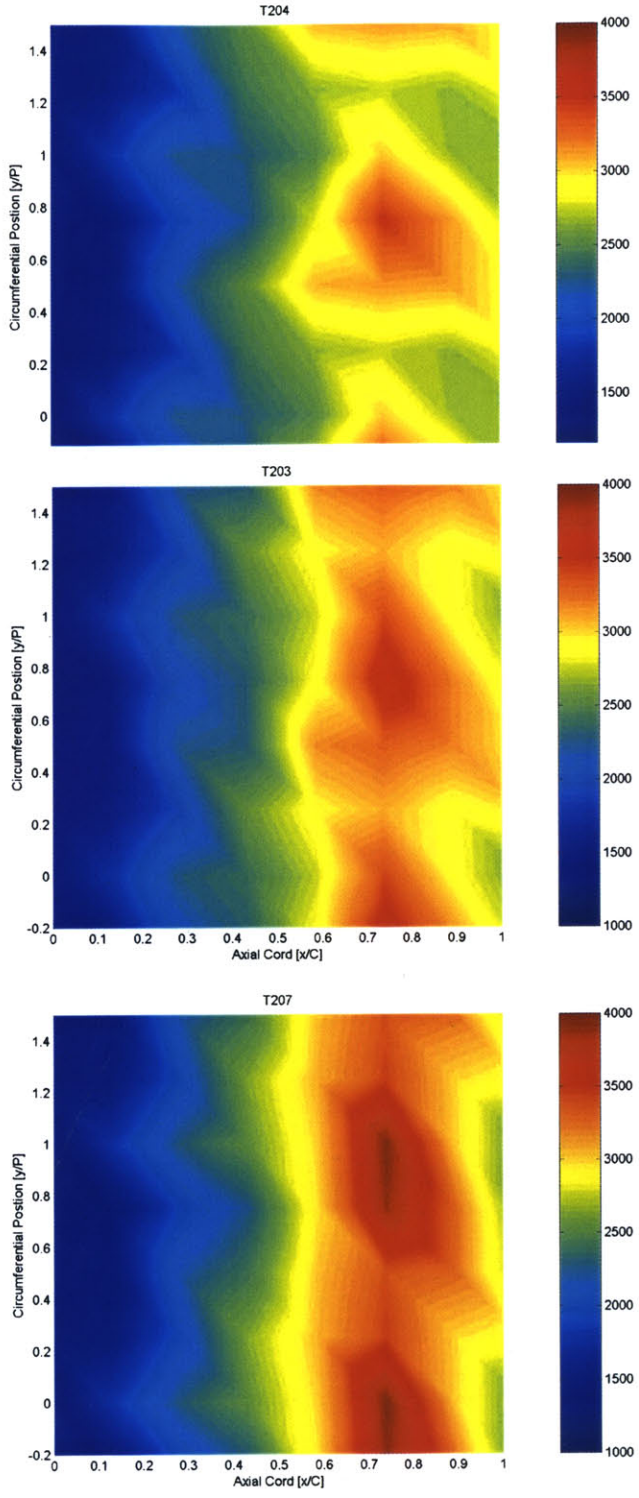

Figure 6-16: N_h for Corrected Speed Runs (T204, T203, T205)

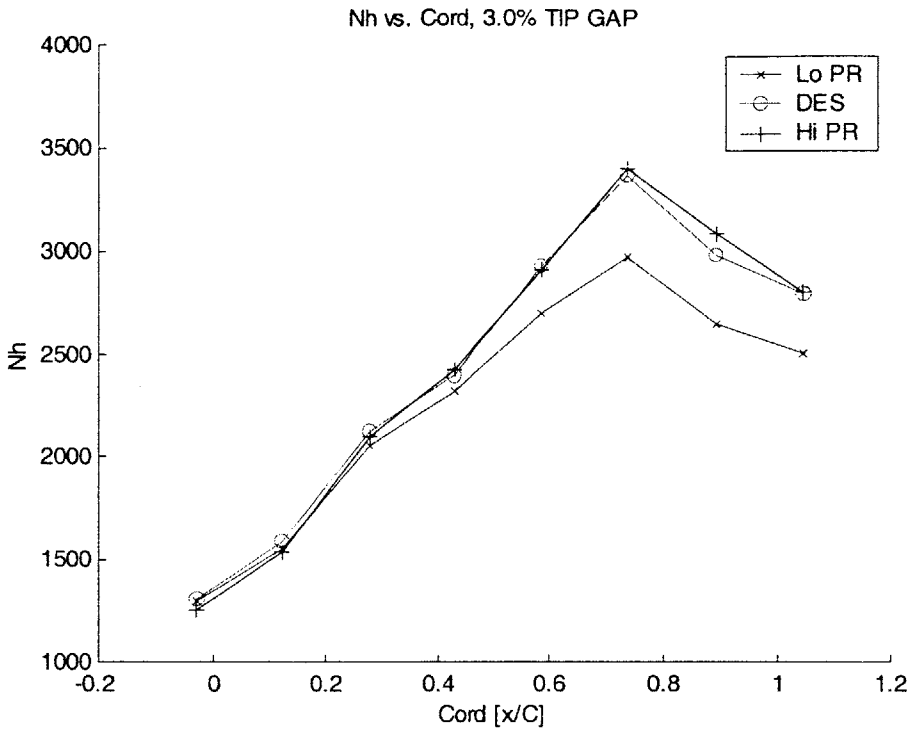

Figure 6-17: Axial Distribution of Nh for Pressure Ratio Tests

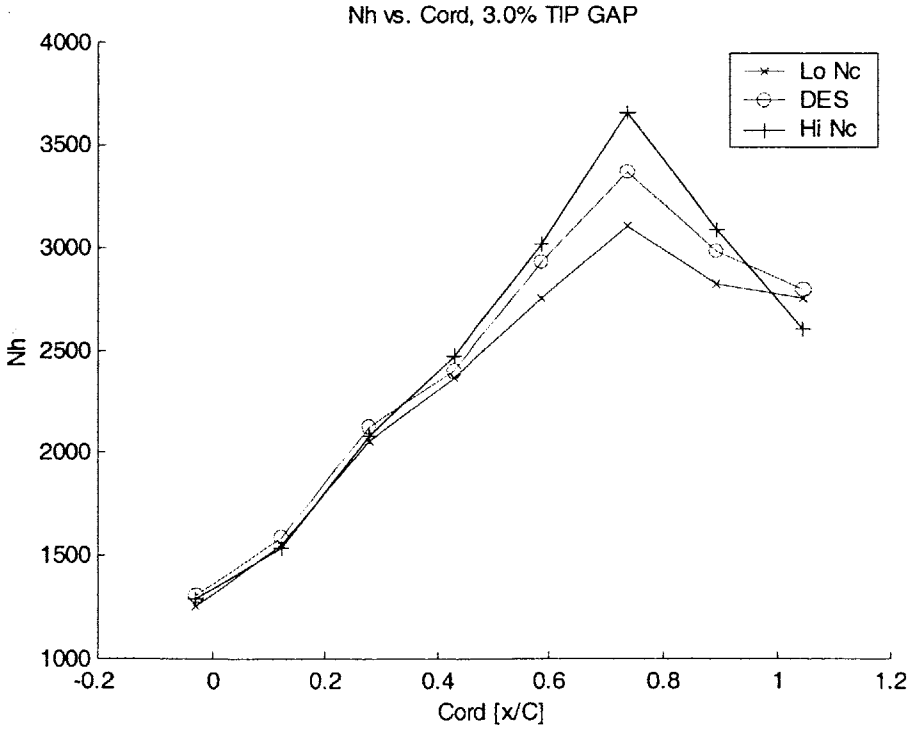

Figure 6-18: Axial Distribution of Nh for Varying Corrected Speed Runs

6.3.4 Discussion

The similarity in the contour maps of the design test runs for N_q suggests strong repeatability of these measurements. The color contour maps of N_q show a steady increase in heat transfer until the 70% cord position, and then a steady decrease through the aft-most gauge. Figure 6-6 clearly illustrates this trend. The axial distribution of N_q with cord is similar to that shown by Guenette [9], although these results show an earlier peak and smaller range of N_q. Since N_q is a direct measure of heat flux to the wall, it can be concluded that this trend is, at least in part, due to rotor enthalpy extraction and the resulting drop in driving temperature.

Along the blade cord, rows of gauges at different circumferential positions show varied trends. Shown in Figure 6-6, the peak values in N_q occur at different locations for each of the gauge rows along the circumference. This trend was observed in all experiments. The circumferential variation implies the possibility of influence by the cooled NGV wakes convecting through the rotor. In many of the contour maps presented, contours appearing as "spurs" of high heat flux are visible from approximately mid-chord to the end of the passage. The direction of these spurs approximates the flow direction as it exits the stator, and therefore may represent further evidence of the influence of nozzle wakes on tip casing heat transfer. Coolant injection at the nozzle trailing edge may affect the distribution of heat flux to the casing. As little full-scale experimentation has been conducted with film-cooled stages, the effects of NGV wakes and coolant injection are unclear. Further experimentation, supported by CFD modeling, will be necessary to confirm any influence.

As pressure ratio was varied for tests, the observable trend in N_q in Figure 6-7 is a dramatic decrease with increasing pressure ratio at 50% axial position and beyond. The difference between the design (T203) and high pressure ratio (T206) tests show a slight decrease in N_q, while the difference between the design and low pressure ratio run (T205) is much more significant. This can be accounted for by the relatively small adjustment of pressure ratio from the design test (approximately 2.1) to the high pressure ratio test (approximately 2.2). Since a higher pressure ratio stage generates more work, the total temperature drop across the stage

($\Delta T_{t_{stage}}$) is also larger for the high pressure ratio run. A resulting decrease in the driving temperature is therefore seen at aft gauge locations. It is postulated that the driving temperature reduction is a significant contributor to the trend of N_q with pressure ratio.

N_q with corrected speed varies only slightly. Although the color contour maps show some variation, the axial plots show very little change in heat flux. In particular, the design test and the high corrected speed tests are nearly identical except for the 25% cord location. The corrected speed for the three test compared was varied from 84% to 94% to 109%. As such, the variation in N_q suggests little dependence of casing heat flux on corrected speed for this class of turbines.

As discussed in section 6.2.3 above, N_h embodies a heat transfer coefficient. When rotor enthalpy extraction is separated out and the effects of the local driving temperature are accounted for, very different trends were observed. In both design point tests, N_h increased steadily through the 75% cord location and then dropped off sharply. Note the similarity of the design point contour maps in Figure 6-12. From Figure 6-14 it can be clearly seen that N_h continues to increase down the cord after the point at which N_q begins to drop off. This trend was observed in every test case. As a heat transfer coefficient, the axial trends of N_h are representative of both the endwall boundary layer and the influence of the tip leakage jet. Previous experimental work has shown that the endwall boundary layer is dominated by the local tip leakage flow [9], with an increasing N_h indicative of a stronger tip leakage flow. The sharp drop at the 75% cord position in Figure 6-14 is similar to that shown previously [9], and is likely the result of decreasing blade thickness near the trailing edge.

One of the most salient trends observed in both N_h and N_q is how each responded to different pressure ratios. As discussed above, N_q decreased steadily at locations aft of mid-cord as test pressure ratio increased. However, the opposite trend is shown in the contour maps of Figure 6-15 for N_h. These results are indicative of a complex endwall flow. Given the higher blade loading that accompanies a higher pressure ratio, it is likely that changes in the tip leakage jet at different pressure ratios contribute to the reversing trends in N_h and N_q. Three-dimensional effects, influenced by coolant and mainstream flow interactions, might be another

contributor. Additional experimental work will be necessary to directly identify any influence of coolant and quantify its effect upon the endwall flow and casing heat load.

Both the color contour maps of Figure 6-16 and the axial plots of Figure 6-18 reveal a region of locally high N_h for corrected speed runs. From Figure 6-18, note that the design and the high corrected speed tests are closely aligned. Given the large increase in corrected speed between the two tests (94% for design; 109% for high corrected speed test), the changes in heat transfer coefficient appear insignificant. For the low corrected speed test, lower values of N_h may be attributable to a low efficiency operating point and reduced loading aft of mid-cord.

6.4 1.5% Tip Gap Results

Heat transfer measurements were made in the MIT BDT with 1.5% tip gap for comparison with 3.0% tip gap data to elucidate any sensitivity to tip gap ratio. The same test matrix as for the 3.0% tests was used for the 1.5% gap tests. Corrected speed and pressure ratio were varied to show any significant departure from trends observed in 3.0% gap tests. A summary of results is provided in Table 6.2.

It must be noted that five of the 32 gauges were inoperative for the 1.5% tip gap tests[2]. The ramification of these gauges was enough to render any color contour plot useless for comparison. Although comparison of different tip gap results was limited, trends of heat transfer phenomenon were both observed and comparable for the 1.5% tip gap tests.

[2] Although two gauges were found to be inoperative for the 3.0% tests, there was very little effect upon the color contour plots displayed in section 6.3.

Table 6.2: Heat Flux Summary for 1.5% Tip Gap Tests

Test	PR	Nc	$\bar{N}_q$	$\bar{N}_h$
T210	2.08	97.3	1469	2038
T211	2.03	86.3	1496	2062
T212	1.86	96.9	1486	1915
T213	2.18	99.0	1396	2075
T214	2.11	114.8	1417	2076
T215	2.09	99.7	1486	2099

6.4.1 Non-dimensionalized Heat Flux

Axial variations for 1.5% gap data are highlighted in Figure 6-19 below, which show time-averaged N_q plotted against normalized axial position for gauge locations at one-quarter normalized pitch. Note the convention of the legend— "Nq1x" –where 1 represents the circumferential locations (row number), while "x" identifies the axial position. The two design point tests are shown to illustrate their agreement.

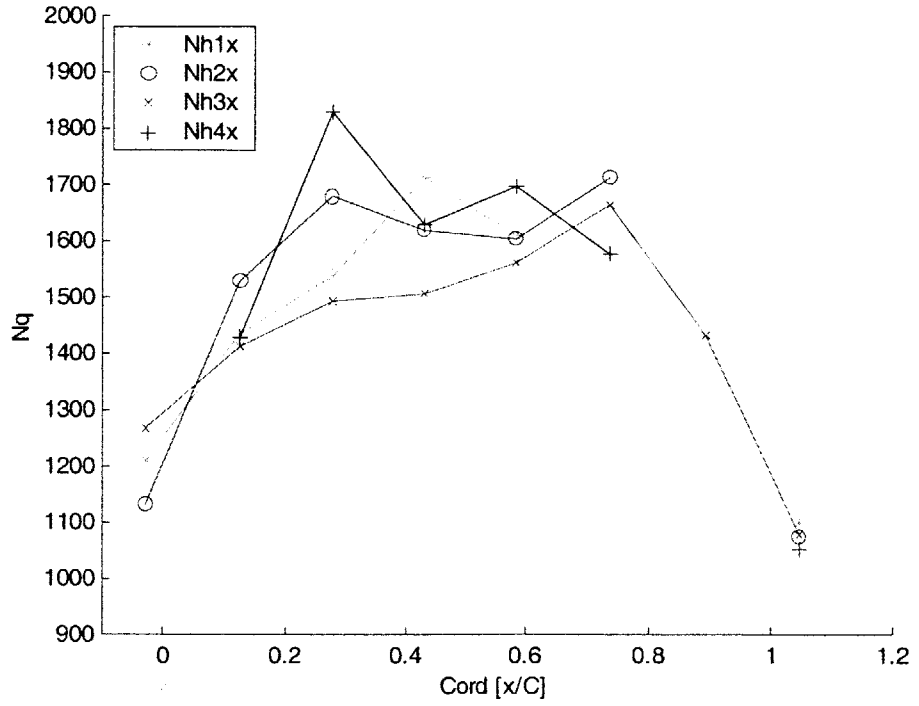

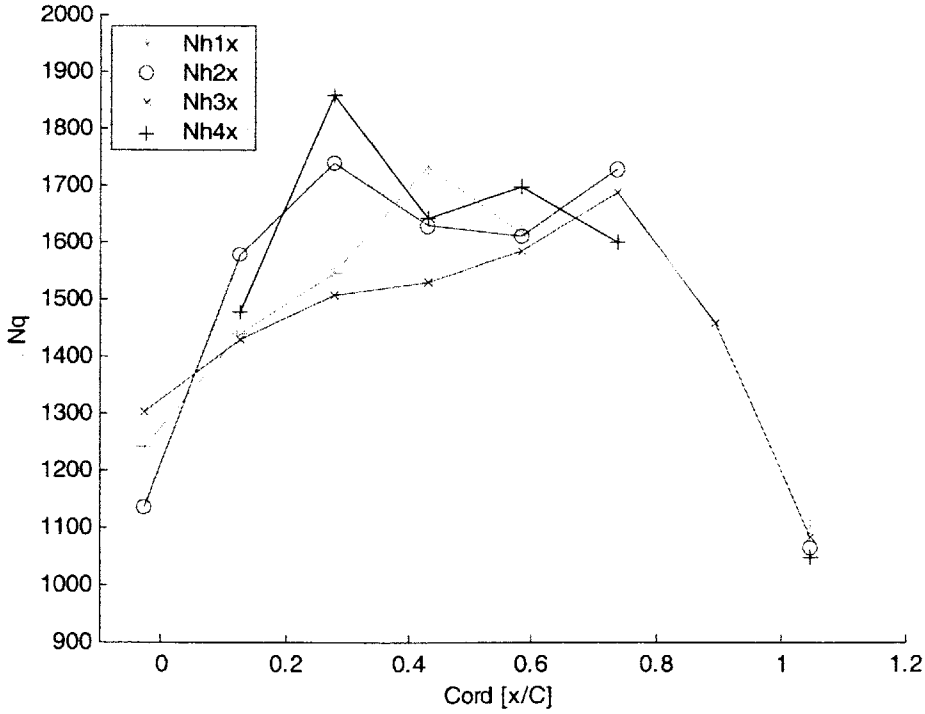

Figure 6-19: Design Point N_q vs. Cord (T210, T215)

For both corrected speed and pressure ratio tests, the endwall averages are shown in Figure 6-20. The variation between tests shows somewhat more variation than was observed for 3.0% data, suggesting the possibility of increased sensitivity of endwall heat load to operating conditions at the smaller tip gap. The extent of the research was unable to confirm this trend, however, and additional research will be required to confirm any change in operating point sensitivity.

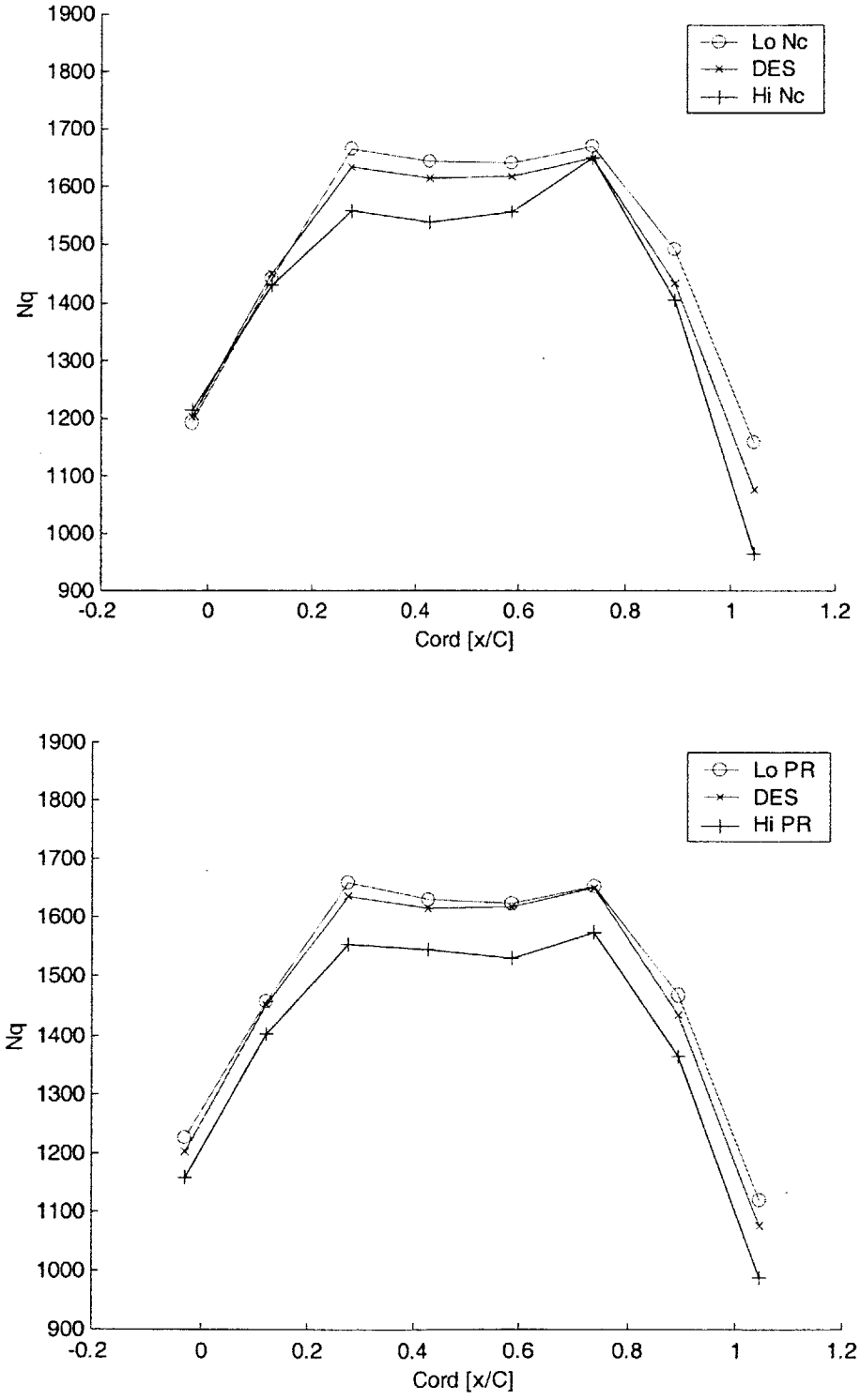

Figure 6-20: Axial Distribution of Nq for Corrected Speed and Pressure Ratio Tests

6.4.2 Non-Dimensionalized Heat Transfer Coefficient

The non-dimensionalized heat transfer coefficient based upon local total temperature, N_h, is presented here for all experimental tests at 1.5% gap. Figure 6-21 shows the relative magnitudes of N_h and N_q. The axial distribution of all gauges is shown in Figure 6-22 for both design point tests to highlight the agreement between runs. Figure 6-23 shows N_h for PR and Nc tests.

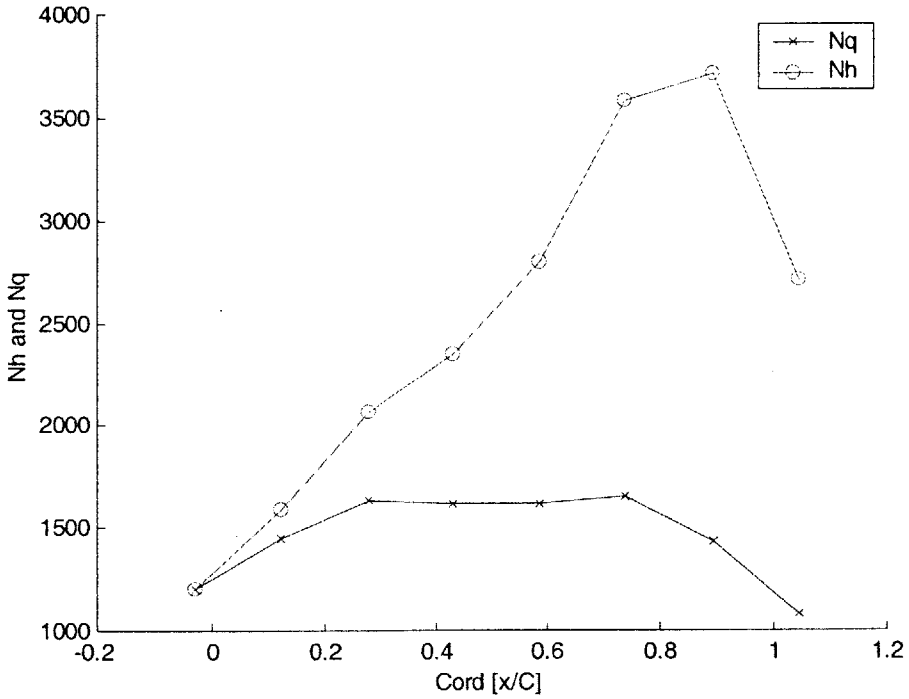

Figure 6-21: N_h and N_q vs. Cord (T210)

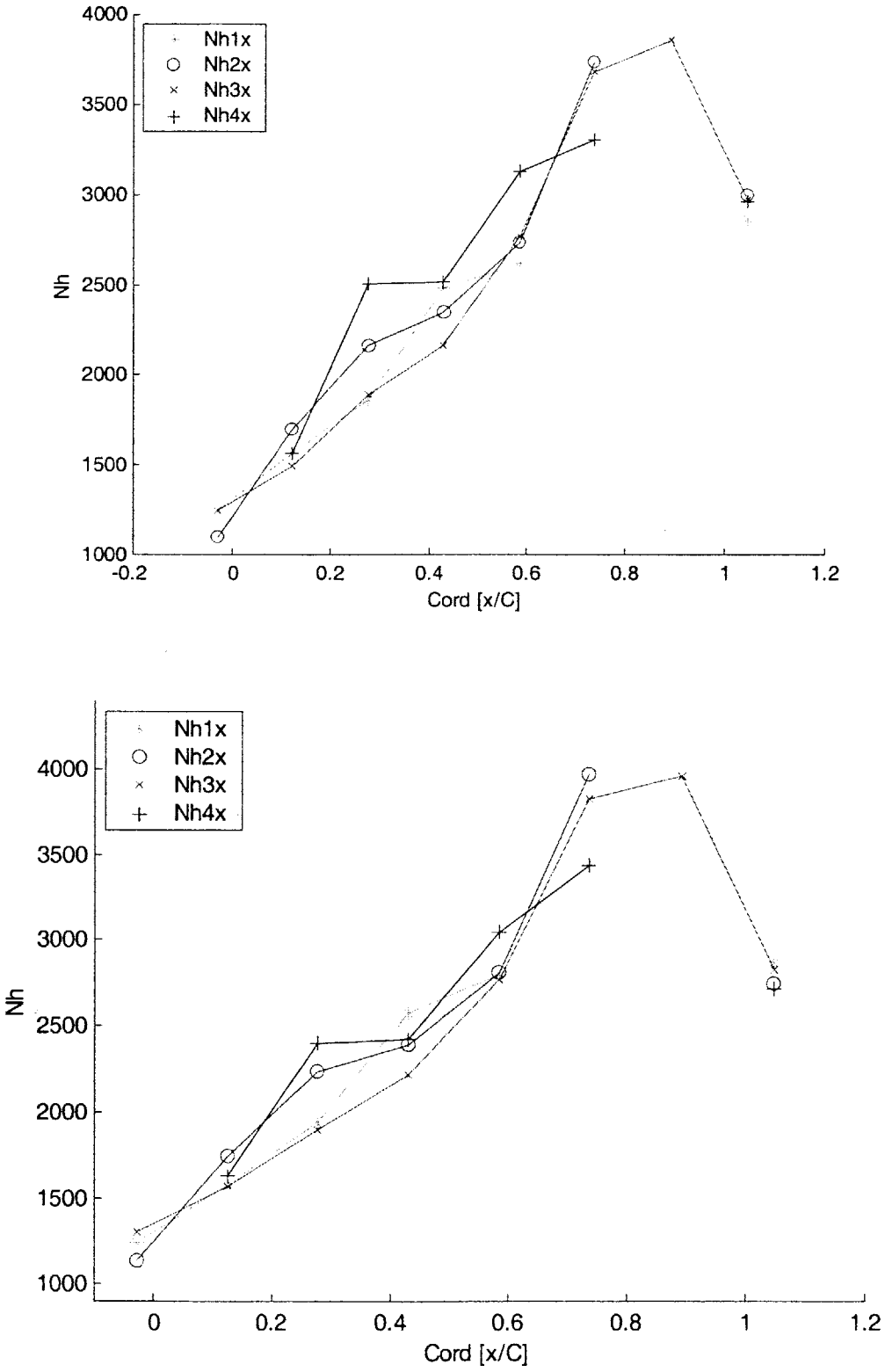

Figure 6-22: Design Point N_q vs. Cord (T210, T215)

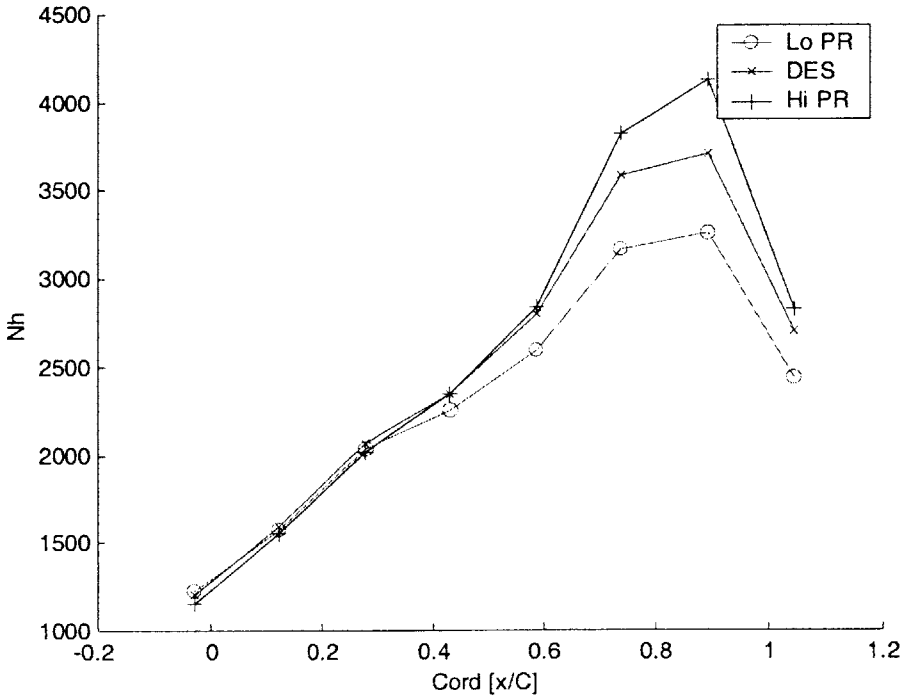

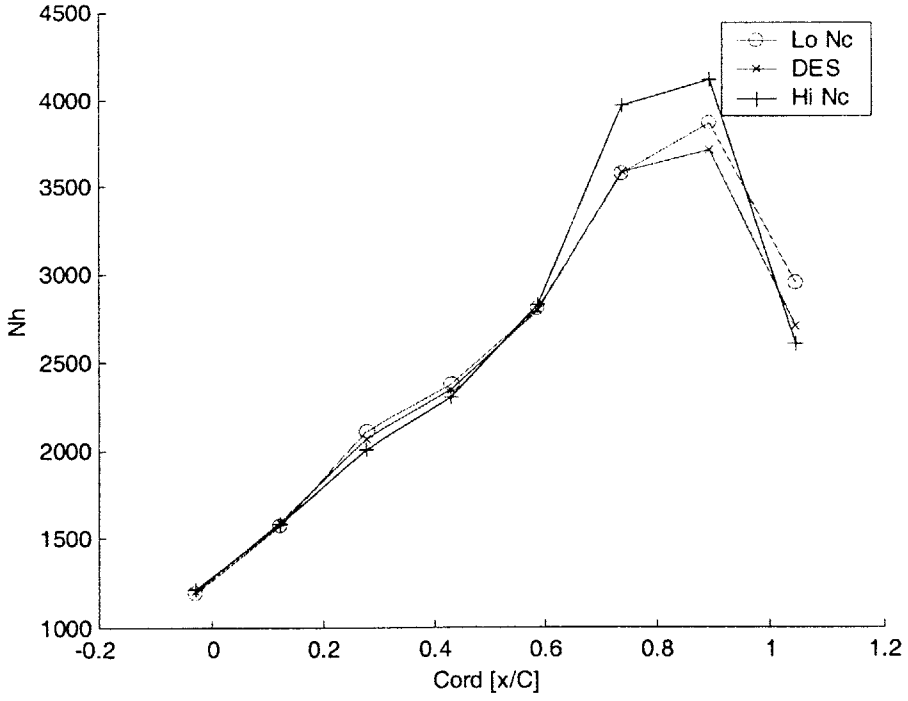

Figure 6-23 Axial Distribution of Nh for Pressure Ratio and Corrected Speed Runs

6.5 Comparison of Tip Gap Results

In order to compare heat transfer results between tip gaps, it was necessary to adjust the results to one common operating point. An inspection of Figure 6-24 reveals that the operating points for the design point tests align closely with respect to pressure ratio.

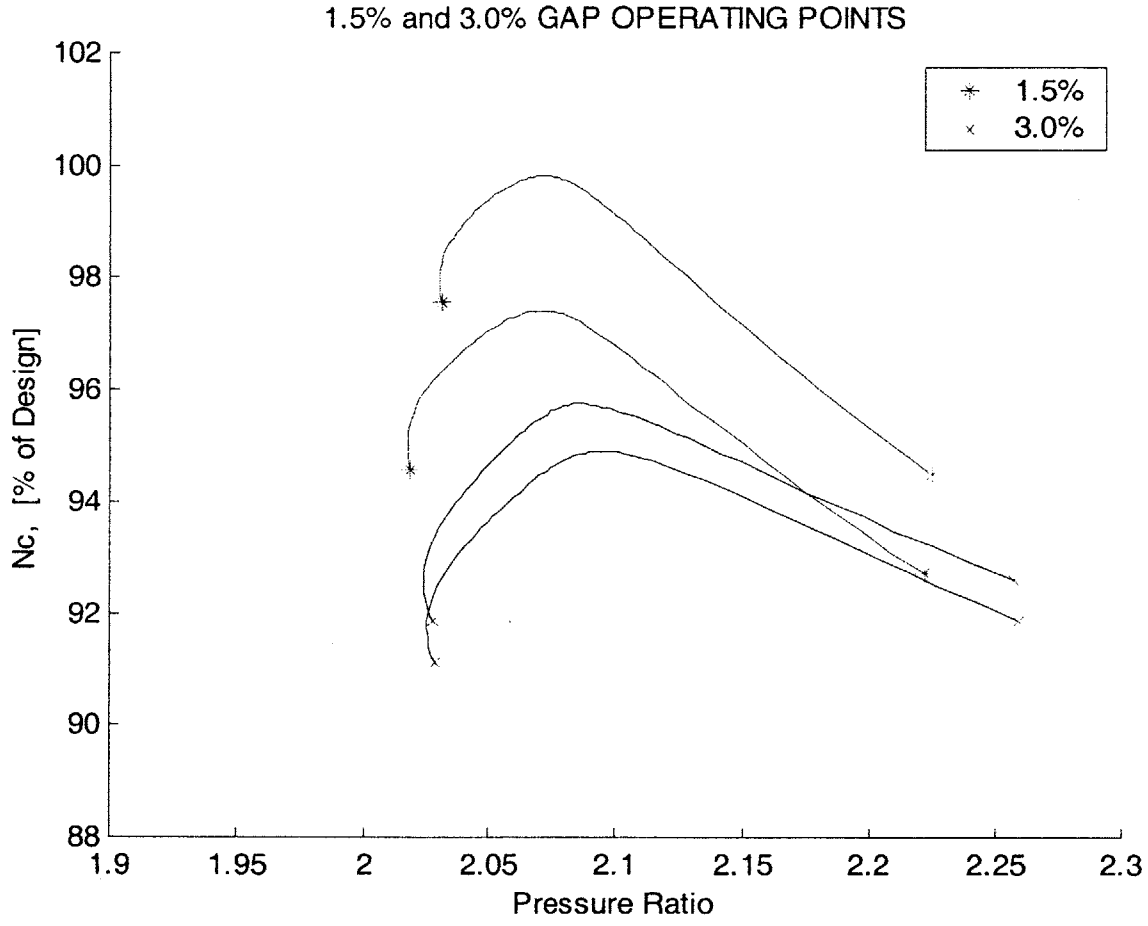

Figure 6-24 Design Test Operating Maps

Thus, the simplest approach was determined to be an adjustment for corrected speed for operating points at the same pressure ratio—in other words, estimating the partial derivative of heat flux with respect to corrected speed and then adjusting heat flux for the difference in corrected speed.

Rotor revolution averaged heat flux for both design point 3.0% gap and both 1.5% gap runs were averaged over the endwall for one representative pressure ratio. The partial derivative with respect to corrected speed, $\frac{\partial N_q}{\partial N_c}$, was approximated for both the 3.0% gap design point runs by $\left.\frac{\Delta N_q}{\Delta N_c}\right|_{3.0\%}$. The 1.5% and 3.0% data were then adjusted to a common operating point corrected speed. This technique is summarized as:

$$N_q\big|_{3.0\%\,adj} = N_q\big|_{3.0\%} + \left(\left.\frac{\Delta N_q}{\Delta N_c}\right|_{3.0\%}\right)\Delta N_c\big|_{1.5\%-3.0\%} \tag{6.5}$$

This procedure was repeated for many pressure ratios within the useful test window. Results are displayed below in Table 6.3 for a pressure ratio of 2.1.

Table 6.3: Tip Gap Heat Transfer Comparison

Test	PR	Nc	Nq	Nc_adj	Nq_adj
T203	2.1	94.9	1731.5	96.0	1694.6
T208	2.1	95.6	1708.0	96.0	1694.6
T210	2.1	96.8	1759.4	96.0	1765.5
T215	2.1	99.2	1741.0	96.0	1765.5

The adjustment for operating point revealed a 4% greater N_q at the 1.5% tip gap. Additional testing at more closely matched operating points, as well as CFD simulations, may be necessary to confirm this observation.

6.6 Summary

The results of an experimental investigation of time-averaged tip casing heat transfer have been presented for two different tip gaps. The test reproduced all of the full scale, non-dimensional turbine flow parameters. Measurements were taken as a function of operating point—pressure ratio and corrected speed. Two non-dimensional parameters were defined to compare both heat flux and the heat transfer coefficient of the endwall boundary layer. Heat transfer data was compared within each test, for different operating conditions at the same tip

gap, and for different tip gap tests. The data shows some circumferential variation in heat flux at the same axial position. Heat flux axial distribution reflects the influence of rotor enthalpy extraction down the cord. Distinct trends in heat flux and heat transfer coefficient were observed for both tip gaps; average levels of endwall heat load increased by approximately 4% when the tip gap was decreased from 3.0% to 1.5%.

Chapter 7

Closure

7.1 Review of Objectives

As described in Chapter 1, the primary objective of this research was to experimentally measure the tip casing heat transfer of a scaled film-cooled turbine stage. The project posed many engineering challenges to that end. In all, the principal objectives for this project included:

1. The construction and validation of surface temperature thermometers with sufficient frequency response, sensitivity, and stability to adequately measure tip casing heat transfer

2. The design and fabrication of an instrumented device to hold surface temperature and pressure instruments on the rotor tip casing to resolve spatial and temporal trends in heat transfer and wall static pressure. This includes the necessary facility modifications to adequately house and support the device.

3. The measurement of heat flux on the tip casing of a film-cooled turbine stage

4. The preliminary investigation of measured tip casing heat transfer to identify trends in time-averaged data and compare results for different operating point and tip gaps

5. The creation of a detailed data set for use in physics-based modeling, CFD code validation, and eventually for improved design of film-cooled turbine stages of this class.

7.2 Summary of Work

An experimental study of the heat transfer to the tip casing of a fully scaled turbine stage was conducted. Pressure and surface temperature measurements were taken on the tip casing. Time-averaged heat flux data were computed and used to assess the influence of stage total pressure ratio, corrected speed and tip gap on casing heat flux.

The experimental work was conducted in the MIT Blowdown Turbine Facility using a film-cooled turbine stage. The facility is a short duration experimental structure capable of testing turbine stages under fully scaled conditions to produce useful test durations of 0.5 seconds. The turbine stage tested consisted of film-cooled turbine blades and nozzle guide vanes. During the course of this research, high frequency response heat flux gauges were designed and fabricated by painting and baking thin platinum films onto machineable ceramic substrates. These gauges were used to experimentally measure surface temperatures on the tip casing with an estimated frequency response of 60 kilohertz. A tip casing insert was designed as an instrument holder to orient the heat flux gauges and highly sensitive pressure transducers on the tip casing surface to spatially resolve heat flux and static pressure.

A matrix of test conditions was devised to investigate the effects of various run conditions and tip gap ratios on tip casing flow. Both a 3.0% and 1.5% tip-gap-to-span ratios were tested. Run conditions were established by varying the stage pressure ratio and the corrected speed. Results were compared within each test, between tests at the same tip gap, and between tests at different tip gaps. Non-dimensionalized heat flux was used to reveal the influence of rotor enthalpy extraction and operating point on casing heat flux. A non-dimensionalized heat transfer coefficient was used to gain insight into the character of the endwall boundary layer along the blade cord. Time averaged data revealed similar trends for similar test conditions at both tip gaps. At design conditions, average endwall heat transfer was approximately 4% greater for the 1.5% tip gap.

7.3 Recommendation for future work

There are several near-term recommendations that can be made to improve upon the results reported herein. Additional experimental testing with various rates of coolant can be conducted to elucidate the influence of film cooling on the endwall heat transfer. In particular,

the coolant to the NGVs should be varied, as the effects of the interaction of the trailing edge and surface NGV coolant with the mainstream flow upon the casing flow are unclear.

Additional testing at more closely matched operating points, with very distinct changes in pressure ratio and corrected speed, may be useful in supporting the conclusions of this work. Experimental measurements of blade tip heat transfer may also provide further insight into the complex flow field on the casing surface.

Further numerical analysis of the data for both tip gaps is warranted. Efforts should be made to analyze the time resolved heat flux to determine the variation of peak heat loads with tip gap and operating point. An analysis of both time average and time resolved casing pressure measured during this experiment is also necessary. From a design perspective, the time-resolved pressure measurements may prove valuable in reducing required coolant plenum pressure and coolant mass flow for this class of turbines.

Long term recommendations include physics-based modeling of the endwall flow. In conjunction with the data set provided, CFD simulations should model the NGV wake and coolant-to-mainstream interactions in the endwall boundary layer to characterize the casing surface flow and identify the effect on heat transfer. With simulated results for both 1.5% and 3.0% tip gaps, comparisons between CFD and experimental results can be made.

BIBLIOGRAPHY

1. A.A. Ameri, E. Steinthorssen, D.L. Rigby. "Effects of Tip Clearance and Casing Recess on Heat Transfer and Stage Efficiency in Axial Turbines." NASA/CR. 1998.

2. A.A. Ameri and R.S. Bunker. "Heat Transfer and Flow on the First Stage Blade Tip of a Power Generation Gas Turbine, Part 2: Simulation Results." *J. or Turbomachinery,* 99-GT-283.

3. ASME/ANSI MFC-7M-1987, "Measurement of Gas Flow by Means of Critical Flow Venturi Nozzles," *An American National Standard,* The American Society of Mechanical Engineers, 1987.

4. R.S. Bunk, J.C. Bailey, and A.A. Ameri. "Heat Transfer and Flow on the First Stage Blade Tip of a Power Generation Gas Turbine, Part 1: Experimental Results." *J. or Turbomachinery,* 99-GT-169.

5. Y Cai., "Aerodynamic Performance Measurements in a Fully Scaled Turbine," Masters Thesis, Massachusetts Institute of Technology, February, 1998.

6. H.W. Coleman and W.G. Steele. *Experimentation and Uncertainty Analysis for Engineers.* John Wiley and Sons, second edition, 1999.

7. J.D. Denton. "Loss Mechanisms in Turbomachines." *J. of Turbomachinery,* 115:621-656, January 1993.

8. A.H. Epstein, G.R. Guenette, and F.J.G. Norton, "The MIT Blowdown Turbine Facility," ASME Paper 84-GT-116, 1984.

9. G.R. Guenette. "A Fully Scaled Short Duration Turbine Experiment." Sc.D thesis, Massachusetts Institute of Technology, 1985.

10. G.R. Guenette. "The Measurement of Cooled Turbine Performance." Final Technical Report. Prepared for ABB ALSTOM Power, Inc, March 2000.

11. C.W. Haldrman. "An Experimental Study of Radial Temperature Profile Effects on Turbine Tip Shroud Heat Transfer." Master's Thesis, Department of Aeronautics and Astronautics, MIT, 1989.

12. M.A. Hilditch and R.W. Ainsworth. "Unsteady Heat Transfer Measurements on a Rotating Gas Bas Turbine Blade." *J. of Turbomachinery,* 1990. 90-GT-175.

13. F.P. Incropera and D.P. DeWitt. *Introduction to Heat Transfer.* John Wiley and Sons, second edition, 1990.

14. R.C. Keogh. "Aerodynamic Performance Measurements of a Film-Cooled Turbine Stage." PhD thesis, Department of Aeronautics and Astronautics, MIT, 2001.

15. R.C. Keogh. "Shaft Efficiency Measurements of a Fully Scaled Turbine in a Short Duration Facility. Master's Thesis, Department of Aeronautics and Astronautics, MIT, 1998.

16. J.L. Kerrebrock. *Aircraft Engines and Gas Turbines.* The MIT Press, second edition, 1992.

17. D.R. Kirk, G.R. Guenette, S.P. Lukachko, and I.A. Waitz. "Near Wall Reaction Effects on Film-Cooled Flat Plate Heat Transfer."

18. D.E. Metzger and K. Rued. "The Influence of Turbine Clearance Gap Leakage on Passage Velocity and Heat Transfer near Blade Tips: Part I—Sink Flow Effects on Blade Pressure Surface Side." *J. of Turbomachinery*, Volume 111, pages 284-292.

19. A.F. Mills. *Heat and Mass Transfer.* Irwin, 1995.

20. K. Rued and D.E. Metzger. "The Influence of Turbine Clearance Gap Leakage on Passage Velocity and Heat Transfer near Blade Tips: Part II—Source Flow Effects on Blade Suction Sides." *J. of Turbomachinery*, Volume 111, pages 293-300

21. O.P. Sharma and T.L. Butler. "Predictions of Endwall Losses and Secondary Flow in Axial Flow Turbine Cascades." *ASME J. or Turbomachinery*, 1987. 86-GT-228.

22. C.M. Spadaccini. "Aerodynamic Performance Measurements of a Fully Scaled, Film-Cooled, Turbine Stage." Master's thesis, Department of Aeronautics and Astronautics, MIT, 1999.

23. R.J. Vidal. "Model Instrumentation Techniques for Heat Transfer and Force Measurement in Hypersonic Shock Tunnel." Report Number AD-917-A-1. Cornell Aeronautical Laboratory, 1956.

24. Shang, T. "Influence of Inlet Temperature Distortion on Turbine Heat Transfer." Ph.D. Thesis, Massachusetts Institute of Technology, February 1995.

2766 - 34